

INAUGURAL - DISSERTATION

zur

Erlangung der Doktorwürde

der

Naturwissenschaftlichen - Mathematischen

Gesamtfakultät

der Ruprecht-Karls-Universität

Heidelberg

vorgelegt von

Dipl.-Phys. Sabrina Roßberger

aus Wiesbaden

Tag der mündlichen Prüfung: 18.06.2014

**Kombination von Strukturierter Beleuchtung und
Lokalisationsmikroskopie in einem neuen Setup mit Anwendungen an
retinale Strukturen**

Gutachter:

Prof. Dr. Dr. Christoph Cremer

Prof. Dr. Sabine Heiland

Dissertation
submitted to the
Combined Faculties for the Natural Sciences and for Mathematics
of the Ruperto-Carola University of Heidelberg, Germany
for the degree of
Doctor of Natural Sciences

Put forward by
Diplom-Physicist: Sabrina Roßberger
born in: Wiesbaden

Oral Examination: 18.06.2014

**A novel combined Structured Illumination and Single Molecule
Localization Microscope and its application to Retinal Structures**

Referees:

Prof. Dr. Dr. Christoph Cremer

Prof. Dr. Sabine Heiland

...dedicated to my family and friends...

Nothing is impossible! (All Blacks)

Disclosure

Main parts of this work have been published in Rossberger *et al.*¹ '*Combination of structured illumination and single molecule localization microscopy in one setup*', *Journal of Optics, Special Issue on High-Resolution Optical Imaging* (2013) and in Rossberger *et al.*² '*High-resolution imaging of autofluorescent particles within drusen using structured illumination microscopy*', *British Journal of Ophthalmology*, Vol. 97 (2013).

Zusammenfassung

Fluoreszenzmikroskopische Methoden sind eine der wichtigsten Bildgebungsverfahren in Life-Science. Jede dieser Methoden ist jedoch auf ein bestimmtes Anwendungsgebiet limitiert. Es wurde ein neues vollautomatisiertes und benutzerfreundliches 'Combo'-Mikroskop entwickelt, welches die zwei hochauflösenden Mikroskopiemethoden 'Strukturierte Beleuchtung' und Lokalisationsmikroskopie in einem Setup vereint. Beide Methoden sind zueinander komplementär, so dass das 'Combo'-Mikroskop das Spektrum an Anwendungsgebieten in der biomedizinischen Forschung erweitert. Außerdem, können durch die Bildgebung und -verarbeitung auftretende Artefakte kenntlich gemacht werden. Eine mögliche Missinterpretation von supraauflösender Daten wird dadurch reduziert.

Motiviert wurde diese Arbeit durch die altersbedingte Makuladegeneration (AMD). Diese Krankheit ist die häufigste Erblindungsursache in der westlichen Welt. Untersucht werden autofluoreszente Partikel in altersbedingten Ablagerungen (Drusen) unterhalb des retinalen Pigmentepithels. Desweiteren wird das neu entwickelte 'Combo'-Mikroskop im dualen Modus genutzt um das Axon Initial Segment in retinalen Ganglien Zellen in 3D zu visualisieren. Dieses stellt eine essentielle Schaltstelle in der visuellen Signaltransduktion darstellt. Zuletzt wird eine *in vitro* Studie, welche die unterschiedliche Effektivität von Medikamenten zur AMD Behandlung vergleicht, skizziert.

Abstract

Fluorescence microscopy methods have become an major imaging tool in biomedical life-science. However, each method only addresses specific questions due to intrinsic limitations. A new, fully automated and user-friendly 'Combo'-microscope setup has been developed, which combines the two advanced high-resolution methods Structured Illumination and Localization Microscopy into one imaging system. As both methods complement one another, the 'Combo'-microscope will greatly extend the range of application in biomedical research. Moreover, artifacts, introduced in the course of the imaging and/or reconstruction processes, can be revealed and potential mis-interpretation of super-resolution data is limited.

This work was motivated by the age-related macular degeneration (AMD), a disease, which is the leading cause of blindness in the Western world. Autofluorescent particles within age-related deposits (drusen) beneath the retinal pigment epithelium are studied on advanced resolution level. Furthermore, the newly built microscope is used for a dual-mode dual-color three-dimensional visualization of the axon initial segment, a crucial region for signal transduction in vision, of retinal ganglion cells. Finally, an *in vitro* study comparing the pharmaceuticals currently used for AMD-treatment is outlined.

1	Introduction	1
2	Background	7
2.1	Optical Imaging	7
2.1.1	Point Spread Function (PSF)	8
2.1.2	Optical Transfer Function (OTF)	8
2.1.3	Fluorescence Microscopy	9
2.1.4	Structured Illumination Microscopy (SIM)	12
2.1.5	Single Molecule Localization Microscopy (SMLM)	15
2.1.6	SMLM vs. SIM	19
2.2	Biological Models	22
2.2.1	Anatomical Structure of the Human Eye	22
2.2.2	Retina and the retinal pigment epithelium (RPE)	23
2.2.3	Visual cycle	24
2.2.4	Lipofuscin (LF), melanolipofuscin (MLF) and A2E	26
2.2.5	Drusen and age-related macular degeneration (AMD)	27
3	Methods	33
3.1	SIM - Microscope Setup	33
3.1.1	Hardware	33
3.1.2	Software	35
3.2	Development of the 'Combo' - Microscope Setup	36
3.2.1	Hardware	36
3.2.2	Electronics	42
3.2.3	Software	45

3.3	Sample Preparation	49
3.3.1	Section preparation retina	49
3.3.2	Tissue preparation retina	49
3.3.3	RPE-cell culture	50
3.4	Imaging and Analysis	52
3.4.1	Retinal histological sections	52
3.4.2	Retinal tissue	53
3.4.3	RPE-cell culture	54
3.5	Simulation of Artifacts	58
4	Results	59
4.1	Analysis of Autofluorescent Particles within Drusen using SIM	59
4.2	Resolution and Artifacts in SMLM & SIM Imaging	69
4.3	Co-localization Analyses with the 'Combo'-Setup	74
4.4	Live-cell experiments with the 'Combo'-Setup	83
5	Discussion	87
5.1	Autofluorescence Study of Drusen using SIM	87
5.1.1	Autofluorescent Particles within Drusen	87
5.1.2	Autofluorescent 'ring-like' Structures within Drusen	89
5.2	The developed 'Combo' - Microscope	90
5.2.1	Application and Benefits	90
5.2.2	Revealing Artifacts in SIM- and SMLM-Imaging	92
5.3	Application of the 'Combo'-microscope	94
5.3.1	Dual-mode dual-color three-dimensional visualization of AIS in retinal ganglion cells	94
5.3.2	<i>In vitro</i> Experiments: VEGF Inhibitors in AMD-Treatment	95
6	Conclusion and Outlook	97

CHAPTER 1

INTRODUCTION

The ability to visualize biological structures and processes on the nanometer scale is instrumental to understanding of functionality in health as well as during dysfunction and structural abnormalities in disease. A universal imaging method that is able to address all biological, physiological or medical questions is currently not available, because each method is subject to its own specific set of limitations and is therefore only able to cover specific applications. Consequently, a big challenge is finding a suitable imaging method, which will allow structures in biological samples to be spatially localized and correlated on the molecular level. These high-resolution insights may then provide a basis for further evaluating functionality as well as interaction at the cellular and molecular level. Thus, the development and refinement of new imaging methods to extend the range of possible applications will be important in promoting the progress of research in life science.

When fluorescence microscopy was first used as a new imaging tool in biomedical research, it provided a unique, high contrast mechanism based on specific labeling of target structures. Though it was rapidly adopted and established as a high quality approach to visualize cellular structure and function, fundamental resolution restrictions limit the spatial resolution of widefield fluorescence microscopy to ~ 200 nm.^{3,4} Over the past decade various fluorescence microscopy methods have been developed in order to circumvent this limitation, but each method is again restricted to certain applications.⁵ Moreover, most of these so called super-resolution microscopy images suffer from artifacts introduced either during the imaging process or by various different image reconstruction algorithms.^{1,6-8} The interpretation of super-resolution images has therefore been a challenging endeavor.

The aim of this thesis was the development of a high-resolution fluorescence imaging system, which exhibit enhanced contrast and resolution properties a single fluorescence

microscopy method cannot provide. To achieve this, two complementary advanced high-resolution fluorescence microscopy methods were combined in a novel super-resolution microscope setup.

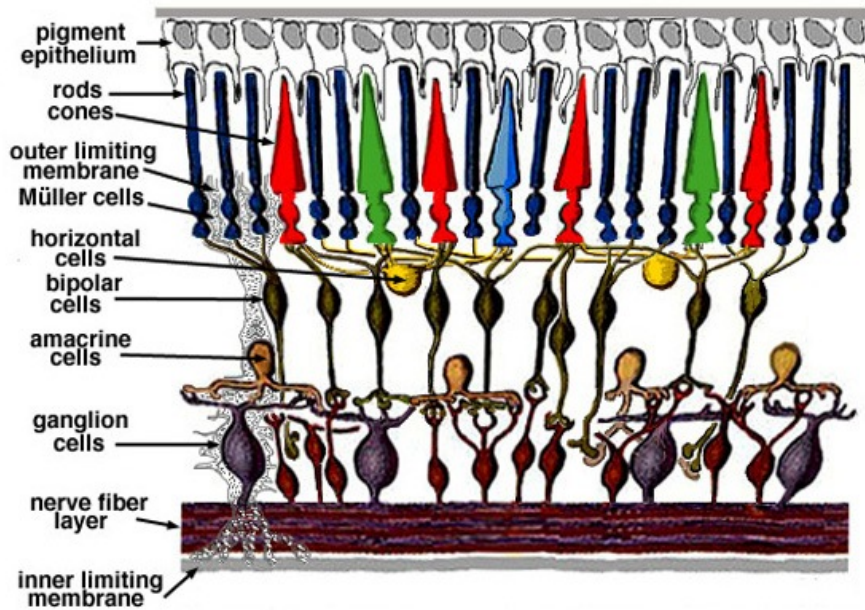


Figure 1.1: Schematic of the retina: Ten layers contributing to the anatomical structure of the retina. Details can be found in section 2.2.2. From Kolb *et al.*⁹

The development of such an imaging method was motivated by its potential to fill a gap in biomedical research. An example for such a gap exists in retina research. Age-related macular degeneration (AMD) is a devastating retinal neurodegenerative disease that is one of the main causes for blindness in the Western world.¹¹ During the course of this disease, the area of highest acuity in the eye, the central retinal field (macula) degenerates, which results in substantial cell loss and consequently, blindness. Since it is the central visual field that is first affected, patients suffer from a rapid loss of abilities to read or recognize faces although some daily activities remain possible during disease progression.

On the cellular level AMD is caused by dystrophy of a specific retinal cell type, the retinal pigment epithelium (RPE, fig. 1.1). Metabolically, RPE cells coordinate an essential part of the visual cycle.^{12,13} When they degenerate, vision is no longer possible. Downstream, the loss of RPE cells then leads to further retinal degeneration within the neuronal population of retinal cells (ganglion cells, fig. 1.1).

'Drusen', focal deposits between the choroid and RPE, are among the first symptoms used in the clinical setting to diagnose AMD. Drusen are followed by atrophy of the RPE and

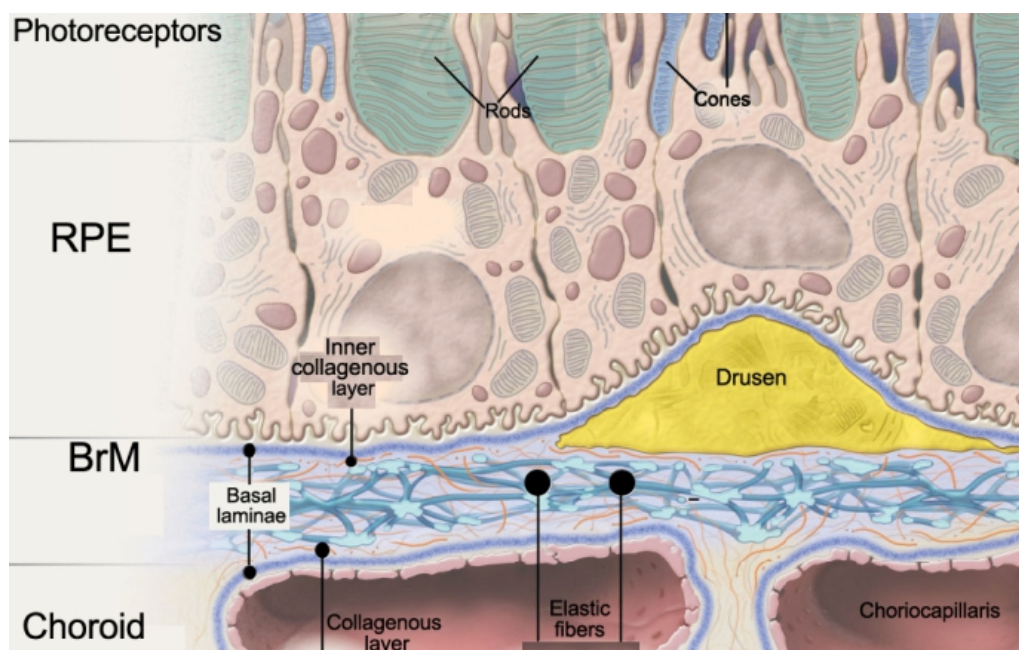


Figure 1.2: Schematic of a druse formed between Bruch's membrane (BM), the innermost layer of the choroid and the retinal pigment epithelium (RPE), which is the outermost layer of the retina. Directly adjacent to the RPE are the photoreceptors (rods and cones). Schematic from Lo Giudice et al.¹⁰

choriocapillaris, RPE detachment and subsequent neovascularization of the choroid.^{12,13} Frequency and size of drusen are hallmarks for 'dry' (non-exudative) AMD. Drusen form a pathophysiological barrier between the choroid and retina and thus negatively influence the visual cycle. Drusen development and formation has been described in histopathological studies.^{14,15} Typically, an accumulation of autofluorescent (AF) by-products (lipofuscin and melanolipofuscin) within the RPE can be observed during the physiological aging, as well as during AMD progression. However, very little has been reported about AF-particles sometimes observed within drusen, their origin and potential impact on drusen formation.¹⁶⁻¹⁸

The more severe form of AMD is the 'wet' (exudative) form, where the choroid undergoes aggressive neovascularization often caused by the action of vascular endothelial growth factor (VEGF). This uncontrolled growth of vasculature often results in a detachment of the retina, with especially devastating effects on the macula. Additionally, a degeneration of photoreceptors and a loss of $\sim 50\%$ of retinal ganglion cells, which are specialized neurons in the outer retina and essential for the signal transduction to the visual cortex, have been reported.^{19,20} Loss of retinal ganglion cells significantly enhances the destructive phenotype of AMD in patients, mostly because here, the cell type responsible for visual signaling is affected. Signal transduction in neurons, also in the retina, requires the

existence of a specialized axonal microdomain, the axon initial segment (AIS). The AIS has been well-described in structure and function in central nervous system neurons,²¹ yet little is known about its existence, location and molecular composition at retinal ganglion cells. Therefore, a proof-of-principle subproject of this thesis highlighting the great advantage of the new imaging technique, was the visualization of the molecular composition and location of the AIS in this specific subset of retinal ganglion cells.

Presently, a few pharmaceuticals (VEGF-inhibitors: Pegaptanib, Bevacizumab, Ranibizumab and Aflibercept) are used for AMD-treatment in order to slow down or potentially stop the progress of the disease. However, controversial studies have been published concerning the tendency of Bevacizumab (Avastin) and Ranibizumab (Lucentis) accumulating within RPE-cells.^{22,23} Accumulation within RPE-cells is risky as VEGF molecules should be bound outside cells in order to prevent neovascularization of the retina. Whether accumulation within RPE-cells has an independent toxic effect is not known as well. Moreover, it is assumed that due to its smaller size, Ranibizumab may penetrate the retina more effectively compared to Bevacizumab. Based on these observations, the a similar efficiency of the pharmaceuticals was questioned. As a result, Ranibizumab was considered to be more effective compared to the 'offlabel', but considerably less expensive used drug Bevacizumab. A subsequent study, which proves that Ranibizumab is superior to Bevacizumab for treating AMD, has not been published yet.

Based on this knowledge, the question was raised whether there is a possibility to detect potential pharmaceutical accumulation within cells on the super-resolution level - ideally *in vitro* - in order to compare the effectiveness of different pharmaceuticals available for AMD-treatment. Moreover, a more detailed study of the components forming drusen and AF-material is highly desirable in order to gain a better understanding of AMD-development and risk-factors at the molecular level. As a result, a suitable imaging method was sought, which is capable of visualizing the various aspects of this study simultaneously. This included the simultaneous imaging of AF-structures combined with additional fluorescence labels, time-resolved live-cell imaging, high resolved structural information in 3D and also super-resolved position information of sparse target distributions.

Standard fluorescence microscopy and immunohistochemistry have already been utilized to study the composition of drusen.²⁴ However, as the spatial resolution is limited due to diffraction, it is not possible to resolve AF-structures at an appropriate level of detail. Other imaging methods such as laser scanning²⁵ and electron microscopy²⁶⁻²⁸ have been applied to study drusen in detail, but there is no data available about frequency, size and behavior of AF-structures within drusen.²

An imaging method, which is capable to circumvent the resolution limit and able to deal with AF-structures is Structured Illumination Microscopy (SIM)^{29,30}, which was already proven to be a promising tool for high resolution imaging of AF-granules within the RPE.^{31,32} SIM shifts frequencies, which are not transferred by the imaging system into a transferable range based on the principle of the Moiré-effect. Thus, the resolution is increased significantly compared to standard fluorescence microscopy and can be easily conducted in 3D.³³ As a result, SIM allows a much more differentiated analysis of AF-particles. Moreover, SIM already provides a sufficient image quality by applying relatively low laser intensities on the specimen, which is especially important for *in vitro* imaging.³⁴ However, the resolution is limited to ~ 120 nm, but most biological processes take place on the nanometer level. In order to gain more insights into drusen composition, an imaging method providing higher resolution is required. Such a technique would also be applicable for visualizing the spatial distribution of single pharmaceutical molecules within live RPE-cells.

Single Molecule Localization Microscopy (SMLM) methods (e.g. PALM/FPALM,^{35–37} RPM,^{38,39} SPDM,⁴⁰ STORM^{41–44}) currently provide the highest spatial resolution in wide-field fluorescence microscopy. The resolution achievable with SMLM-methods is currently within the 10 nm range. These approaches are based on the general principle of optical isolation of the diffraction limited images of point emitters due to differences in spectral signatures such as fluorescence lifetime,⁵ photo-switching behavior,⁴⁵ differences in the absorption/emission spectrum,⁵ photo-bleaching,⁴⁶ and blinking.⁴⁷ Spatial positions of optically isolated single emitters, whose intensity distributions do not overlap within a diffraction limited area, can mathematically be approximated by a center of mass calculation of a fitted Airy or Gaussian function. Summing up positions of all single emitters recorded for up to several thousand frames, results in a super-resolved position map, which can be further processed to visualize structural details.

Nevertheless, these methods also have their limitations: Imaging of AF-structures is highly challenging when applying SMLM-methods as switching of AF-fluorophores remains challenging. Furthermore, most SMLM-imaging methods rely on very high laser-intensities, which are highly destructive and make experiments on live preparations difficult, especially over longer durations. Further, as SMLM-methods deliver only position information and no 'real' images, visualization methods are necessary in order to reveal the underlying structure. In the case of sparsely labeled target structures this might even be impossible. Without any contextual information e.g. drug localization within a specific cell compartment no biological/medical relevant conclusions can be drawn.

The combination of SIM and SMLM would allow correlating single molecule position

information directly with the super-resolved structural information of a target structure within a biological sample. The difficulty remaining is imaging the same region of interest (ROI) using two different physical setups. Therefore, a combination of these two high resolution imaging techniques in a single instrument is highly desirable not only to access above described medical motivated question but also to analyze various biological nano-structures.¹

To combine the advantages of both approaches, a custom microscope setup was developed to provide SIM and SMLM acquisition modes. This 'Combo'-microscope setup is able to fulfill all requirements specified above and is able to deal with the questions motivated. Thus a new, powerful tool for super-resolution imaging is now available. Revealing artifacts, which may be introduced during the imaging and reconstruction process, is an additional benefit of combining these two methods.^{1,6,8,48}

A detailed description of each component of the custom setup is presented in this thesis (chapter 3.2). The description also includes several additional fully-automated and software-controlled features, which were developed in order to speed up and simplify the imaging process. A user-friendly graphical interface of all software-controlled features is also outlined.

A detailed characterization of AF-structures within drusen in histological retinal sections by applying SIM was carried out (section 4.1). The impact of these results on drusen origin and development are discussed (section 5.1). The complementary features of SIM and SMLM will be identified (section 2.1.6) and the impact of revealing introduced artifacts is exemplarily depicted and discussed (section 4.2 and 5.2.2). A proof of principle of the newly developed 'Combo'-microscope is demonstrated using retinal sections (section 4.3) and RPE-cells *in-vitro* (section 4.4). Potential application of the microscope in life-science as a useful and advanced imaging method is discussed as well (section 5.2). Finally, future experiments and procedures for dealing with current biomedical questions concerning AMD treatment with VEGF inhibitors are outlined in detail (section 5.3.2).

2.1 Optical Imaging

Every imaging system is only able to transmit a certain bandwidth of spatial frequencies due to limiting factors such as diffraction and aberrations, which are direct consequences of the wave-nature of light. Chromatic and spherical aberrations are generally not a limiting factor in modern optical imaging systems as high sophisticated lens systems built into objectives are able to correct most chromatic and spherical shift in the focal plane. The limiting factor 'diffraction' is still highly challenging in optical imaging and is the reason for a fundamental resolution limit described by Abbe and Rayleigh (λ is the wavelength; NA: numerical aperture):^{3,4}

$$\text{Abbe : } d = \frac{\lambda}{2 \cdot NA} \quad (2.1) \quad \text{Rayleigh : } d = \frac{1.22 \cdot \lambda}{NA} \quad (2.2)$$

In microscopy the aperture given by a lens (objective) can mathematically be considered as a single circular slit though the size of the lens is much larger compared to the wavelength. Nevertheless, diffraction also occurs at the edges and leads to a diffraction pattern (Fraunhofer pattern) projected into its focal plane. The lens is only able to collect a certain solid angle and therefore only a certain fraction of the diffraction pattern. The collection efficiency of lenses is dependent on the wavelength of incident light and the maximum angle where marginal rays are still captured (numerical aperture: $NA = n \cdot \sin \alpha$ with n : refractive index of medium between objective and cover-slip, α : max. opening angle between marginal rays and optical axis). Higher orders of the Fraunhofer diffraction pattern are 'cut-off' by the optical imaging system (low-pass filter) resulting in an information loss in the image formation.

2.1.1 Point Spread Function (PSF)

Due to diffraction, imaging of an idealized point like object (e.g. a single fluorophore) located in the object plane with a lens results in a Fraunhofer intensity diffraction pattern within the image plane (blurring). This observation is the impulse response of the optical system, which is mathematically described by the point spread function (PSF). As the PSF is fundamentally band limited, only a certain band-width of frequencies is transmitted by the optical system. Ideally the diffraction pattern should contain all spatial frequencies contributing to the original object. As a result, information of fine details of the object structure get lost. Assuming a homogeneous illumination (e.g. Koehler illumination, shift-invariance of PSF) the final image $A(\vec{x})$ can mathematically be described as a convolution of the original object $O(\vec{x})$ with the PSF(\vec{x}) of the system (equ. 2.3).

$$A(\vec{x}) = (O \otimes PSF)(\vec{x}) \quad (2.3)$$

Each point within the object plane is convolved with the PSF. As the point emitters are incoherent, intensities emitted can be added linearly within the image plane. Hence, imaging of an object, which consists of a large number of point emitters, can be describes as a linear system. Knowledge about the PSF of the system theoretically allows a deconvolution of the gained image in order to improve resolution of the image by restoring information of the original object. However, in reality noise sources and the 'cut-off' of higher spatial frequencies make this problem a difficult endeavor. Therefore, the challenge to retrieve the original object from the microscopic image is highly challenging and only possible within the band limit of the optical transfer function (OTF, see section 2.1.2).

In the case of a circular aperture (e.g. a lens) the PSF is an Airy pattern, which is mathematically described by the Airy function. The Airy disc (center maximum) is mathematically generally approximated by a 3D Gaussian or normal distribution. The full width of half maximum (FWHM) of the fitted function then qualifies the achievable resolution of the optical system. However, other factors such as signal-to-noise ratio also influence the achievable resolution of the system.⁴⁹

2.1.2 Optical Transfer Function (OTF)

The Fraunhofer diffraction pattern is the Fourier transform of a point like object. A collecting lens functions as a Fourier transformer (Fourier lens). The Fourier transform of an idealized point object described by a delta-function is a constant in Fourier space and therefore contains all frequencies. Assuming no diffraction, an object imaged through a lens would be mapped identically within the image plane. The Fourier transform of the delta function in Fourier space is then a constant over the whole frequency space. As a

result the image contains all details (spatial frequencies) describing the object. However, a lens captures only a certain angle of the incident em-wave, resulting in the cut off of higher orders of the diffraction pattern (higher spatial frequencies). Therefore, the Fourier frequencies are also limited characterized through a 'cut-off' frequency, which defines the resolution of the optical system. Higher frequencies are not transferred by the optical imaging system. The Fourier transform of the PSF is the optical transfer function (OTF), which describes the correlation between incoming and outgoing signal within frequency space (equ. 2.4).

$$OTF(\vec{k}) = \mathcal{F}(PSF(\vec{x})) \quad (2.4)$$

As described in the prior section the image formed within the image plane is mathematically a convolution of the object with the PSF of the system. In Fourier space a convolution corresponds to a simple multiplication, which generally simplifies image reconstructions (equ. 2.5).

$$\mathcal{F}[A(\vec{x})] = \int_{-\infty}^{\infty} O(\vec{k}) \cdot PSF(\vec{k}) d\vec{k} = \mathcal{F}[O(\vec{x})] \cdot OTF(\vec{k}) \quad (2.5)$$

As described, an optical system functions as a lowpass filter and thus limits the transferable information. Therefore, the detectable Fourier frequency range is also limited, which is denoted as the 'cut-off' frequency ω_{max_F} in Fourier space and ω_{max_P} in position space (equ. 2.6). The inverse of ω_{max_P} is the minimal distance, which can be still resolved in position space.⁴⁹

$$\omega_{max_F} = 2\pi\omega_{max_P} = -\frac{2\pi}{\lambda} \sin \alpha_{max} \quad (2.6)$$

2.1.3 Fluorescence Microscopy

Fluorescence and Autofluorescence

Fluorophores are functional groups, which possess the ability to spontaneously emit a photon ($E = h \cdot \nu$) after absorption (fluorescence). On the atomic level, an absorbed photon leads to discrete transition of an electron from its current electronic state S_0 to a state of higher energy S_1 (excited state) within a time range of femtoseconds. The electron is able to stay within the excited electronic state for a few nanoseconds (fluorescence lifetime $\tau = 1 - 5$ ns) before it undergoes an internal conversion (IC) back to a lower and energetically more favorable electronic state. The energy difference is irradiated as a 'fluorescent'-photon of characteristic wavelength/energy. Characteristic for fluorescence is

the longer wavelength (less energy, lower frequency) of the emitted 'fluorescent'-photon compared to the absorbed photon (Stokes shift). The energy difference is released in form of heat due to vibrational relaxation (VR, picoseconds) between different vibration states within one electronic state of the fluorophore. VR occur as the electron transition has disturbed the existing equilibrium of charges within the atom, which directly results in vibrations of the nuclei. Intersystem crossings (ISC) between a singlet S and a triplet state T are less probable - nevertheless, they occur sometimes. The lifetime of a triplet state T_0 (microseconds) is much longer compared to the lifetime of a fluorescent state and may result in non-radiative relaxation or phosphorescence. Due to the longer lifetime, it is also possible that the fluorophore undergoes conformational changes e.g. as a result of a chemical reaction with other atoms/molecules and thus loses its ability to fluoresce (photo-bleaching).⁴⁹

Fluorophores such as Alexa dyes are used in fluorescence microscopy in order to mark target structures. Generally fluorophores are attached to an antibody (AB), which specifically binds to a biological structure of the specimen (antibody-antigen reaction). Other fluorophores, which are also often used in fluorescence microscopy, are special proteins such as the Green Fluorescent Protein (GFP) or derivations of it (YFP, RFP, CFP). The GFP gene is fused into the DNA-sequence of the target protein via a vector and thus is also expressed. Therefore, the target protein is able to fluoresce after excitation. This labeling method is only minimal invasive and thus also often used for *in vitro* imaging experiments. However, fluorescence emission of dyes is also highly depending on the surrounding micro-environment. An overview about fluorescent dyes and embedding media was published lately.⁵⁰

Autofluorescence (AF) is fluorescent light emitted by biological objects without additional labeling necessary. Generally AF is an unspecific source of fluorescence often e.g. introduced by fixation processes of the sample. However, there are also specific and well-defined biological structures, which autofluoresce. This AF may be exploited in order to visualize structures without additional artificial labeling methods.

Fluorescence Microscopy

Fluorescence microscopy is a widely used widefield microscopy method, which provides a unique, high contrast mechanism based on specific labeling of target structure. Labeling is either performed using antibody, which specifically tag protein distributions, with fusion-proteins or by exploiting AF-signals of specific biological structures.

Fluorescence microscopy exploits the Stokes shift (fig. 3.2), in order to separate excitation signal from the much weaker emission signal. Separation is conducted by special

dichromatic filters, which separate incident light and emitted fluorescence light due to wavelength/frequencies (see fig. 3.1). A more detailed description can be found in my diploma thesis.⁵¹

Though standard fluorescence microscopy has been proven to be a powerful tool in life-science a high demand for imaging below the diffraction limit has developed. As it is not possible to break this fundamental limit, various different super-resolution approaches have been established, which are discussed elsewhere.^{5,51} This work will focus on the high resolution method Structured Illumination Microscopy (SIM) and Single Molecule Localization Microscopy (SMLM) methods (see section 2.1.4 and 2.1.5).⁴⁹

2.1.4 Structured Illumination Microscopy (SIM)

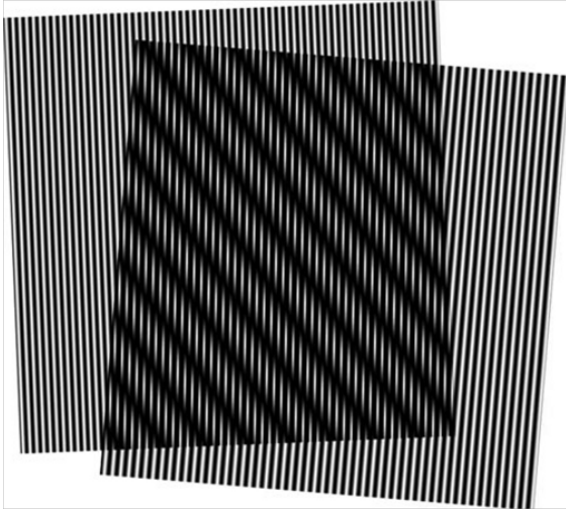


Figure 2.1: *Moirè-Effekt: Overlaying two fine structures result in a coarse, but resolvable structure. If the coarse structure (e.g. detected image) as well as one of the finer structure (e.g. illumination pattern) is known, the other fine structure (e.g. object information) will be calculable. From Rossberger et al.*²

SIM is a widefield fluorescence microscopy method, which illuminates the object structure with a pattern. This method yields a lateral resolution typically twice as high as in commonly used wide-field fluorescence microscopes, in which resolution is limited to about half the wavelength of excitation light.^{29,30} The most descriptive way to illustrate the resolution improvement may be explained by the Moirè-effect (fig. 2.1). Two overlaying gratings result in a coarser (Moirè-)structure, which can be easily resolved. In practice, an object is illuminated with an fine but known illumination structure (e.g. a sinusoidal illumination pattern). The coarse grating is the imaged structure, which contains the object structure, which contains the object structure

as well as a illumination structure. As the coarse imaged structure and the illumination pattern is well-defined, the fine object structure (i.e. the sample structure) can be back calculated. The illumination can be realized by a physical grating, a spatial light modulator or by an interferometer, which is the method used in this work (section 3.1).

The sinusoidal illumination pattern (typically 350 nm period) is modified in phase and orientation. In the case of two beam interference the phase is usually shifted to three different positions by $1/3$ of the period of the illumination pattern ($1/3 \cdot 350$ nm), which would add up to an image obtained for a homogeneous illumination. In order to achieve an isotropic resolution in the lateral plane the illumination pattern is rotated to three different angles (usually 0° , 60° , -60°). Thus typically nine images for each reconstructed high-resolved 2D image need to be acquired, which are composed of three phase shifted images for three different orientations of the illumination pattern.

There are no special requirements for fluorescent labeling as fluorophores do not need to be photo-switchable. Commercially available fluorophores already express a sufficient signal intensity at low laser-intensities (focal plane intensity: ~ 100 W/cm²). Furthermore, SIM is able to image well-defined autofluorescent (AF) structures. In this case, no additional labeling is necessary at all in order to visualize structures.

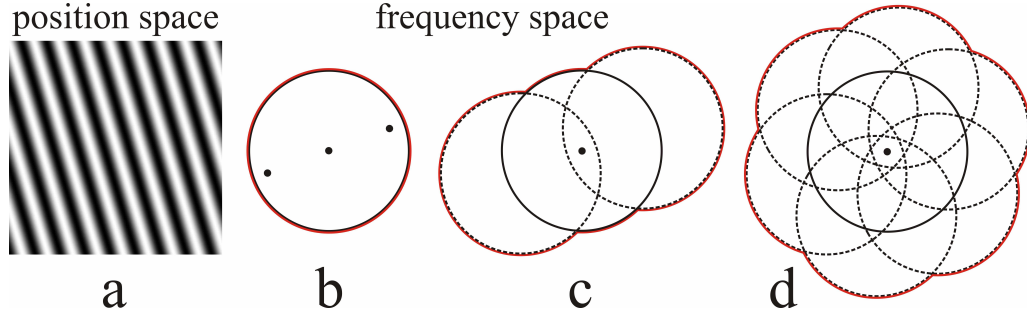


Figure 2.2: Enhancement of resolution with SIM: **a**: Sinusoidal illumination pattern in position space. **b**: The Fourier transform of the illumination pattern are three delta peaks within Fourier space. As a result three copies of the object are generated. The red circle denotes the limited frequency range, which is transferable by the optical system. **c**: Shifting of the three copies to their original position and thus extending the range of transferable frequencies. **d**: Rotation of the grating by different angles leads to an isotropic resolution improvement. From Best *et al.*³²

A more mathematical approach deals with the description of the imaging process as a Fourier transformation of the image information into frequency space as derived in section 2.1.2. As discussed the range of frequencies contributing to the image formation is limited to a specific cut off frequency in Fourier space (limited OTF). SIM is based on a spatial frequency shift of information into a range, which is transferable by the objective lens. Thus information of high, but usually non-resolvable frequencies is detectable by the objective lens.^{29,32,52,53}

An object $O(\vec{x})$ (e.g. fluorophore distribution) is illuminated with a sinusoidal intensity pattern $I_{ill}(\vec{x})$ in position space. The image $A(\vec{x})$ in position space is then the result of a convolution of the Object $O(\vec{x})$ and illumination pattern $I_{ill}(\vec{x})$ with the PSF(\vec{x}) of the optical system (equ. 2.7).

$$A(\vec{x}) = [(O(\vec{x}) \cdot I_{ill}(\vec{x})) \otimes PSF(\vec{x})] \quad (2.7)$$

The image in Frequency space $\tilde{I}(\vec{k}_g)$ is then a convolution of the object $\tilde{I}(\vec{x})$ with the illumination pattern $\tilde{I}_{ill}(\vec{k}_g)$ followed by a multiplication with the OTF(\vec{k}_g) (equ. 2.8, $|\vec{k}_g| = 2\pi/g$ with g : grating constant of sinusoidal pattern).

$$\tilde{A}(\vec{k}_g) = \mathcal{F} [PSF(\vec{x}) \otimes [O(\vec{x}) \cdot I_{ill}(\vec{x})]] = OTF(\vec{k}_g) \cdot [\tilde{O}(\vec{x}) \otimes \tilde{I}_{ill}(\vec{k}_g)] \quad (2.8)$$

The sinusoidal illumination pattern in position space can be described with a cosinus-function as follows:

$$I_{ill}(\vec{x}) = \left[1 + \cos(\vec{k}_g \vec{x} + \varphi) \right] \quad (2.9)$$

$$I_{ill}(\vec{x}) = \frac{1}{2} (e^{ix} + e^{-ix}) \quad \text{and} \quad \delta(k - a) = \frac{1}{2\pi} \int e^{i(xk - xa)} dx \quad (2.10)$$

Using the identities in 2.10, the Fourier transform of the sinusoidal illumination pattern $\tilde{I}_{ill}(\vec{k}_g)$ becomes a sum of three delta-function (fig. 2.2) in frequency space.

$$\tilde{I}(\vec{k}) = 2\pi \cdot I_0 \cdot \left[\delta(\vec{k} + e^{i\varphi} \delta(\vec{k} - \vec{k}_g) + e^{-i\varphi} \delta(\vec{k} - \vec{k}_g)) \right] \quad (2.11)$$

The convolution of the object with the illumination pattern then results in an image $\tilde{A}(\vec{k})$, which contains three copies $\hat{O}(\vec{k})$ of the object, where each copy is shifted according to the position of the delta-function in Fourier space (equ. 2.12).

$$\tilde{A}(\vec{k}) = OTF(\vec{k}) \cdot \frac{I_0}{2\pi} \cdot \left[\hat{O}(\vec{k} + e^{i\varphi} \hat{O}(\vec{k} - \vec{k}_g) + e^{-i\varphi} \hat{O}(\vec{k} - \vec{k}_g)) \right] \quad (2.12)$$

By shifting the object information, frequencies, which were prior beyond the cut off frequency (fig. 2.2), are now transferred by the imaging system. Thus, an resolution improvement by about 2-fold can be achieved. However, the acquired image represents an superposition of these three copies, which need to be separated during further post-processing of the image. For further details see Heintzmann *et al.*,²⁹, Karadaglic *et al.*,⁵⁴ and Kubitscheck *et al.*⁴⁹

Image Reconstruction

In one acquired image three copies of the original object are superimposed due to the convolution of the object with the sinusoidal illumination pattern in Fourier space. Three images of different phases are recorded for each orientation of the grating. As a result three differential equations with different phases are defined. In order to separate the copies of the object, solving the equation system delivers the original positions of the copies.

For reconstruction in frequency space, custom software was used as described previously.^{29,32,55} For reconstruction in position space, custom software developed by Gerrit Best (Kirchhoff Institute for Physics, University of Heidelberg) was used.⁵⁶

2.1.5 Single Molecule Localization Microscopy (SMLM)

Various different variants of SMLM-methods such as PALM³⁵/FPALM,^{36,37} RPM,^{38,39} SPDMPHymod^{38,40,57,58} and STORM^{41,42}/dSTORM^{43,44} currently exist. All these methods are based on the principle to activate only one fluorophore within a diffraction limited area in the same image frame. Each of these diffraction limited signals represents a measured point spread function (PSF) of the microscope. As PSFs of two different fluorophores are optically isolated on a detector, it is possible to fit a Gaussian function. Instead of the full width of half maximum (FWHM) center of maximum intensity (center of mass) can be calculated, which results in a theoretically infinite resolution.^{36,41,42} However, a resolution improvement of a factor ~ 10 has been proven to be realistic as the localization accuracy is highly dependent on signal, background and noise levels. Recording several thousand images - each frame containing only a sparse number of fluorescing fluorophores - allows generating a map of single molecule positions. This point-like image needs to be further processed in order to visualize structural information accounting the accurate single molecule positions. This procedure described allows to circumvent the fundamental diffraction limit proposed.^{3,4}

The SMLM-methods mentioned above vary in terms of achieving only a sparse number of molecules being in a fluorescent state per frame. SPDMPHymod^{38,40,57,58} applies high laser intensities (focal plane intensity $\sim 10 \text{ kW/cm}^2$), which transfers most of the fluorophores into a dark (non-fluorescent) state D from which they recover stochastically into the ground state G (fig. 2.3). From the ground state G fluorophores can be excited again resulting in up to several thousand electron transitions between ground and bright (fluorescent) state B. Provided negligence of losses the number of electron transition is directly proportional to the number of detected photons on the camera chip. Ideally only one fluorophore is in a bright state B within a diffraction limited area. This method works successfully with commercially available standard fluorophores and some standard embedding media. Fluorophores are able to recover several times before they are irreversibly photo-bleached. Rate of recoveries can be enhanced using oxygen scavenging systems such as 'switching buffer'.⁵⁹ Multiple detection of same fluorophores automatically increase the localization precision and are thus feasible.

Image Reconstruction

The following paragraph has been published in my diploma thesis: '*Multi-color Localization Microscopy with a Single Excitation Laser Line using Far-Red Dyes*',⁵¹ which describes the fitting and reconstruction process of SMLM datasets.

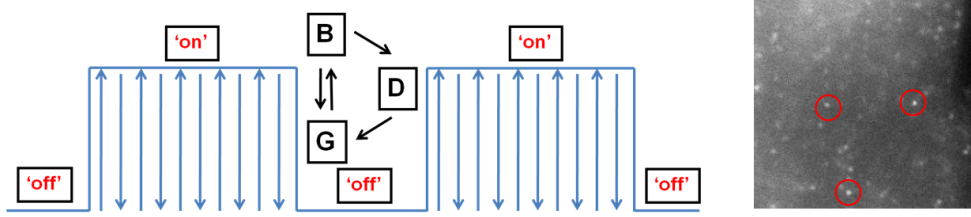


Figure 2.3: **Left:** Fluorescence is the result of the irradiation of photons after electron relaxation from an excited state to an energetic more advantageous state. One event detected by the camera consist of several thousand photons directly correlated to an equal number of electron transitions. When the fluorophore is excited from a ground (non-fluorescing) state (G) enters a bright state (B) the emitted photon it is detected by the CCD-chip of the camera. Afterwards the fluorophore enters a triplet state, a dark state (D) or it is irreversibly photo-bleached. Fluorophores can undergo several of switching cycles between G- and B-state until they are either photo-bleached or undergo chemical reactions with other molecules. If the fluorophore enters a dark state it is able to recover slowly from this state and thus can be again detected as a single molecule event. **Right:** Single molecule events per frame as they appear during the acquisition process.⁵¹

Each frame including all its detected events is analyzed individually. Background values for each event are evaluated by averaging over 10 frames before an event occurs and then subtracting this value. A bandpass filter, whose frequency is chosen according to the expected frequency spectrum of the fluorophores (spot size: FWHM of the Gaussian) smooths the difference image. Then a local variable threshold is applied to the image to isolate the single molecule events. This threshold is an estimate of the photon-counting-noise in each pixel (standard deviation of the Poisson distribution) multiplied with a scale factor chosen by taking integration time and em-gain into account.³⁸

A standard labeling algorithm selects the events from the thresholded image, numbers those consecutively and calculates the center of intensity, which gives the starting coordinates for the fitting process. The localization of each fluorophore is then estimated by fitting a Gaussian model function:⁵¹

$$f(\vec{x}, \vec{y} | A, \sigma, x_0, y_0, b, b_x, b_y) = A \cdot e^{-\frac{(x-x_0)^2 + (y-y_0)^2}{2\sigma^2}} + b + \frac{\partial b}{\partial x}(x - x_0) + \frac{\partial b}{\partial y}(y - y_0) \quad (2.13)$$

with $b_x = (\frac{\partial b}{\partial x})$ and $b_y = (\frac{\partial b}{\partial y})$. The fitting function $f(\vec{x}, \vec{y} | \vec{p})$ consists of a 2D Gaussian term and is extended with three additional terms. The first one is a constant describing the background level, followed by two terms taking weak gradients of the background into account.

This model function is fitted to a 15x15 pixel ROI extracted at the position of each detected event. The fit is performed using the Levenberg-Marquardt algorithm^{60,61} implemented in Scipy⁶² to solve the weighted least squares problem:

$$\left\| \frac{f(\vec{x}, \vec{y} | \vec{p}) - \vec{d}}{\vec{w}} \right\|^2 \quad (2.14)$$

with $\vec{p} = (A, \sigma, x_0, y_0, b, b_x, b_y)$ and \vec{d} representing the raw data. The numerator is the difference between the intensity values generated by the model function and the actual data intensity values. The whole expression is 'weighted' by the vector \vec{w} , which is the standard deviation of each pixel:

$$\vec{w} = \sigma_{readout-noise} + \sigma_{photon-counting-noise} + \sigma_{electron-multiplying-noise} \quad (2.15)$$

The error introduced by each pixel consists of two components: 'Read-out-Noise' and 'Photon-Counting-Noise', which is assumed to be Poisson distributed. Therefore $\sigma_{poisson}$ is replaced by $\sqrt{N_{Photons}}$, the standard deviation of the Poisson distribution. Minimizing this expression leads to a Gaussian intensity distribution, whose center approximately localizes each single molecule event.

The starting values for the fit are calculated as follows: The position values are obtained by the center of intensity calculation. The intensity amplitude A is the maximum value subtracted by the minimum value. The starting value for the background is the minimum intensity value. Gradients in the background level are assumed to be zero. Sigma is the expected standard deviation of an ~ 250 nm spot.

Localization Accuracy

The localization of single molecule signals is a sub-pixel accurate fitting routine. However, noise sources limit the resolution theoretically achievable. Thompson *et al.*⁶³ described very precisely all parameters influencing the 2D localization precision. Based on a least-squares fit of the intensity distribution of a single fluorophore the error of the position Δx can be approximated as follows:

$$\Delta x = \sqrt{\langle (\Delta x)^2 \rangle} = \sqrt{\frac{(\sigma_{PSF})^2 + \frac{a^2}{12}}{N} + \frac{8\pi(\sigma_{PSF})^4 b^2}{a^2 N^2}} \quad (2.16)$$

$$with (\sigma_{PSF})^2 = \frac{(FWHM_{PSF})^2}{2.35} \quad (2.17)$$

with N: photon number/pixel, a: size of pixel, b: background noise. Approximating the PSF of a single fluorophore by an Gaussian distribution σ_{PSF} can be replaced with the

FWHM. The first term accounts for the photon-counting-noise consisting of the variances of Poisson-distributed photon counts and pixelation noise. Pixelation noise is considered as photons can be only detected with an accuracy of the pixel-size. The second and usually more prominent term is accounting for background noise and can be replaced by $b^2 = N_b + (\sigma_{readoutnoise}/em - gain)^2$. Out-of-focus fluorescence and autofluorescence signals are taking into account as variance of the measured background photon level, whereas the variance of the read-out noise of the CCD-chip needs to be divided by the electron-multiplying gain of the camera if necessary. A comprehension of the derivation of this formula can be found in my diploma thesis.⁵¹

2.1.6 SMLM vs. SIM

Localization data is essentially a finite list of single molecule positions. Visualization algorithms are required to generate a structural image by connecting each position. A few numerical methods such as Gaussian-blur or triangulation provide visualization of single molecule localization microscopy data with regard to important parameters such as localization accuracy or local density.⁶⁴ However, these methods become highly challenging or sometimes even impossible, when a very low yield of single molecule positions is detected (see also section 4.2).⁵⁷

Even if the structure is well labeled, only a fraction of those single molecule signals is usually detected in SMLM. In some cases, the structure may then not be sufficiently visualized. A similar problem arises when a sparse target distribution is of interest, which inherently exhibits low labeling densities.

In both cases described, it often remains difficult to obtain structural spatial information from these images and thus to interpret images correctly. Moreover, visualization algorithms in SMLM often introduce artifacts in the generated images, which have to be considered (see section 4.2). In many cases structural information can be provided by using a microscope technique with a lower resolution in a linear excitation mode, though a second co-localizing label is necessary in the case of sparse target distributions. Artifacts occurring during the visualization process can be identified and considered appropriately for data interpretation. A comparison with conventional fluorescence microscopy may be an option to solve this problem. However, the optical resolution (~ 200 nm) may be inadequate to advantageously integrate the SMLM data.

Structured Illumination Microscopy (SIM) approaches are currently the most convenient choice in fluorescence microscopy in order to gain highly resolved structural information because this method provides a 2-fold resolution improvement (~ 120 nm) compared to standard fluorescence microscopy.^{29,30,52} SIM is also superior to the resolving power of confocal⁶⁵ or multi-photon microscopy.⁶⁶ Theoretically, SIM provides unlimited resolution when nonlinear fluorescence response is utilized.^{67–69} However, for practical applications this is quite complicated to realize. Special fluorophores with a long life time, high laser-intensities, or complicated microscope setups are generally necessary in order to achieve a high degree of nonlinearity. For practical applications the resolution of SIM is generally about one order of magnitude lower compared to SMLM.⁵

Nonetheless, an essential advantage of SIM is the opportunity to obtain images with an enhanced resolution already at low laser-intensities with conventional fluorophores. This enables in-vivo imaging including repeated imaging of the same target up to several hours or ideally even a few days.^{34,70,71} Furthermore, the imaging process is much faster, which leads to a much shorter exposure time resulting in substantially less phototoxic

Single Molecule Localization Microscopy (SMLM)	Structured Illumination Microscopy (SIM)
<input checked="" type="checkbox"/> super resolution (~ 30 nm)	<input type="checkbox"/> high resolution (~ 100 nm)
<input checked="" type="checkbox"/> single molecule position information	<input type="checkbox"/> no position information
<input type="checkbox"/> no contextual/structural information - visualization algorithm necessary	<input checked="" type="checkbox"/> contextual/structural information
<input type="checkbox"/> can not deal well with sparse target distribution/labeling efficiency	<input checked="" type="checkbox"/> can deal with sparse target distribution/labeling efficiency
<input type="checkbox"/> AF imaging very difficult	<input checked="" type="checkbox"/> AF imaging possible
<input type="checkbox"/> live-cell imaging (highly invasive)	<input checked="" type="checkbox"/> live-cell imaging (less invasive)
<input checked="" type="checkbox"/> multi-color	<input checked="" type="checkbox"/> multi-color
<input checked="" type="checkbox"/> low computing power for reconstruction	<input type="checkbox"/> high computing power for reconstruction
<input type="checkbox"/> slow imaging process	<input checked="" type="checkbox"/> fast imaging process
<input checked="" type="checkbox"/> easy beam adjustment	<input type="checkbox"/> complex beam adjustment
<input checked="" type="checkbox"/> 3D imaging	<input checked="" type="checkbox"/> 3D imaging
<input type="checkbox"/> special/switchable fluorophores	<input checked="" type="checkbox"/> no special fluorophores
<input type="checkbox"/> special embedding media	<input checked="" type="checkbox"/> no special embedding media
<input type="checkbox"/> fixation method of sample relevant	<input checked="" type="checkbox"/> no special fixation necessary

Table 2.1: *Complementarity of SMLM and SIM: Advantages and disadvantages of SMLM-methods vs. SIM are compared to each other. Check-boxes display the case when one method is superior to the other for a specific application. Both methods clearly compensate the weakness of the other one and thus complement one another in a very useful way in order to access various medical and biological motivated questions.*

damage of the biological object.^{67,69} In order to transfer fluorophores into a spectrally different state (e.g. dark), SMLM often requires either high illumination intensities when using conventional single fluorophores combined with standard preparation conditions,⁴⁰ or very special fluorophores and complex illumination schemes (e.g. PALM/FPALM). At present, time lapse live-cell or other in-vivo applications have been extremely difficult to realize. Toxic illumination intensities and switching buffers, or molecule mobility are a major problem.⁷²⁻⁷⁸ Furthermore, special fluorophore characteristics and/or buffer media needed, challenge the range of application for SMLM-methods.^{43,59,79}

Despite the more stringent restrictions in terms of specimen labeling, SMLM also exhibits benefits over SIM. Setup realization and alignment are generally much simpler compared to a SIM-setup. However, realization and alignment of a SIM setup is still less complex than focused super resolution microscope techniques such as STED⁸⁰ or 4Pi-CLSM⁸¹. Moreover, the imaging process of SIM is faster as it does not require a data stack of several thousand images as in SMLM. And finally, SMLM is capable of 3D imaging providing a highly enhanced z-sectioning compared to SIM. Nevertheless, it is necessary to generate an astigmatism by introducing additional optical elements into the detection beam-path and special algorithms are needed for SMLM imaging in order to gather 3D information.^{37,39,44} So far, imaging of thicker 3D structures (beyond the $\sim 10 \mu\text{m}$ range) has been almost impractical. A possibility to overcome this problem is the use of a perpendicular illumination e.g. light sheet microscopy.^{55,82,83}

Moreover, both methods, SMLM^{57,84-87} and SIM^{32,33,88} allow imaging of multi-color labeled targets, though SIM benefits from a simple sample preparation as no special fluorophores and embedding media are needed.

As previously described SIM is able to access and resolve autofluorescent (AF) structures within the retina on a high resolution level.^{2,31,32,88} Thus, SIM allows a differentiated analysis of AF tissue. In comparison, it is usually quite challenging to image AF structures with SMLM, as bleaching and switching of fluorophores contributing to the AF signal are difficult to control.³⁹

2.2 Biological Models

2.2.1 Anatomical Structure of the Human Eye

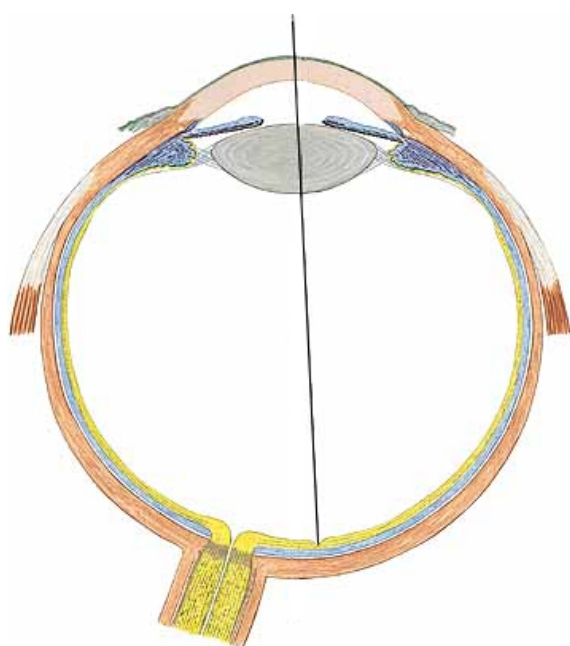


Figure 2.4: *Cross section of the human eye: The most outer layer consists of sclera and cornea, followed by the uvea and the retina, which is the most inner layer. Uvea can be further split into iris, choroid and ciliary body. Spot of sharpest vision within the retina is the Fovea. Optical signals of incident light is transduced via the retina through the optic nerve to the brain. The optic disc is the blind spot. The visual axis is indicated. From Trepel.⁸⁹*

The outer layer of the bulbus oculi (eye) consists of the sclera and the cornea. The sclera covers nearly the entire bulbus and migrates into the transparent cornea located in the front of lens and pupil. The middle layer is the uvea consisting of the iris, the choroid and the ciliary body. The iris is responsible for the physical adjustment of the pupil to different intensities of incident light (adaptation). The ciliary body is able to change the refractive index of the lens (accommodation) in order to focus objects of different distances onto the retina, which is the most inner layer of the eye. The choroid (choriocapillaris) consists of three histological distinct layers: Bruch's Membrane (BM) is the innermost layer adjacent to the retinal pigment epithelium (RPE), followed by the lamina vasculosa, and the lamina suprachoroidea. The choroid supplies the retina with oxygen, plays an important role for heat transfer and also for the metabolism of the retina. BM forms a physiological barrier between the choroid and the retina. The area of highest acuity in the human retina is the macula (~ 5 mm), which is located in the direct vicinity to the optic nerve head and possesses the highest density of photoreceptors within the retina. The inner central region of the macula is the fovea (~ 0.5 mm), which provides the highest spatial resolution and thus is the site of sharpest vision. The blind spot (optic disc) is located at the junction of the retina and the optic nerve. The optic nerve is composed of retinal ganglion cell axons that bundle together at the optic disc and thus leave the retina and project towards the central nervous system.

The outer layer of the bulbus oculi (eye) consists of the sclera and the cornea. The sclera covers nearly the entire bulbus and migrates into the transparent cornea located in the front of lens and pupil. The middle layer is the uvea consisting of the iris, the choroid and the ciliary body. The iris is responsible for the physical adjustment of the pupil to different intensities of incident light (adaptation). The ciliary body is able to change the refractive index of the lens (accommodation) in order to focus objects of different distances onto the retina, which is the most inner layer of the eye. The choroid (choriocapillaris) consists of three histological distinct layers: Bruch's Membrane (BM) is the innermost layer adjacent to the retinal pigment epithelium (RPE), followed by the lamina vasculosa, and the lamina suprachoroidea. The choroid supplies the retina with oxygen, plays an important role for heat transfer and also for the metabolism of the retina. BM forms a physiological barrier between the choroid and the retina. The area of highest acuity in the human retina is the macula (~ 5 mm), which is located in the direct vicinity to the optic nerve head and possesses the highest density of photoreceptors within the retina. The inner central region of the macula is the fovea (~ 0.5 mm), which provides the highest spatial resolution and thus is the site of sharpest vision. The blind spot (optic disc) is located at the junction of the retina and the optic nerve. The optic nerve is composed of retinal ganglion cell axons that bundle together at the optic disc and thus leave the retina and project towards the central nervous system.

2.2.2 Retina and the retinal pigment epithelium (RPE)

The retina is essential for the vision process. It can be distinguished into ten different layers. The RPE is directly adjacent to the choroid (fig. 1.1 and 2.2.4). The RPE is followed by a layer containing specialized neurons, the photoreceptors (rods and cones, photoreceptor outer segments, external limiting membrane, outer nuclear layer). Within the fifth layer (outer plexiform layer) the endings of rods and cones form synapses with the dendrites of bipolar cells (inner nuclear layer). The seventh layer contains the synapses formed between the axons of the neuronal bipolar cells and the dendrites of the following ganglion and amacrine cells (inner plexiform layer). The next layer consists of the ganglion cells (ganglion cell layer), directly followed by the nerve fiber layer, which consists of ganglion cell axons. They form the optic nerve. Finally the retina is completed by the inner limiting membrane, which also contains Mueller glia cells, the only retinal glia cell type. Mueller glia span the entire retina and play an important role for the structural integrity of the retina.

Besides essential function in the visual cycle (see section 2.2.3) the RPE also fulfills barrier and transport functions such as the transport of metabolic end products and water from the lower retina to the choroid (fig. 2.5). On the other hand the RPE supplies the retina with essential nutrients from the blood. Moreover, the RPE is responsible for the ion-concentration in the sub-retinal space in order to maintain the excitability of the photoreceptors.⁹⁰ Probably, one of the most important functions of the RPE is the phagocytosis of spent photoreceptor outer segments (POS), which are digested within the RPE. Loss of this function is also a leading cause of retinal degeneration, especially age-related macular degeneration (AMD).^{19,91,92}

Photoreceptors are specialized neurons capable of converting incident electromagnetic waves into an electrical signal. Immediately after the incidence of a photon, photoreceptors produce a membrane potential, which is forwarded towards the ganglion cells via a downward progression of the signal through various retinal cell types, cumulating at retinal ganglion cells. Their axons form the optic nerve and therefore, transmit the electrical signal towards the visual cortex for further processing. Within the retina, fully developed axon initial segments (AIS) have so far only been found at retinal ganglion cell axons (Schlueter & Engelhardt *et al.*, personal communication). Additional data has been presented, that indicated AIS-like structures at bipolar cells⁹³ and amacrine cells.⁹⁴ The AIS is the site for action potential generation in neurons,²¹ and is localized at the proximal axon. It has a major role in maintaining neuronal polarity^{95,96} and thus can be considered one of the most fundamental neuronal microdomains. On a molecular level, the AIS is defined by a high density of voltage-gated sodium channels that are anchored in the

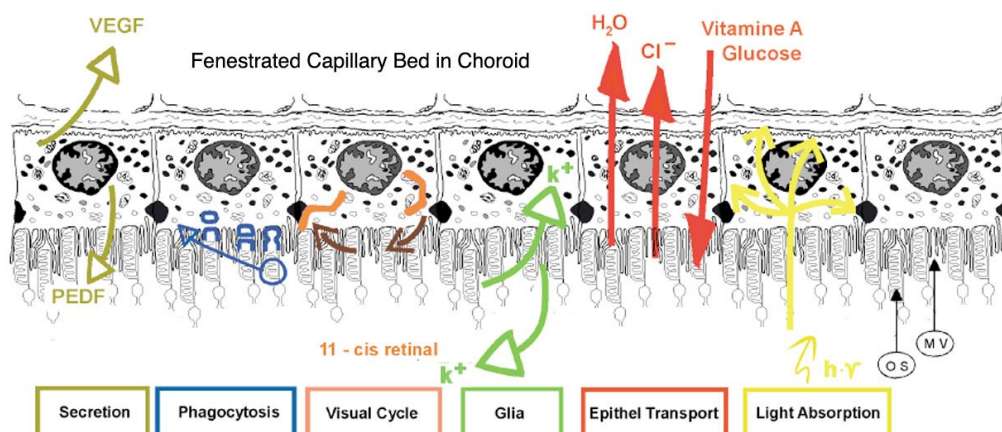


Figure 2.5: Schematic of the retinal pigment epithelium (RPE) and related transport mechanism and metabolic processes. Details can be found in the text. From Strauss *et al.*⁹⁰

membrane through a complex network of scaffolding proteins on the inside of the axonal membrane (fig. 4.16). The retinal ganglion cell AIS is the most crucial link for signal transduction from the photoreceptors to the cortex. In case of dysfunction of the AIS, e.g. due to the development of neurodegenerative disease, signal transduction is inhibited resulting in vision loss of affected patients.⁹⁷

Ankyrin-G (AnkG) is a membrane scaffolding protein and located within the AIS. AnkG functions as an adapter protein between trans-membrane proteins and spectrin, a protein connecting the ankG-complex with the actin cytoskeletal network. AnkG protein expression is restricted to the AIS, and the nodes of Ranvier, which are crucial components of action potential propagation along myelinated axons.²¹ AnkG possesses a central binding site for spectrin and is also essential for the spatial organization of different integral membrane proteins such as Ca²⁺- and K⁺-ion-channels. Synaptopodin (synpo) is an actin-binding protein. It is associated with the cisternal organelle (CO), which is composed of stacks of smooth endoplasmic reticulum and localized to the inner membrane of the AIS. Morphology and functionality synpo and the CO within the AIS of retinal neurons are not well understood, although they are assumed to play an important role in Ca²⁺ regulation and release. A study describing a co-localization of synpo and AIS within retinal ganglion cells is lacking.

2.2.3 Visual cycle

A complex signal-transduction cascade transforms an incident electromagnetic signal (photon) into an electrical signal within the retina. Along the outer segments of photoreceptors (POS), so called discs can be found. The photo-converting protein complex rhodopsin, a

G-protein receptor, is located here (aldehyd of vitamin A₁).⁹⁸ 11-cis-retinal has a C=C-double bond, which is able to absorb an incident photon within the visible spectrum. The photon initiates an electron being transferred to an excited state, but after relaxation the prior cis-form results in an 11-trans-retinal molecule (all-trans-retinal). Due to the conformation change (photo-isomerisation), opsin itself also undergoes conformational changes into meta-rhodopsin II. As a result the trans-form dissolves from the opsin-protein.

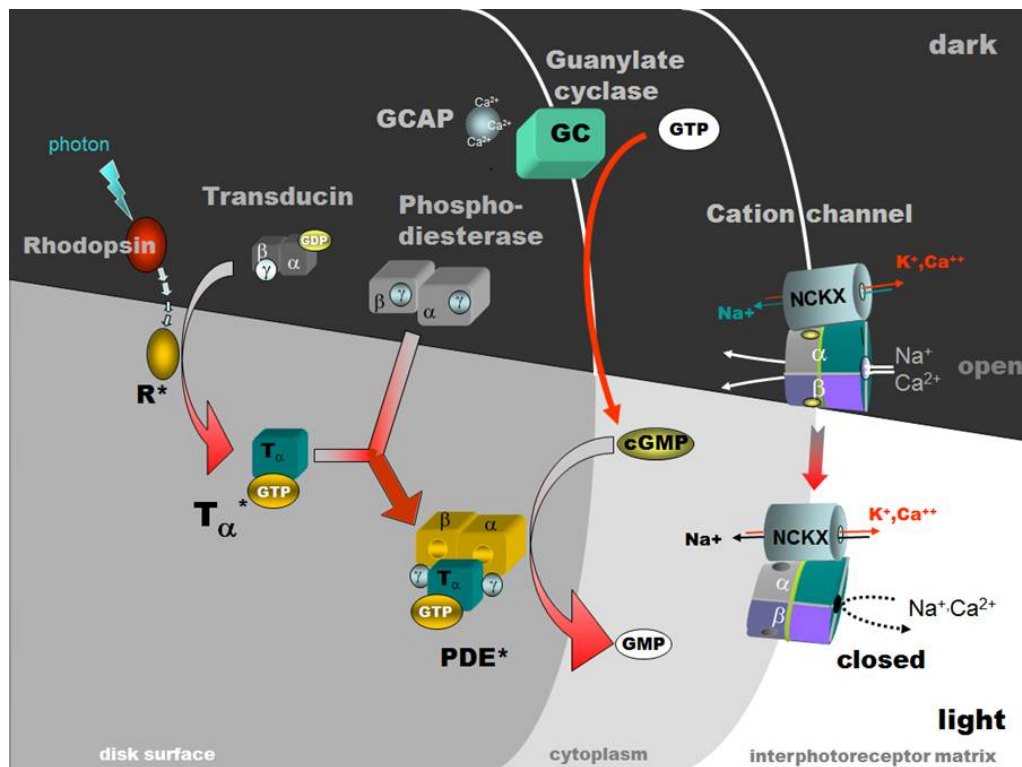


Figure 2.6: Schematic of the visual cycle: An incident photon induces a conformational change of the chromophore 11-cis-retinal, which is part of the rhodopsin complex located within the photoreceptor outer segments (POS), into 11-trans-retinal (all-trans-retinal). An enzyme cascade triggers ion-channels anchored within the POS-membrane resulting either in a hyperpolarization (light) or in a depolarisation of the membrane (dark). This in turn triggers voltage-gated Ca²⁺-channels. Ca²⁺-concentration is directly related to further signal transduction. From Webvision⁹

Subsequently, an enzyme cascade follows: Opsin triggers the activation of the regulatory protein transducin (G-protein), which itself activates the enzyme phosphodiesterase (PDE) after several additional steps. PDE converts cGMP (cyclic guanosinmonophosphat) into GMP. As a consequence the dark current between POS membrane and extracellular space is inhibited. The dark current denotes the Na⁺-ion flow into the POS through cGMP triggered ion-channels, which are closed after photon absorption. However, K⁺ current into the extracellular space is still conducted via non-gated K⁺-ion channels, which leads to a hyperpolarization of the membrane. A membrane potential of -70 mV (resting poten-

tial) can be measured (repolarisation). In the dark, the Na^+ current is not inhibited and a membrane potential of -30 mV can be observed (depolarisation, non-active rods). As the ATP-triggered (adenosintriphosphate) Na^+ - K^+ -pump actively transports Na^+ against the gradient into the extracellular space, the concentration of Na^+ within the POS is even further reduced during light exposure. The hyperpolarization effects voltage-gated Ca^{2+} channels, which are actively closed followed by a reduced Ca^{2+} concentration within POS, which is directly related to a reduction in glutamate release (neurotransmitter in synapses). The Ca^{2+} is essential for the fusion of glutamate-vesicles with the postsynaptic membrane at synapses, thus releasing the neurotransmitter into the synaptic cleft. A reduction in glutamate results either in a depolarization or a hyperpolarization of bipolar cells.

Activity of the meta-rhodopsin II is terminated by its phosphorylation. By binding again to regenerated 11-cis-retinal the opsin-complex is fully recovered and able to respond again to an incident photon.

Photoreceptors are not capable of re-isomerizing the all-trans-retinal back into its 11-cis-form as they do not express the necessary re-isomerase. This procedure is conducted for rods within the RPE cells and for the cones either in the RPE or by Mueller glia cells. The all-trans-retinal is reduced to 11-trans-retinol (vitamin A_1) within the POS before it is phagocytosed by the RPE, where it is oxidized back via the 11-cis-retinol into 11-cis-retinal under the influence of various different enzymes. Afterwards, 11-cis-retinal is transported back into the POS for the next vision cycle. This is a very simplified description of the visual cycle. More details can be found in Strauss *et al.* and Tang *et al.*^{90,99}

2.2.4 Lipofuscin (LF), melanolipofuscin (MLF) and A2E

Photoreceptors are exposed to a high photo-oxidative stress. Therefore, POS need to be consecutively renewed. An elemental factor in this cycle is the RPE (see section 2.2.3 above). Moreover, RPE-cells are destined for the important role to regenerate the retinoid all-trans-retinal into its cis-form. The phagocytosis of POS is assumed to lead to an accumulation of autofluorescent (AF) lipofuscin (LF) within RPE-lysosomal compartments. LF consists of lipids, retinoids and waste products.¹⁰⁰ The total number of spherical LF-granules (mean size: $\sim 1\ \mu\text{m}$) increase during the progression of the aging process and is therefore also an marker for the aging eye.¹⁰¹

Besides proteins and lipids, extraction of further components such as bis-retinoid A2E (N-retinylidene-N-retinyl-ethanolamine), one of more than twenty, mostly unknown, fluorophors within LF-granules has been shown.¹⁰² A2E is synthesized from one molecule ethanolamine (phosphatidylethanolamine) and two molecules all-trans-retinal (vitamin A aldehyde) within the POS.¹⁰³ Phagocytosis of POS and the subsequent hydrolysis leads to A2E accumulation within the RPE. Therefore, A2E and all-trans-retinal are associated with LF-

accumulation within the RPE.¹⁰⁴ However, recent investigations could not reveal a direct spatial correlation of A2E and LF within the human eye.^{105,106}

LF-granules illuminated with 470 nm excitation filter irradiate autofluorescent (AF) light in a range between 500 nm - 750 nm.¹⁰⁷ A2E was verified to fluoresce within the mentioned wavelength range.¹⁰⁸ The maximum of the emission spectrum was evaluated at ~ 600 nm, when excited with a wavelength of 400 nm and an excitation maximum at 418 nm.^{98,101} It was demonstrated that cultured RPE express LF-granules after feeding with A2E. Total number of granules was directly dependent on the added A2E concentration.

Melanolipofuscin (MLF) granules also accumulates within the RPE. Their typical appearance is an AF-ring of the similar spectral characteristics as LF, but including a dark, non-AF core, which is most likely composed of melanin. Despite some similarities it has been shown that MLF do not contain any proteins related to POS and are therefore not assumed to originate from the phagocytosis of POS as stated for LF-granules.¹⁰⁹

Nevertheless, the formation of A2E or LF-accumulation within RPE-cells is still quite controversial and their impact on cell function is not well understood.⁹⁹

2.2.5 Drusen and age-related macular degeneration (AMD)

Age-related macular degeneration (AMD) is a disease related to the aging process (onset of disease > 50 years of age). The central vision loss accompanied with this disease is the main cause of blindness in Western countries.¹¹ Different stages of AMD are distinguished: Early and intermediate stages are referred to as 'dry' AMD. Late stages of AMD are either referred to as 'geographic atrophy' (late stage of dry form) or as 'wet' AMD (exudative). 'Dry' form of AMD occurs in 80% of all cases, but is less severe compared to the 'wet' type of AMD. 5-10% of all cases linked to the 'dry' type lead to blindness.¹⁰

AMD is characterized by a sequence of pathophysiological events best characterized as follows: (i) oxidative stress and/or genetic predispositions cause insults within the retinal pigment epithelium (RPE) layer, possibly also in the choroid, which in turn leads to (ii) chronic inflammatory responses in Bruch's membrane (BM), (iii) inflammation leads to the development of an abnormal extra cellular matrix (ECM), which in turn then leads to altered diffusion between these vital retinal layers, and finally (iv) cellular atrophy due to severe impact of the changes in diffusion on the microenvironment of the retina.^{12,13}

Besides thickening of BM and damage to photoreceptors, the development of early and intermediate stages of AMD involves the formation of drusen and microdrusen, which are focal deposits between the inner collagenous layer of BM and the basal lamina of the RPE.¹¹⁰⁻¹¹³ The pathogenesis of drusen formation is still relatively unknown, but lipids and proteins and occasionally intracellular material like organelles and particles originating

from the RPE have been analyzed.^{26,28,114} There are some reports referring to AF within extracted drusen, AF within the RPE overlying drusen or AF within drusen.^{107,115,116} In a few cases, particles/granules within drusen were observed, which showed a strong AF in the visible spectrum similar to AF behavior of LF granules generally observable within the RPE. Drusen are also assumed to consist of end-products of metabolic processes. Moreover, they form a physical barrier between BM and RPE, which leads to RPE-detachment and an undersupply of the RPE by the choroid, often resulting in a focal atrophy of the RPE.² Size and total number especially of soft drusen including RPE-detachment qualify the severity of the progressing AMD.^{25,112,114,117,118}

Drusen can be classified either according to size or shape. Drusen appearing dome-shaped with well-defined borders were classified as 'hard' type (fig. 4.1), whereas drusen with poorly defined borders with endings often merging with adjacent basal linear deposits were assigned to the 'soft' type (fig. 4.2).¹⁸ A classification based on size distinguishes drusen into three categories. Drusen are categorized into smaller than $63\ \mu\text{m}$, which are generally associated with the 'hard' type, intermediate drusen, which are larger than $63\ \mu\text{m}$ and smaller than $125\ \mu\text{m}$, and into drusen larger than $125\ \mu\text{m}$, which generally appear comparable to the 'soft' type (Wisconsin grating system).¹¹⁹

Whereas the 'dry' type of AMD can not be treated until now, the 'wet' and more severe type of AMD can be stopped and sometimes vision can be improved for a short time period by a few available pharmaceuticals. The 'wet' AMD is a result of uncontrolled laminar growth of blood vessels (angiogenesis), which proliferate from the choroid into the overlying retina (choroidal neovascularization, CNV) accompanied by a detachment of the RPE. The permeability of the newly grown vessels is generally increased and such leads to a leakage of fluid into the choroid. As a result the visual center is bulged out and hemorrhages occur between RPE and choroid. Due to this processes vision loss is preassigned.

The best studied initializing factor for the uncontrolled angiogenesis is the signal molecule VEGF (vascular endothelial growth factor, 45 kD), which is mainly produced within RPE and Mueller cells.¹⁰ Five isoforms of VEGF (32 - 40 kD) are known, which originate from a alternative splicing of the mRNA. Three of these isoforms (VEGF-A₁₂₁, VEGF-A₁₄₅ and VEGF-A₁₆₅) are secreted by cells, whereas two isoforms are cell-mediated (VEGF-A₁₈₉ and VEGF-A₂₀₆).¹²⁰ This angiogenic molecule induces the signal cascade by binding to the VEGF-receptor tyrosine kinase (VEGFR) of endothelial cells, which is a transmembrane protein and assigned to the family of the enzyme-linked receptors. Activated VEGFR results in a signal transduction of the extracellular signal into the cell, which stimulates the proliferation of the cell and is responsible for vasculogenesis and angiogenesis.

AMD treatment

VEGF is the key molecule for ('wet') AMD treatment, which initially induces the undirected growth of blood vessels. A few pharmaceuticals are available for treatment, which bind VEGF and thus reduce the undirected proliferation (tab. 2.2). Ideally the progress of the disease can be stabilized or at best the visual acuity can be improved due to a degeneration of diffuse developing blood vessels.

The first pharmaceutical available to treat AMD was Pegaptanib Sodium (Macugen, Pfizer, ~50 kDa), a single nucleic acid strand (oligonucleotide aptamer) that only binds to VEGF-A₁₆₅ but not to other types of VEGF-molecules. When VEGF is bound it is no longer able to bind to the VEGF-receptor as the ligand bonding site does not fit anymore. Consequently, VEGF is removed from the signal cascade and the angiogenesis is inhibited. As Pegaptanib only binds a specific type of VEGF, other VEGF-molecules are still able to activate the signal cascade for angiogenesis and thus the efficiency of Pegaptanib is only minor. As a result, Pegaptanib has been replaced by other pharmaceuticals.

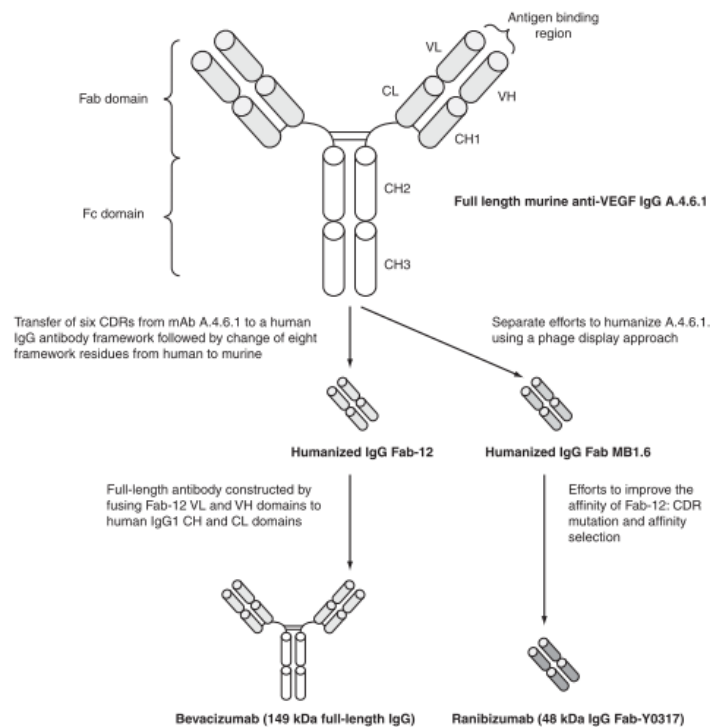


Figure 2.7: Difference between Bevacizumab and Ranibizumab: Bevacizumab (149kDa) is a IgG1 antibody consisting of two Fab-domains and a Fc-domain. The Fc-domain can bind to Fc-receptors. Antigen binding sites are located at the end of the Fab-domain. Ranibizumab only consists of the Fab-domain without a Fc-domain and is therefore significantly smaller (48.4 kDa). From Meyer *et al.* ¹²¹

Currently, three pharmaceuticals for treating AMD are used in therapy: Bevacizumab (Avastin, Novartis, 149 kDa) an 'offlabel' used pharmaceutical originally used in tumor therapy, Ranibizumab (Lucentis, Novartis, 48.4 kDa) the officially approved pharmaceutical for treating AMD, and Aflibercept (Eylea/VEGF-Trap, Bayer, 96.9 kDa). Bevacizumab is a complete IgG1 antibody (AB) consisting of two heavy chains (Fc-region) and two light chains (Fab-region). An antigen binding site (VEGF) is located on the end of each light chain. The Fc-region of the IgG is a target for Fc-receptors located on the surface of cells, which among others can result in an immune-response of the cell. The enzyme Papain cleaves IgG into two Fab-fragments (light chain + antigen binding site) and one Fc-fragment (two heavy chains linked by a disulfide bond). Ranibizumab only consists of such a Fab-fragment, is thus significantly smaller and not able to bind to Fc-receptors. Additionally, Ranibizumab does not carry any glycosylation sites and is therefore no target for sugar receptors located on the surface of cells as well.¹²² However, Ranibizumab is considerably more expensive compared to Bevacizumab. Both pharmaceuticals bind all isoforms of the antigen VEGF-A and thus inhibit the activation of VEGF-receptors and therefore counteract CNV.

Pharmaceutical	Distributor	Molecular Weight	Binding of VEGF	
Pegaptanib (Macugen)	Pfizer	~50 kDa	Aptamer	VEGF-A ₁₆₅
Bevacizumab (Avastin)	Novartis	149 kDa	IgG	all isoforms
Ranibizumab (Lucentis)	Novartis	48.4 kDa	Fab-fragment	all isoforms
Aflibercept (Eylea/VEGF-Trap)	Bayer	96.9 kDa	Fab-fragment + binding site for VEGFR	all isoforms of VEGF-A + VEGF-B

Table 2.2: *VEGF-inhibitors used for AMD-treatment.*

The third relatively new pharmaceutical Aflibercept (Eylea/VEGF-Trap, Bayer, 96.9 kDa) is a recombinant fusion protein consisting of a Fab-fragment of IgG similar to Ranibizumab, but additionally possesses the binding site of the soluble VEGF-receptor (sVEGFR). VEGF Trap also binds to all isoforms of VEGF-A and additionally VEGF-B and thus also inhibits CNV. The binding affinity of Aflibercept is determined to be ten times higher compared to Bevacizumab. Long-term studies are currently not available. A detailed overview including all clinical trials can be found in Lo Giudice *et al.*¹⁰

Current State in Science

The effectiveness of Bevacizumab and Ranibizumab is highly controversial. Until today, a long-term clinical-trial for the use of Bevacizumab in exudative AMD still needs to be

conducted. Therefore, the effects and safety of using Bevacizumab are unknown. The CATT-study is a clinical study, which directly compares the effects of Bevacizumab and Ranibizumab in-vivo.²³ The study was not able to reveal any significant differences between the two pharmaceuticals. Both pharmaceuticals improved the vision of patients to a similar amount. The only differences observed were a more efficient liquid removal by Ranibizumab. The long-term effects of both pharmaceuticals show similar results as well.¹²³

The CATT-study only describes a clinical outcome of both pharmaceuticals but provides no histological information such as penetration of retina and choroid by Bevacizumab and Ranibizumab or the effect of the pharmaceuticals on the RPE. It was assumed that Bevacizumab is less efficient as the IgG1-AB might be too big to cross the retina in order to reach the choroid, where the CNV generally starts.¹²⁴ As a result Ranibizumab, which is only a Fab-fragment of IgG1-AB was created. However, it was demonstrated that despite its size Bevacizumab is able to reach the RPE and can even be detected in the choroid (monkey).¹²⁵ Moreover, Bevacizumab was detected in POS (monkey) after 7 days of injection.¹²⁵ As a consequence Bevacizumab was also detected within RPE-cells as POS are digested by the RPE. After 14 days the pharmaceutical was no longer detectable within the inner retina. Other studies were also able to localize Bevacizumab within the retina within a time range of days or even few hours (rabbits and mice).^{126,127}

Bevacizumab and Ranibizumab have shown that they are able to neutralize VEGF to the same amount in cell-cultures (*in vitro*) with being Ranibizumab already efficient at lower quantities.¹²⁸ There are some concerns about the effect of the pharmaceuticals on the permeability of the RPE. It has been demonstrated that Bevacizumab leads to a higher permeability of the RPE for nine days, whereas the effects of Ranibizumab were only observable for three days.¹²⁹ Prior to this study the half-life time for Ranibizumab (2.88 d) compared to Bevacizumab (4.32 d) within the plasma was already determined.¹³⁰ As the RPE forms an essential barrier between the rest of the retina and choroid this observation could negatively affect diffusion processes. However, more detailed data could not be found.

Two different mechanisms underlying the uptake of the pharmaceuticals were suggested. Bevacizumab was detected in RPE cells due to phagocytosis of POS, which contained Bevacizumab (monkey).¹²⁵ Other studies were able to demonstrate Bevacizumab within cultured cells (pig) in the absence of POS.²² Ranibizumab was not observed within cells. Based on these results the molecular mechanism for the uptake of Bevacizumab into the cell is assumed to be due to a Fc-mediated phagocytosis. Bevacizumab, but not Ranibizumab is carrying a Fc-domain as well as glycosylation sites (sugar). Thus Fc-receptors are able to bind Bevacizumab but not Ranibizumab, which could explain a Bevacizumab uptake into the cell. Additionally an uptake mediated by sugar receptors (mannose and galectins),

which have been reported to be expressed on RPE surfaces, might be an explanation. In the course of these studies, the effectiveness of both pharmaceuticals were investigated as well. Both pharmaceuticals were only effective within three days, where no detectable amount of VEGF could be observed within the liquid excess. Afterwards VEGF-production increased again. When adding Bevacizumab (250 $\mu\text{g}/\text{ml}$) and additionally POS-linked Beads to the RPE-cell-culture, it has been shown that cells were either accumulating lots of Bevacizumab molecules but only a few beads or the other way around. Based on these results it was concluded that the phagocytosis of POS is reduced while Bevacizumab is present. This might indicate possible long-term effects when treating repeatedly with Bevacizumab, which still need to be studied.¹³¹ The same experiment was conducted using Ranibizumab (125 $\mu\text{g}/\text{ml}$), which could not be observed within RPE-cells. The direct comparison between both cell-cultures showed a 50 % reduced phagocytosis of POS for Bevacizumab compared to Ranibizumab.¹³¹

3.1 SIM - Microscope Setup

The following section describes the existing microscope setup at the starting point of this thesis. The microscope was only capable of standard fluorescence imaging and the high-resolution imaging method 'Structured Illumination Microscopy' (SIM). The development of this microscope into a 'Combo'-microscope in order to perform SIM imaging as well as SMLM imaging with the same physical setup is described in section 3.2.

3.1.1 Hardware

The setup provides three different monochromatic laser wavelength for illumination (405 nm: DPSS, 150 mW, BFi Optilas, Dietzenbach, Germany; 488 nm and 568 nm: Coherent Sapphire 488/568 HP, 200 mW, Coherent, Dieburg, Germany). A fourth laser line (633 nm) was available, but not coupled into the beam path. The laser-lines are coupled into the optical path by using appropriate dichromatic mirrors. Laser lines are controlled by custom built shutters as described in detail elsewhere.¹³² Shutters are fully automated, which enabled either sequential or simultaneous switching between the different laser lines. A custom-built neutral-density-filter wheel (fig. 3.1, orange asterix) allows controlling laser intensities as not all laser are adjustable. A detailed description of the wheel including the software control can be found elsewhere.¹³² The wheel contains twelve neutral gray filters of different densities, which cover a range from 100 % to 0 % transmission. An attached stepper motor enables an automated rotation of the neutral-density-filter wheel. Calibration of the wheel is done by a photo sensor consisting of a photo diode and a light emitting diode (OPB980, OPTEK Electronics, Carrollton, Texas, USA).¹

The illumination pattern is generated by a Twyman-Green interferometer as previously

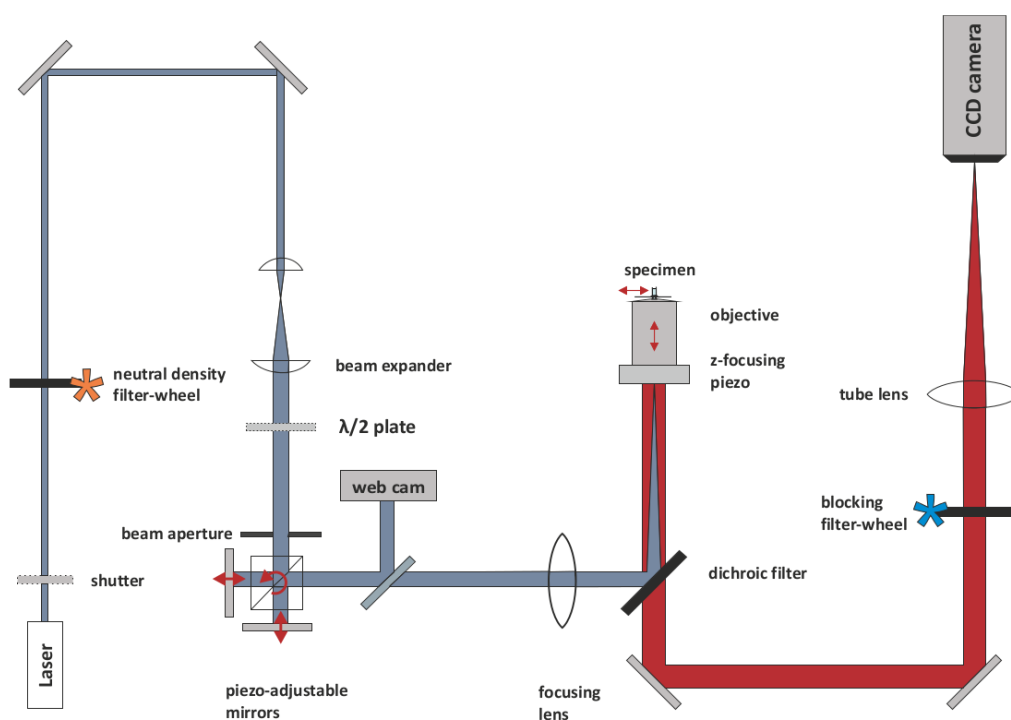


Figure 3.1: Schematic of the 'SIM'-setup: Three laser excitation frequencies are available, which can be selectively switched on and off by using custom built shutters. A neutral density filter-wheel (orange asterisk) regulates the laser-intensity. The expanded beam is passing a Twyman-Green interferometer, where a sinusoidal interference pattern is generated. This illumination pattern is redirected onto the sample by an quad-band dichromatic mirror. A manual emission filter-wheel (blue asterisk) removes all remaining of the excitation laser light within the detection path. The tube lens projects the fluorescence light into its focal plane (primary image plane), where the CCD-chip of the high quantum efficiency camera is placed. Modified from Rossberger *et. al.*¹

described.³² A 50 % beam splitting mirror transmits one half of the beam and reflects the other half each onto a reflective mirror positioned directly next to the cube in order to minimize beam displacement. Both beams are then redirected back into the cube by the mirrors, which are controlled by piezo actuators and appropriate piezo amplifiers (both PI, Karlsruhe, Germany). The interference pattern is generated in the plane of the beam splitting cube, which is mounted on a rotatable stage, including an appropriate linear actuator and its control element (M-RS 65 and CMA-12CCCL, controller: Esp300, all Newport Spectra-Physics GmbH, Darmstadt, Germany). Thus, the cube can be automatically rotated around its axis perpendicular to the optic table. The incident excitation beam is reflected by an angle of Θ instead of 90° . This results in two beams, which leave the cube at an angle of 2Θ and -2Θ respectively (fig. 3.1: rotated red arrow). Each beam is of $1/4$ intensity of the original excitation beam and is passing through the focusing lens. As the splitting cube is in the focal point of the focusing lens, the generated sinusoidal

illumination pattern is imaged into the object plane by the high numerical objective (Leica HCX PL APO 100x/1.4-0.7 OIL CS).¹

The illumination pattern can be shifted by the piezo actuators attached to the mirrors (fig. 3.1: red arrows). A minimum of three different positions of the patterns is required, which results in sequential shifts of the mirror by $\lambda/(2*3)$ (2 due to the doubling of the optical path). In order to achieve an isotropic resolution improvement, a minimum of three orientations of the illumination pattern are generally generated. For this purpose the splitting cube is tilted by a second attached linear actuator (CMA-12CCCL, Newport Spectra-Physics GmbH, Darmstadt, Germany), which results in a rotation of the two beams around a horizontal axis (x- and y-axis). In order to achieve a high modulation of the excitation pattern in SIM, it is important that the polarization of the interfering light beams is perpendicular to the plane spanned by the two beams. Therefore, a half-wave plate mounted on a motorized rotational stage (Newport PR50CC) is used in order to rotate the polarization according to the orientation of the pattern. All optical parts in the beam path after the wave plate are unpolarizing.¹

The fluorescent signal emitted by the sample is separated from the excitation laser light by a quad-band dichromatic filter (Z405/488/568/647, AHF, Tuebingen, Germany). Remainings of the excitation light are blocked by a manual emission filter wheel (fig. 3.1, blue asterix) containing a triple-band bandpass emission filter (Z488/568/647 M V2, AHF, Tuebingen, Germany) among others. The image is formed by the tube lens, which projects the Fraunhofer diffraction pattern given by the fluorescence emission onto a CCD-camera (Sensicam QE, PCO, Kelheim, Germany) in its focal plane.¹ A more detailed description of the microscope setup has been published recently.³²

3.1.2 Software

The hardware control and acquisition software is written in the python programming language. A basic graphical user interface including basic hardware control for the described setup above was developed in the cause of the PhD-thesis by David Baddeley.¹³³ The graphical user interface (GUI) includes basic controls for the CCD-camera and piezo. When performing SIM-imaging phase-shifting and rotation of the grating need to be conducted manually for each acquired image as well as saving of each single image.

3.2 Development of the 'Combo' - Microscope Setup

Based on the study of autofluorescent (AF) particles within drusen several further questions respective molecular level were risen. Though SIM is a very useful tool to study objects beyond the diffraction limit, the resolving power is still limited to about 100 nm. In order to resolve objects on the molecular level other microscopy methods needed to be employed.

Electron-microscopy could be first choice as it provides a very high resolution down to the angstrom-range, but this method is highly challenging in terms of hardware realization. Moreover sample preparation differs for electron microscopy compared to fluorescence microscopy. Similar applies for STED-microscopy⁸⁰ - sample preparation is in this case the same and resolution has been realized down to the nanometer-level, but the setup is very complex to realize. SMLM-methods seemed to be most promising as they provide an appropriate resolving power on the nanometer-scale. The disadvantage of SMLM-methods appear when AF structures are of interest as well or long-term live-cell imaging is aimed. Here SMLM-methods generally fail. The same applies for sparsely labeled structures, where visualization methods generally used in SMLM-imaging fail resulting in a missing assignment of single molecule position information. An orientation within the biological object is then generally no longer possible.

However, when comparing SIM and SMLM it is obvious that each method compensates the weaknesses of the other one, which will be discussed in detail in section 2.1.6. As a result a combination of both methods seemed to be highly desirable in order to increase the amount of information. The challenge remaining is to image the same region of interest within a sample using different microscope setups. Furthermore this procedure is very time consuming and in several cases this might be even impossible. The implementation of two methods in one setup would simplify the imaging process enormously. The aim was to realize a microscope, which is able to provide a high resolved overview image combined with super-resolved single molecule position information of the specimen and furthermore is capable of depicting AF structures ideally also in-vitro.

The following chapter represents the main part of this thesis, which deals with the design and development of a newly 'Combo'-super-resolution setup. A detailed description of all hard- and software developments and changes of the prior existing SIM-setup is given.

3.2.1 Hardware

Hardware development of the microscope setup affected parts of the excitation as well as nearly the whole optical detection path had been rebuilt. Shutter, neutral density filter-wheel and the Twyman-Green interferometer as described in the prior section were not touched by any changes (see section 3.1). Everything else was modified in order to

extend the setup for sequential SIM and SMLM imaging (fig. 3.2). The result is a custom built wide-field microscope of extraordinary mechanical stability, which combines the two high resolution microscopy methods Structured Illumination Microscopy (SIM) and Single Molecule Localization Microscopy (SMLM).

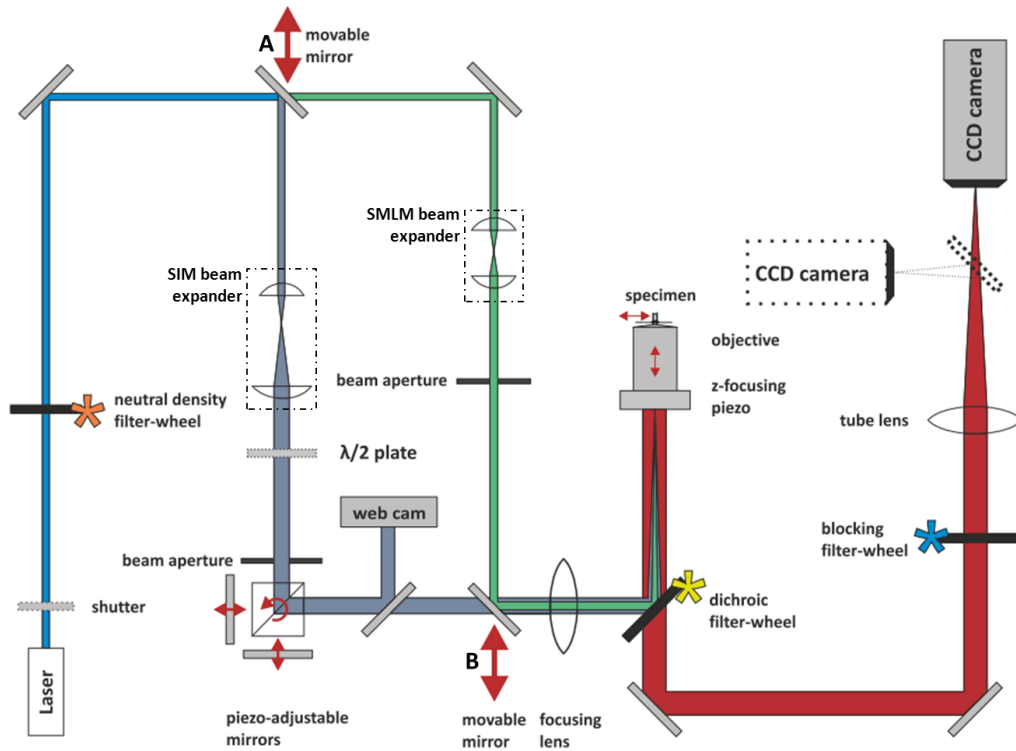


Figure 3.2: Schematic of the 'Combo'-setup: Five laser excitation frequencies are available for the presented 'Combo'-setup, which can be selectively switched on and off by using custom built shutters. A neutral density filter-wheel (orange asterisk) regulates the laser-intensity. An automated mirror-system switches the setup between two modes depending on whether the mirrors are moved in or out of the beam-path. In the case of the mirror A being placed into the beam-path the laser-beam is reflected into the direction of the custom built interferometer in order to perform SIM imaging (dark blue). For this purpose the second automated mirror B needs to be removed from the excitation-path. In reverse mode, SMLM imaging (green) is performed. A fully automated dichromatic splitter filter-wheel (yellow asterisk) as well as an automated blocking filter-wheel (blue asterisk) were introduced. The tube lens projects the fluorescence light into its focal plane (primary image plane), where the CCD-chip of the high quantum efficiency camera is placed. The setup can be supplemented with a second CCD-camera in order to split fluorescence light emitted by different fluorophores, but excited with the same wavelength. In addition to the SPDMPhymod/SIM mode used in this work, the setup is also applicable for PALM/FPALM or STORM/dSTORM imaging. From Rossberger et al.¹

In addition to the SIM optical path a second SMLM path was established by implementing a motorized mirror-based mechanism into the beam path, which allows circumventing the beam expander matching the requirements for SIM-imaging, the $\lambda/2$ plate and the Twyman Green interferometer (fig. 3.2, large arrows). The hardware realization of the switchable mirrors was conducted of Frederick Goerlitz in the course of his Bachelor the-

sis ('Improvement of a setup for 5 colors SW-TIRF-Microscopy'). Both pathways merge again behind the second motorized mirror placed in front of the focusing lens. As SMLM is generally relying on high illumination intensities a different beam expander needed to be implemented into the SMLM path (fig. 3.2; tab. 3.1), resulting in a smaller illumination field compared to the SIM-mode.

Lenses	SMLM beam path	SIM beam path
f_1	10 mm	40 mm
f_2	250 mm	100 mm

Table 3.1: *Lenses Beam Expander*

While the first movable mirror A is placed within the optical path and the second movable mirror B is removed, SIM-imaging is enabled as the light travels through the Tywman Green interferometer and the corresponding beam expander (fig. 3.2). In the case of SMLM-imaging mirror A is removed from the optical path whereas the second mirror B is switched into the path in order to deflect the excitation beam into the direction of the focusing lens. In order to realize fast switching between the two microscope modes SIM and SMLM both mirrors are triggered simultaneously via a micro-controller. (Arduino Uno, for details see section 3.2.2). The rest of the beam path is the same for both microscope modes. As SMLM usually requires high illumination intensities a different beam expansion compared to SIM is implemented into the optical path by using lenses of different focuses (tab. 3.1).

Five different monochromatic laser wavelengths from the UV-range to the IR-range are currently available for illumination (tab. 3.2). Shutters and neutral-density-filter wheel (fig. 3.2, orange asterisk) have been described in the previous section (see section 3.1.1). The focusing lens, an achromat (VIS ARB2, $d = 31.5$, $f = 300$) was mounted on a x-z-translation system (both QiOptiq Photonics, Goettingen, Germany) for easier adjustments. The lens focuses the laser light into the high numerical objective (HCX PL APO 100x/1.4 oil CS, Leica, Wetzlar, Germany). The objective lens then refocuses the generated sinusoidal illumination pattern into a plane of the sample. The objective lens is mounted on a fine adjustment micrometer (G061061000, Qioptiq Photonics, Goettingen, Germany), which allows a coarse adjustment of the focus into the sample. In order to scan the sample in the z-direction/for fine adjustment of the focus position, a further focusing element (P-725.1CD, $100 \mu\text{m}$, pfoc, Physik Instrumente (PI), Karlsruhe, Germany)

Wavelength [nm]	Power [mW]	Type	Model	Manufacturer
405	150	DPSS	n/a	BFi Optilas, Dietzenbach, Germany
488	200	DPSS	Coherent Sapphire 568 HP	Coherent, Dieburg, Germany
568	200	DPSS	Coherent Sapphire 568 HP	Coherent, Dieburg, Germany
671	300	DPSS	VA- I-300-671	Beijing Viasho Technology Co.Ltd., Beijing, PRC
808	800	Diode	Coherent Sapphire 568 HP	Roithner Lasertechnik, Vienna, Austria

Table 3.2: List of laser available at the 'Combo'-setup.

is introduced.

To obtain a visual control of the grating generated and projected into the object plane, a small part of the beams is split and redirected by an additional beam splitter cube within the optical path onto the CCD-chip of a web-camera (MANHATTAN Webcam 500) before passing through the focusing lens. This visual control is necessary for the adjustment of the interferometer, which can be controlled by several piezo-actuators as described above. The rest of the excitation light is reflected on appropriate dichromatic edge-filters (tab. 3.3) mounted on a commercially available manual dichromatic filter-wheel (CDFW5/M, Thorlabs, Munich, Germany, fig. 3.2, yellow asterisk). In order to enable a fully automated image acquisition, the manual dichromatic filter wheel was mounted on a custom built construction including a shaft, which was attached to a stepper motor (P430 258 005 01, Portescap, La Chaux-de-Fonds, Switzerland) removed from an old ophthalmic imaging unit. An simple stepper motor controller (RN-Stepp297, Robotikhardware, Sontra, Germany) allows an automated operation of the stepper motor utilizing custom software, which was developed in the course of this work (details see section 3.2.2).

The reflected excitation light illuminates the aperture of the objective lens and is focused into the sample. Microscope slides or a live-cell chamber are mounted on a Nikon Eclipse microscope table (for Nikon Eclipse TI and TE 2000, 00-24-437-0000, Maerzhaeuser, Wetzlar, Germany). The microscope table itself is mounted on a custom-built stage made of invar, which was constructed using the CAD software SolidWorks® 2012 Student Edition. Invar is a special iron(65%)-nickel(35%) alloy (Fe65Ni35-Invar), which benefits from its

Dichromatic Filters		
Wavelength [nm]	Model	Manufacturer
405	Di02-R405	Semrock, Rochester, NY
488	Di02-R488	Semrock, Rochester, NY
568	Di02-R568	Semrock, Rochester, NY
680	Q680LP	Semrock, Rochester, NY
810	Q810LP	Chroma, Olching, Germany

Emission Filters		
Wavelength [nm]	Model	Manufacturer
405	BLP01-405	Semrock, Rochester, NY
488	BLP01-488	Semrock, Rochester, NY
561	BLP01-561	Semrock, Rochester, NY
690	LP XF 3104	Omega Optical, Olching, Germany
808	BLP01-808	Semrock, Rochester, NY

Table 3.3: *List of dichromatic and emission filter available at the 'Combo'-setup.*

unusually low coefficient of expansion (20-90°C: $1.7 - 2.0 \cdot 10^{-6} \text{ K}^{-1}$ and thus minimizes thermal and mechanical drifts. The controlling of the microscope table is performed by a commercial controller (mc2000, also Maerzhaeuser) which is additionally equipped with a joystick.

For easier adjustments, a periscope (not shown in fig. 3.2, silver mirrors, 21010, Chroma, Olching, Germany) custom built of commercially available optic components is positioned in front of the dichromatic filter-wheel. This is used to direct the laser beam into the objective and to perform imaging at different illumination angles. Thus, TIRF (Total Internal Reflection Fluorescence)-microscopy can be conducted as well.

The fluorescence signal emitted by the sample passes the high numerical objective lens and is transmitted by the same appropriate dichromatic edge-filter, which separates the excitation light from the fluorescent emission light (fig. 3.2, yellow asterisk). To remove any remains of the excitation light, a stepper motor driven filter wheel (FW102C, Thorlabs,

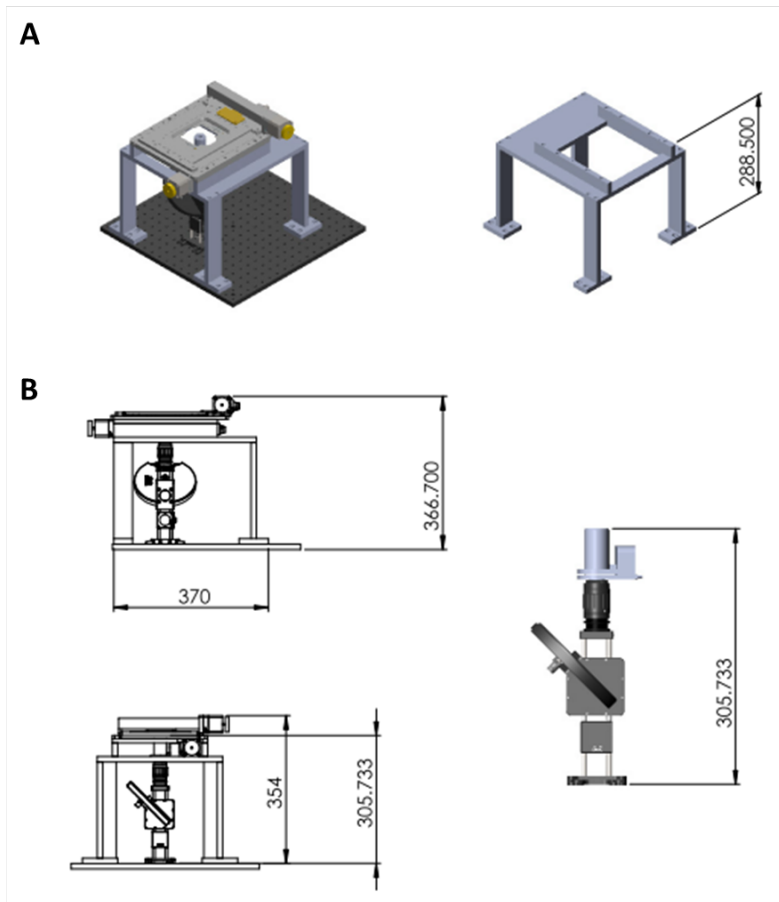


Figure 3.3: Microscope stage made of Invar. Constructions were performed with SolidWorks®2012 Student Edition. The stage was constructed meeting the requirements of the newly purchased components for the 'Combo'-setup, which include dichromatic filterwheel (Thorlabs), a manual fine adjustment micrometer (Qioptiq Photonics), a software-controlled fine adjustment unit (PI) and the objective (Leica) among others. **A:** shows the whole assembly including the new microscope table (Maerzhaeuser) mounted on top of the constructed invar (Fe65Ni35-Invar) stage. **B:** Sideview. Dimensions are in mm.

Munich, Germany, fig. 3.2, blue asterisk) is placed in front of the tube lens prior to a high quantum efficiency CCD-camera (Sensicam QE, PCO, Kelheim, Germany). This filter wheel houses up to 6 emission filters - one for each excitation wavelength (tab. 3.2) - and is fully automated. The diameter of the illuminated field of view is $\sim 65 \mu\text{m}$, which corresponds to a full use of the CCD-chip of the camera. The setup can be further extended by implementing a second dichromatic beam-splitter and a second CCD-camera. Thus the light emitted by different fluorophores excited with the same (or different) wavelengths can be split on two CCD-chips similar to the setup described by Baddeley *et al.*³⁹ As a consequence the range of fluorophores can be further extended.

Additional equipment for the microscope includes a halogen lamp (TQ/FOI-1, 150W, Techni-Quip, Pleasanton, California, USA) for studying samples using transmitted light and for widefield fluorescence microscopy. Furthermore, a heated incubator (UNO Top Stage Incubator, H501, Okolab, Ottaviano, Italy) has been purchased in order to perform live-cell experiments. An exchangeable 35 mm Petri-dish plate adapter (H501-EC-35PA, Okolab, Ottaviano, Italy) is implemented into the incubator. CO₂ and humidity control

during experiments is ensured by an additional air pump (OKO-AP, Okolab, Ottaviano, Italy).

In the course of this work the SMLM method SPDMP_{hymod}^{38,40,57,58} was conducted. However, other SMLM variations mentioned before may also be applied with the described setup. A detailed description of the image reconstruction process for SIM and SMLM imaging is given in section 2.1.4.

3.2.2 Electronics

All main hardware components of the 'Combo'-setup are fully automated and software-controlled. Switching between SMLM- and SIM-mode of the microscope is performed by an automated mirror system, which can be either placed within the beam-path or removed. Mirrors are triggered via a microcontroller (Arduino Uno, fig. 3.4 left). The communication with the Arduino microcontroller is carried out via USB-connection, which also guarantees the power supply. Basic software development for the communication with the Arduino was done by Gerrit Best (KIP, University of Heidelberg) in the course of a different project using the open-source Arduino environment (C++) provided on the Arduino-website. The basic software was extended in the course of this work in order to allow software controlled simultaneous switching of both mirrors in C++ (tab. 3.4; pin 8).

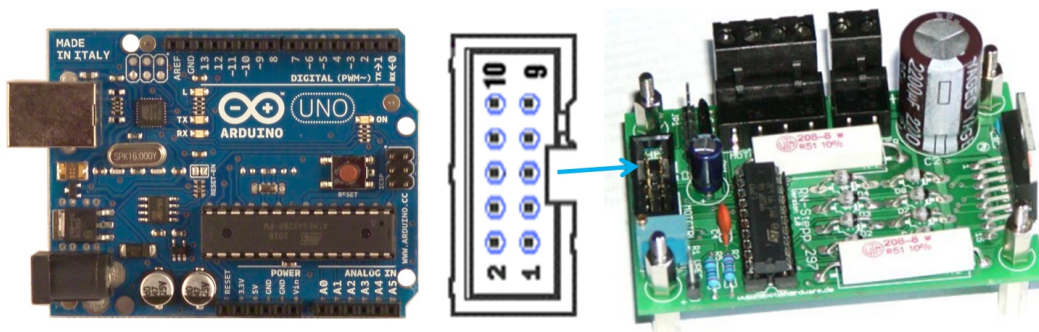


Figure 3.4: **Left:** Arduino Uno microcontroller **Right:** Stepper motor controller

The manual dichromatic filterwheel was automated by a custom built construction including an attached stepper motor (P430 258 005 01, Portescap; fig. 3.5 right). The stepper motor control element (RN-Stepp297, Robotikhardware; fig. 3.4) communication is conducted via the Arduino microcontroller likewise. A wiring diagram is shown in figure 3.5 in the left image. The motor consists of four coils, which can be either operated in series or parallel. As the stepper motor controller is configured for a bipolar control of the motor

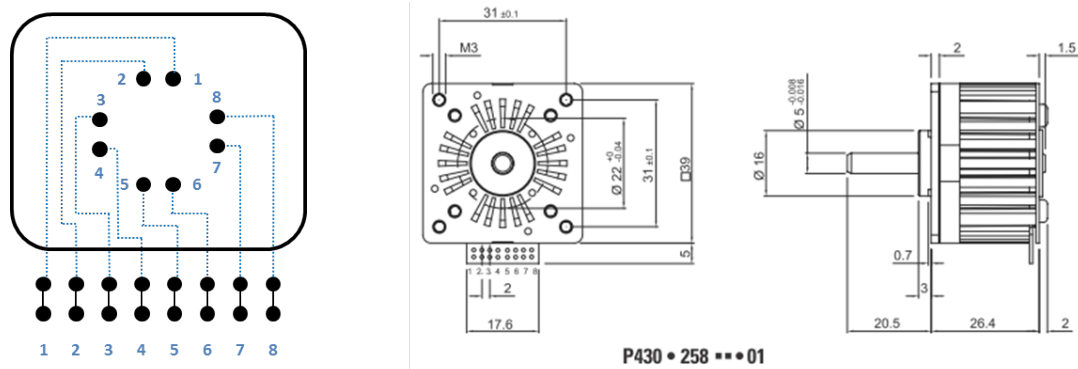


Figure 3.5: **Left:** Wiring diagram of the stepper motor P430 258 005 01 (Portescap). The motor consists of 4 coils, which can be connected either in series or parallel. In the described microscope setup the two opposite coils were connected in series. **Right:** Stepper motor specification from www.portescap.de

two coils opposite of each other have to be connected. For the described 'Combo'-setup, the two coils opposite of each other were connected in series in order to exploit the by a factor $\sqrt{2}$ higher torque (<http://www.rn-wissen.de/index.php/Schrittmotoren>) compared to a parallel connection (fig. 3.6, red/black and yellow/brown wires). The resistance of the serial connection is twice the single resistance for one coil. However, the maximal current possible is automatically reduced by the same factor.

The connection with the controller was conducted via a pc-mouse cable (fig. 3.6: Stepper motor connection). The stepper motor controller power supply is provided by the Arduino microcontroller (Pin 1 and 2 of stepper motor controller). The motor power is guaranteed via the controller by a 24 V (DC) power supply. Though the rated voltage of the motor is specified with 12 V, a 24 V power supply was chosen in order to deal with the internal current regulation of the controller.

Pin 3 to 5 (JP1 fig. 3.6) of the stepper motor controller are assigned as displayed in table 3.4. A pull-up at each pin is existing. Pins are triggered via the Arduino microcontroller. Via pin 3 (arduino pin 2) the motor is only switched on during rotation of the dichromatic filter-wheel. It is necessary to switch the motor off as currents higher than the specified rated current of 0.56 A are flowing through the motor. Due to experimental results where the motor was not able to rotate the inertial mass of the filter-wheel, the adjustable reference voltage V_{ref} measurable on the controller plate was increased. Thus the maximal motor current is increased ($V_{ref} = I_{motor} \cdot 0.51 \Omega$) as well, which directly translates into a higher torque.

The motor can be rotated either in a full- (100 x 3.6°) or half-step (200 x 1.8°) mode. To operate the motor in a full-step mode pin 5 (MOTCTRL fig. 3.6) is shorted with pin 2 (GND) in order to convert the existing pull-up (half-step mode) into a pull-down (full-step mode). The trigger to rotate the motor by one step is triggered via pin 5 (Arduino pin

7). As the filter-wheel contains five different dichromatic beamsplitters a change from one filter to the next is conducted by 20 single steps of the motor assuming a full-step mode. In order to operate the filter-wheel most time-efficient the smallest angle, which needs to be covered for the rotation, is calculated before rotating the filter-wheel either clockwise (CW) or counter-clockwise (CCW). The direction of the rotation is triggered via pin 4 (Arduino pin 4).

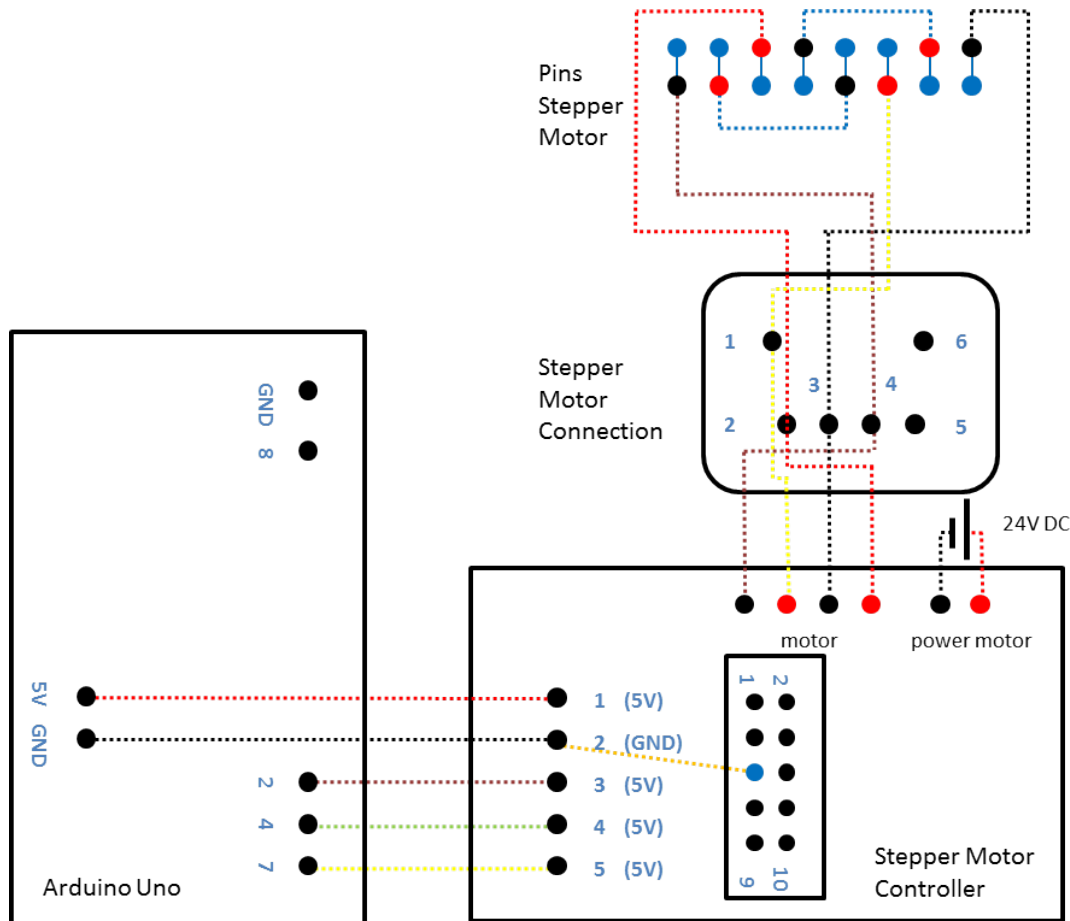


Figure 3.6: *Wiring diagram: Switching between SMLM- and SIM-mode is performed via the Arduino Uno microcontroller (pin 8). Likewise the communication with the stepper motor controller is conducted. The stepper motor controller is connected to the stepper motor via an old pc-mouse cable. The stepper motor is controlled bipolar - the two opposite coils are connected in series in order to achieve a torque increased by a factor of $\sqrt{2}$ compared to a parallel connection. The motor is supplied by 24 V via the stepper controller. The power supply of the stepper controller is realized by 5 V provided by the Arduino microcontroller. Switch on/off of the motor (pin 3, arduino: pin 2), rotation direction (pin 4) and clock (one step of motor, pin 5, arduino: pin 7) are triggered via the Arduino microcontroller as well. Full-step mode is realized by shorting pin 5 (MOTCTRL). More details can be found within the text.*

In order to trigger all features described in this section via the microscope GUI a serial connection for the communication with the Arduino microcontroller was implemented into the python code of the microscope software (see section 3.2.3).

Pin Arduino Microcontroller	Pin Stepper Motor Controller	Color	Function
8/GND	-	purple/off-white	switch mirrors (SIM/SMLM-mode)
5V/GND	1/2	orange/white	power supply stepper motor controller
2	3	brown	clock stepper (rotates stepper motor)
4	4	green	rotation direction (CW/CCW)
7	5	yellow	enable stepper motor (On/Off)

Table 3.4: *Pin assignment: Arduino Uno microcontroller and stepper motor controller*

3.2.3 Software

The acquisition software is based on the programming language python. The basic microscope software 'PYME' for SMLM is available at <http://code.google.com/p/python-microscopy/>. The basic software mainly written in Python was modified and extended in order to fulfill the requirements of the described 'Combo'-setup. The aim was a user-friendly, self-explanatory graphical user interface (GUI) and a fully automated and thus time-saving image acquisition of both microscope modes. Figure 3.7 shows the GUI modified and developed during this work.

On the left side all hardware controls (A: red and purple frame) are displayed. All piezo controls (A: yellow frame) for the interferometer such as rotation and tilting of the beam splitter (spatial orientation of grating) and the piezo control for the mirrors (phase shift) can be manually adjusted with an accuracy of three digits. The piezo control for the z-focusing unit is included as well. A manual shutter control (A: green frame) for the different excitation laser lines allows simultaneous as well as sequential switching of the laser lines depending on filters and application. All filter wheel controls are also shown on the left side of the GUI (A: purple frame). The density filter wheel includes 12 different filters or varying transmittance. The dichromatic filter wheel provides five different long-pass beam splitters for each of the different excitation laser lines. An appropriate emission filter can be chosen with last filter control, which includes six different long-pass emission filters. Further controls include a joystick control and a switching option, which allows fast changing between the two microscope modes (A: both cyan frame). The chosen camera mode, integration time and an automatic gray value adjustment are displayed among other camera controls (A: orange frame). In the middle of the GUI either the current CCD-camera view is displayed (A: blue frame) or the grating projected on the webcam

(B: blue frame) by choosing a different slider. In addition to the grating in the position space (B: left within blue frame), the corresponding Fourier transform of the grating is also displayed (B: right within blue frame).

A fully automated acquisition algorithm is provided for SIM (B: orange frame) and SMLM imaging (B: yellow frame). An acquisition script for SMLM was already included in the basic 'PYME' version, which allows 2D or 3D imaging. A fully automated analyzing procedure for SMLM-data was already implemented as well. An algorithm for SIM imaging was implemented in the course of this work. Parameters necessary for SIM imaging may be assigned only once prior to all imaging processes and are then reused for all further acquisition processes. This procedure saves a lot of time compared to the manual adjustments, which had to be conducted with the old software prior to each image acquisition. Pre-defined parameters include laser power, grating period, piezo-settings for different polarization and grating positions (orientation), integration time for images and density filter wheel settings (B: purple frame). Phase positions are automatically calculated depending on the wavelength of the illumination laser (B: pink frame). 2D or 3D imaging as well as total number of orientations of the grating can be defined including 3D-parameters such as step-size, start- and end-position. However, all parameters can be adapted during different acquisitions if necessary. The image acquisition is carried out sequentially. Changing of phases, grating orientations and illumination lasers as well as 3D stepping do not need manual manipulation. Thus a series of images, which include the pre-defined total number of different phases and orientations of the grating for a chosen number of excitation laser lines are recorded. 3D stepping is also performed software controlled by automatically changing the z-positioning via a z-focusing piezo-unit as mentioned. Saving is still done manually though an automated saving procedure is under development. Formats for saving can be either 'tif' or 'h5' formats. As the reconstruction software for SIM-data is written in Matlab, an import routine for both formats into Matlab is available in the research group. A metadata saving routine is already included within the 'PYME'-package. This routine was extended for SIM-acquisition and completed for various parameters specific for the 'Combo'-setup.

The microscope stage positions for each acquisition are automatically saved (B: cyan frame), which allows repeated relocation and imaging of the same region of interest (ROI, max. $88.75 \mu\text{m} \times 67.08 \mu\text{m}$), which is generally necessary for time-resolved live-cell experiments. However, it is only possible to save relative stage positions. In the case of a power blackout positions might be not accessible again as no absolute positions are currently available. A further development would include a calibration of the microscope table.

Microscope modes were changed by movable mirrors as described in previous section. Mirrors were triggered by a micro-controller (Arduino Uno). Software development for the communication with the micro-controller was done in C++. The same applies for the

controller of the dichromatic filter-wheel. As described in the previous section calibration of the density filter-wheel was performed via a diode. The mirror switching mechanism as well as the dichromatic filter-wheel are not equipped with a diode. Calibration is conducted via external saving of the current position, which has proven to be sufficient even in the case of a software crash or power blackout.

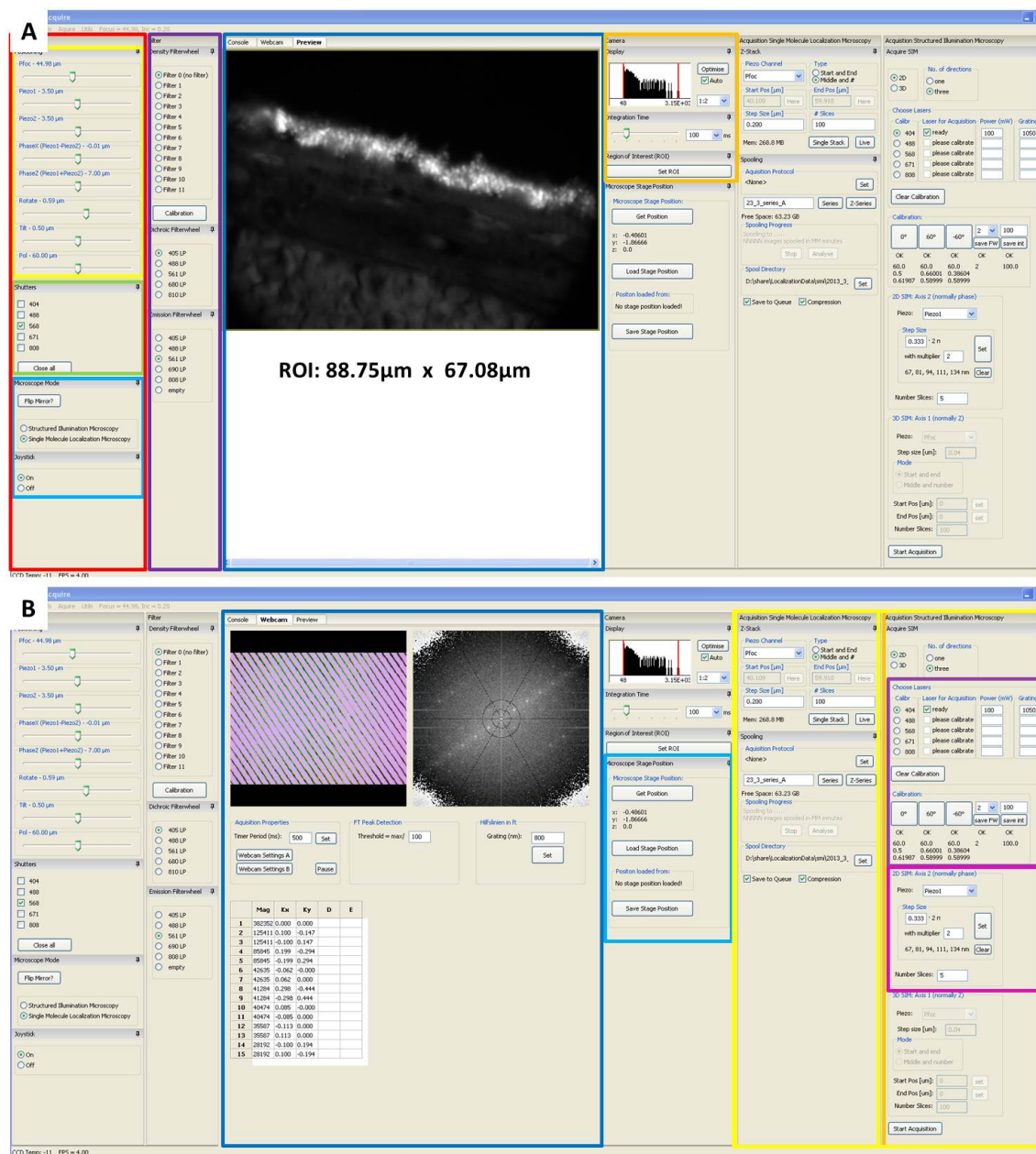


Figure 3.7: Custom designed software interface (GUI) based on in the python microscopy software environment PYME (<http://code.google.com/p/python-microscopy/>). All hardware control elements are displayed on the left side (A: red and purple frame) including piezo-controls (A: yellow frame), shutter control (A: green frame), microscope and joystick controls (A: cyan frame). Moreover, various different filter wheel settings (density, dichromatic and emission filter) can be manually adjusted (A: purple frame). The middle parts of the GUI shows either the current view acquired by the CCD-chip of the camera (A: blue frame) or the webcam view (B: blue frame), where the grating in spatial and Fourier space is monitored. Camera control elements are displayed within the orange frame. Microscope stage positions can be saved as well as the relocation of prior saved positions can be conducted (B: cyan frame). The right side displays all parameters necessary for a fully automated image acquisition (B: yellow frame: SIM; orange frame: SMLM; right column: SIM). For further details see text. Modified from Rossberger *et al.*¹.

3.3 Sample Preparation

3.3.1 Section preparation retina

Histological sections from ora serrata to ora serrata transversing the macular region were obtained from eight human donor eyes (76 ± 4 years) from the Department of Ophthalmology, University of Heidelberg. In all donor eyes, no macroscopic retinal abnormalities were detectable except for drusen. There were no signs of advanced dry or exudative AMD. Immediately after removing the anterior segment of the eyes for corneal transplantation, the remaining tissue was fixed with 4% paraformaldehyde (PFA) in phosphate-buffered saline (PBS, pH 7.4) and embedded in paraffin. Sections ($4 \mu\text{m}$) were prepared and fixed on microscope slides, deparaffinized with xylene (3 x 5 min), rehydrated through graded ethanol and stored in phosphate buffered saline until further processing. Approval was obtained from the local ethics committee.

All procedures adhered to the Tenets of the Declaration of Helsinki.² Preparation of sections were conducted by Dr. Thomas Ach (Ophthalmology, University Hospital Heidelberg).

3.3.2 Tissue preparation retina

Retina tissue was obtained from adult mice or rats and fixed for 5 min with 4% paraformaldehyde (PFA, in 0.1 M phosphate buffer (PBS), pH7.4). Afterwards, tissue was washed twice with 1x PBS. Blocking was conducted over night at 4° C (blocking solution: 1x PBS, 0.5% triton-X, 0.2% BSA (bovine serum albumin), 0.02% sodium azide). Tissue was incubated again over night at 4° C in primary antibody (AB) (AB solution: 1x PBS, 1% triton-X, 10% FCS (fetal calf serum), 0.02% sodium azide). Afterwards, tissue was washed three times in 1x PBS for 10 min. Incubation of tissue in the secondary AB was performed for 2 hours at roomtemperature followed by three washing steps for 10 min with 1x PBS. Then retina tissue was fixed with 1% PFA for 5 min. Washing was conducted for 5 min with 1x PBS. Finally, tissue is mounted on slides, embedded in ProlongGold (Life Technologies, Karlsbad, CA) or a modified switching buffer (90% glycerol, 10% 500 mM switching buffer),^{43,51} cover-slipped, and sealed with nailpolish.

Labeling of the axon-initial segment (AIS) of retinal ganglion cells was conducted using primary AB against ankyrin-G (rbAnkG, 1:500, Clone N106/36, Neuromab, Davis, CA) or β -IV-spectrin (rb β -IV-spectrin, 1:500, kind gift from Christian Schultz, Inst. of Neuroanatomy, CBTM, Medical Faculty Mannheim, Heidelberg University). Labeling of the cisternal organelle (CO) was conducted via an AB against synaptopodin (1:500, rbSynpo, 163002 and gpSynpo, 163004, both Synaptic Systems, Goettingen, Germany). Secondary ABs goat anti mouse, rabbit and guinea pig Alexa 488/568/647 (1:1000; Live Technolo-

gies, Carlsbad, CA).

Approval for all animal studies was obtained from Heidelberg University, Medical Faculty Mannheim Animal Research Board and from the State of Baden-Württemberg, Germany and were conducted in accordance with Heidelberg University Guidelines on the Care of Laboratory animals. All retina tissue preparation was conducted by Annabelle Schlueter (Inst. of Neuroanatomy, CBTM, Medical Faculty Mannheim, Heidelberg University).

3.3.3 RPE-cell culture

Human donor cells

Human donor eyes were prepared within 24 h after death. All within the bulb including the retina except the RPE were removed with fine forceps. The remaining bulb is filled with PBS and the RPE is removed with fine forceps and is cut into pieces. Each RPE-piece is incubated in 2 ml enzyme solution trypsin (0.25 % trypsin-EDTA, 25300-062, Life Technologies, Carlsbad, CA) for 40 min at 37°C and 5 % CO₂ in order to dissolve cells. Afterwards 4 ml cell medium (DMEM-F12) is added in order to prevent excessive digestion of the tissue. In the following step the cell-enzyme-solution is centrifuged for 8 min at 1500 r/min and 25°C. The liquid supernatant is discarded preserving the cell pellet. Finally, cells are cultured in 25 cm³ culture bottles (tissue culture flask, 50 ml, 353108, Astromedtec, Bergheim, Austria) embedded in 5 ml incubation medium containing 44.17 % DMEM-F12 (Delbecco's Modified Eagle's Medium; Ham's Nutrient Mixture F-12, 1:1, 30-2006, ATCC, Manassas, VA), 44.17 % Medium199 (31150, Life Technologies, Carlsbad, CA), 8.83 % FCS (fetal bovine serum, ATCC, 30-2020, ATCC, Manassas, VA), 1.77 % penicillin-streptomycin-glutamin (30-2220, 10,000 I.U./ml penicillin, 10,000 ug/ml streptomycin, 200 mM L-glutamine (29.2 mg/ml), ATCC, Manassas, VA), 0.88 % sodium pyruvate (S8636-100ml, Sigma-Aldrich, St. Louis, MO), 0.18 % insulin (1 mg/ml) and incubated at 37°C (5 % CO₂). Incubation medium is changed two times each week until after about 2 to 3 weeks cells have covered the whole bottle bottom. Then cultured cells are dissolved again with trypsin (see above) for 60 min at 37°C (5 % CO₂) and afterwards splitted on several new culture bottles. Each bottle then contains about 3 x 10⁵ cells per 25 cm³, which were counted prior to the splitting by a Neubauer counting chamber.

For imaging cells are cultured within special culture dishes (FluoroDish, 35 mm, FD35-100, World Precision Instruments, Sarasota, FL). 2 ml incubation medium (see above) were added per dish. Additional HEPES buffer was not necessary as DMEM-F12 already contains 15 % HEPES buffer. After incubation over night cells were adherened to the dish bottom, but not densely packed in order to be able of imaging single cells.

Approval was obtained from the local ethics committee. All procedures adhered to the Tenets of the Declaration of Helsinki. Preparation of cells were conducted by Stefanie

Pollithy and Nil Celik (Ophthalmology, University Hospital Heidelberg).

ARPE-19 standard cell line

A standardized cell line (ARPE-19, CRL-2302, ATCC, Manassas, VA) was used for all phagocytosis experiments as this cell line does not contain any AF LF- and MLF-granules, which could potentially interfere with the fluorescent signal of added components thus as pharmaceuticals. Moreover this cell line is generally used as a reference in order to enable a better comparison of different studies. Cells were cultured in in 25 cm³ culture bottles (tissue culture flask, 50 ml, 353108, Astromedtec, Bergheim, Austria) embedded in 5 ml incubation medium containing 89.29 % DMEM-F12 (Delbecco's Modified Eagle's Medium; Ham's Nutrient Mixture F-12, 1:1, 30-2006, ATCC, Manassas, VA), 9.81 % FCS (fetal bovine serum, ATCC, 30-2020, ATCC, Manassas, VA), 0.09 % penicillin-streptomycin-glutamin (30-2220, 10,000 I.U/ml penicillin, 10,000 ug/ml streptomycin, 200 mM L-glutamine (29.2 mg/ml), ATCC, Manassas, VA) and incubated at 37°C. Incubation medium is changed two times each week until after about 2 to 3 weeks cells have covered the whole bottle bottom. Then cultured cells are dissolved with 2 ml enzyme solution trypsin (0.25 % trypsin-EDTA, 25300-062, Life Technologies, Karlsbad, CA) for 15 min at 37°C (5 % CO₂) in order to dissolve cells. The cell-enzyme-solution is split on several new culture bottles. For imaging cells are cultured within special imaging culture dishes (FluoroDish, 35 mm, FD35-100, World Precision Instruments, Sarasota, FL) incubated with 2 ml of incubation medium (see above).

After cells are incubated over night in a culture dish, nucleus and membrane of the cells are labeled with a live-cell labeling kit (CellLight Nucleus-GFP/Membrane-RFP, BacMam 2.0, C10602/C10608, Live Technologies, Karlsbad, CA). Total cell numbers were estimated prior to the incubation procedure in the culture dishes using the Neubauer counting chamber. After one day cells were assumed to undergo only one division cycle, which is considered with a factor of two. The volume added to the culture dish was calculated according to the distributor's specification as follows:

$$V [ml] = \frac{\# cells * desired PPC}{10^8 CellLight [particles/ml]} \quad (3.1)$$

with PPC: total number of particles per cell. After ~ 20 h cells have undergone the next division cycle during which the fluorescent label is expressed. Details are given on the data sheet provided by Live Technologies.

Preparation of cells were conducted by Stefanie Pollithy and Nil Celik (Ophthalmology, University Hospital Heidelberg).

3.4 Imaging and Analysis

3.4.1 Retinal histological sections

One histological section of each donor was analyzed regarding drusen, using a standard wide-field epi-fluorescent microscope (Leica DMRB, Wetzlar, Germany; excitation: 404 nm, camera: Qimcam SVGA-color, Phase, Lübeck, Germany, objective: HCX PL APO 63x/1.4 - 0.6 OIL CS) in order to gain an overview as demonstrated in figure (fig. 3.8). Each druse with or without AF inclusions was imaged. Afterwards same sections were studied with the SIM-setup as described in section 3.1. Each druse was scanned for AF particles from the surface to the bottom (in depth, parallel to Bruch's membrane; z-direction) using low laser intensities in order to avoid bleaching. The focal layer with the largest diameter of the fluorescent particle was chosen by eye. Laser power was then switched to higher intensities to perform SIM-image acquisition (excitation intensity: $87 \text{ mW/cm}^2 \pm 6\%$; 50 msec/image). Two excitation wavelengths were applied consecutively. At first the laser with the longer wavelength (568 nm) was utilized for image acquisition in order to avoid bleaching of the shorter channel. Immediately afterwards the same druse was imaged with the shorter wavelengths (488 nm).²

Illumination of sections was conducted with a fine sinusoidal pattern (350 nm period) at three different phase positions, which add up to a homogeneous illuminated image comparable to an widefield image generally obtained from standard fluorescence microscopy (fig. 3.9).² Isotropic resolution in the lateral plane was achieved by automated rotation of the illumination grating to three different orientations (0° , 60° and 120°). Thus a total of nine images of standard resolution were acquired (3 in each direction). Raw SIM-images were reconstructed by using custom reconstruction software, which has been published in detail elsewhere.^{29,32,52} Further image processing was performed using Matlab and the open source software ImageJ.

Drusen were classified into hard and soft type based on their shape but not content as sections have been treated with organic solvents during the deparaffinisation process.¹⁸ Basal diameters were measured using the image processing software ImageJ, (Open Source, National Institute of Health, US). The number of drusen containing fluorescent material detected by epifluorescence microscopy and SIM was compared.

SIM images were used for further analysis: fluorescent particles within drusen were measured (greatest diameter) and classified into smaller ($< 500 \text{ nm}$ in diameter) and larger ones ($> 500 \text{ nm}$ in diameter). Their distance to Bruch's membrane was determined. Fluorescent material located in drusen was analyzed regarding spectral similarities to intracellular RPE granules overlying the drusen. For this purpose two intensity profiles of selected AF particles and RPE-LF granules were generated (one for each excitation wavelength). Calculating the characteristic ratio of the maxima given by the intensity profiles allows a

comparison of RPE-LF and AF particles within drusen. All statistics were performed with excel. Results are presented as mean value with corresponding standard deviation.²

3.4.2 Retinal tissue

Tissue was scanned for AIS labeling (AnkG/ β -IV-spectrin: Alexa 568) of retinal ganglion cells, which also showed a strong labeling for the CO (Synpo: Alexa 647) in the other color channel, using low laser intensities. A widefield image in transmitted mode was recorded prior to the imaging process (pixelsize: 64.5 nm). Furthermore, a conventional fluorescence widefield image for each color channel was recorded (pixelsize: 64.5 nm). For SIM-acquisition, a fine sinusoidal grating (350 nm period) was projected onto the object plane and then shifted by $1/3 \times 350$ nm along the direction of modulation (three phase positions). Afterwards, the orientation of the grating was changed in order to achieve an isotropic resolution improvement (0° , 60° and -60° ; three orientations). A 3D SIM-stack (z-direction) was recorded sequentially for each color channel (200 nm steps; integration time: 50 msec/image; focal plane intensity: $\sim 46.8 \pm 2.7$ W/cm⁻²). Afterwards, the illumination path was switched to SMLM-mode without moving the specimen. The focal layer corresponding to the middle layer of the SIM-stack was selected for SMLM-imaging. A 2D-SMLM-data set was recorded for each color channel until switching of molecules drops to zero (~ 2000 frames; integration time: 50 msec/image; 3.84 ± 0.1 kW/cm²).

Raw SIM-images were reconstructed by either using conventional frequency space based reconstruction software,^{29,32,52} or a newly pixel-sorting based deconvolution algorithm in position space,⁵⁶ which has been developed by Gerrit Best (Kirchhoff Institute for Physics, University Heidelberg; pixelsize both algorithms: 32.25 nm). Standard widefield fluorescence images were calculated from three raw SIM-images of different phase (pixelsize: 32.25 nm). Position determination of the optically isolated SMLM-data was performed using the open source software 'PYME' (see section 2.1.5). The mean localization accuracy was $\Delta x = 10.6$ nm. Visualization of the SMLM-data was also performed with 'PYME' using a triangulation algorithm (pixelsize: 32.25 nm, when imaged with SIM- and SMLM-mode; 5 nm for SMLM-imaging only). Edges were smoothed by applying 10 random jitterings of the images. Further details concerning image acquisition and reconstruction algorithms are described elsewhere.^{39,64,134}

Further image processing and 3D visualization were conducted with Matlab and the open source software ImageJ and Vaa3D (stretch factor z: $200 \text{ nm}/32.25 \text{ nm} = 6.2$). 2D-SMLM-images were overlaid with the corresponding focal layer of the SIM-stack.

3.4.3 RPE-cell culture

Culture dishes were placed within the purchased heated incubator (see section 3.2.1), which is mounted on the microscope table, at 37° C. The culture was scanned for RPE-cells using low laser intensities in order to avoid bleaching. Then selected living cells were imaged in SIM-mode switching to slightly higher laser-intensities (\sim mWatt range). Illumination was conducted with a fine sinusoidal pattern (400 nm period) at three different phase positions. Only one orientation of the grating was chosen (0°) in order to minimize the total time for the imaging process as granules within cells tend to move ('vibrate'), which results in imaging artifacts. Raw SIM-images were reconstructed by using custom reconstruction software, which has been published in detail elsewhere.^{29,32,52} Image processing and 3D visualization were conducted with Matlab and the open source software ImageJ and Vaa3D (stretch factor z : 300 nm/32.25 nm = 9.3). RPE-cell culture experiments were mainly qualitatively analyzed in terms of practicability of the 'Combo'-setup and potential limits for visualization of the outlined questions (see section 4.4).

Donor RPE-cells: Relocation

For comparison, an overview image using transmitted light was recorded before each SIM-image acquisition. Afterwards, cells were imaged in SIM-mode. Microscope stage positions were saved in order to relocate cells after two hours for repeatedly imaging. 15 focal layers (z -direction) were recorded (300 nm steps). A density-filter position of 4 was chosen. 568 nm and 488 nm excitation were applied consecutively (Integration time: 100 msec/image).

Donor RPE-cells: Phagocytosis of beads

One day prior to the imaging process cells were fed with artificial beads (200 nm, excitation: 488 nm, Duke Scientific; final concentration: $2.39 \cdot 10^8$ beads/ml). 15 focal layers (z -direction) were recorded (300 nm steps). A density-filter position of 4 was chosen. 568 nm and 488 nm excitation were applied consecutively (Int. time: 100 msec/image).

ARPE-19 cell line: Phagocytosis of Bevacizumab

Cells were fed with labeled Bevacizumab (Avastin, 25mg/ml, Roche, 3159652) obtained from Mivenion (Berlin). Two different dyes were tested: The 6S-IDCC maleimido dye (206005, Mivenion, Berlin) is spectrally similar to a Cy5-dye (Excitation: 760 - 780 nm; Emission > 820 nm) and the 6S-ICC maleimido (205005, Mivenion, Berlin) is spectrally similar to a Cy3-dye (Excitation: 520 - 540 nm; Emission > 550 nm). Beforehand, labeled Bevacizumab was tested for the photo-switching ability of the attached dyes and em-

bedded in different media. To avoid a crosstalk with the membrane and nucleus label (GFP and RFP; section 3.3.3) Bevacizumab-6S-IDCC (~ 150 kDa) was chosen for further experiments. Cells were fed with Bevacizumab-6S-IDCC when mounted in the incubation chamber (final concentration: $10 \mu\text{g}/\text{ml}$). SIM-images were recorded after one day. 671 nm (6S-IDCC, Bevacizumab), 568 nm (RFP, membrane) and 488 nm (GFP, nucleus) excitation were applied consecutively in SIM-mode (Int. time: 100 msec/image, excitation intensity: $\sim\text{mWatt}$). A final SMLM-image series was recorded for the 671 nm color channel (Int. time: 50 msec/image).

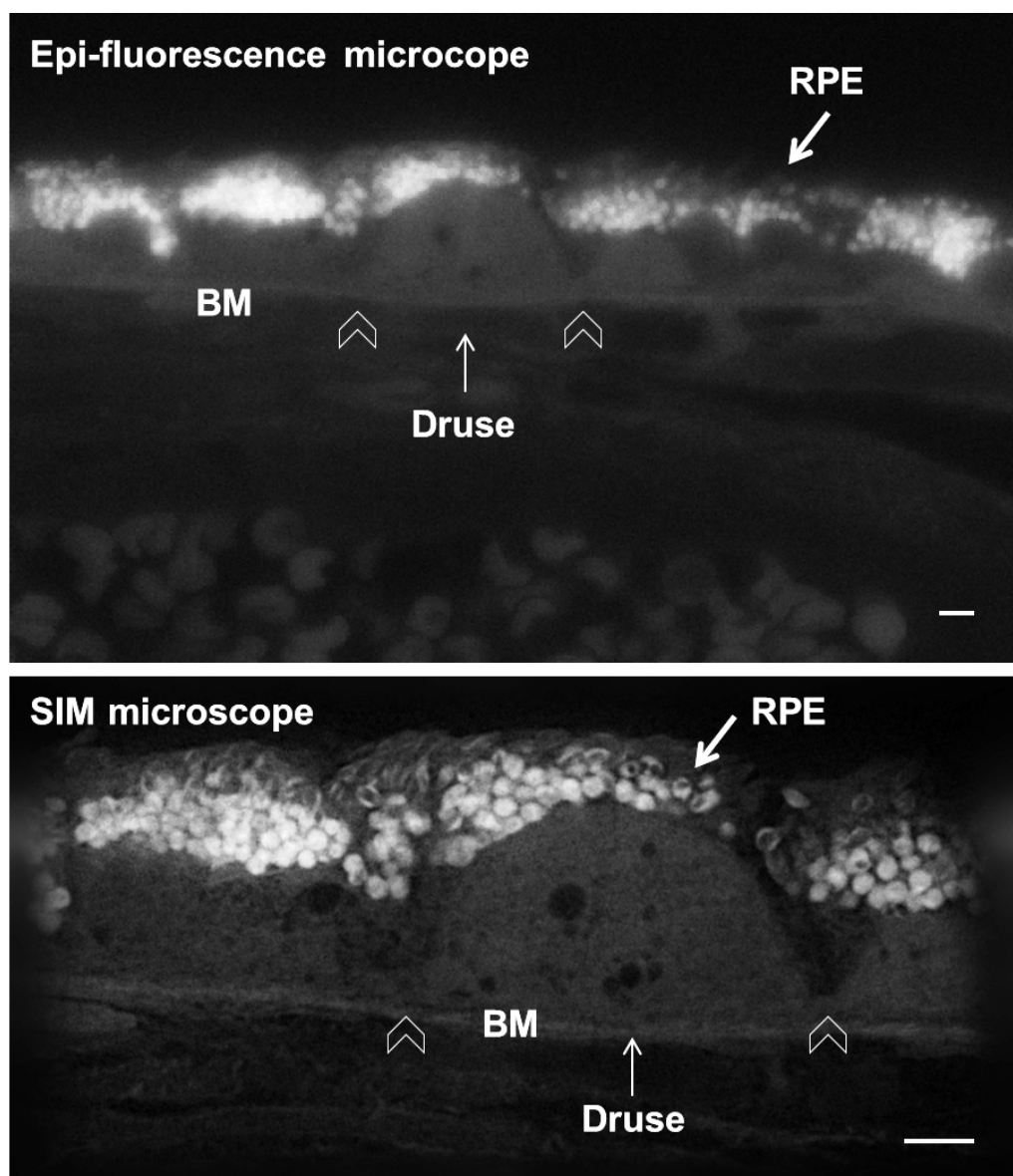


Figure 3.8: Screening of histological sections for drusen containing autofluorescent particles. **Top:** Druse imaged with an epi-fluorescent microscope with a 63x-objective. **Bottom:** Same druse imaged using the SIM-setup with a 100x-objective. LF: lipofuscin; MLF: melanolipofuscin; RPE: retinal pigment epithelium; BM: Bruch's membrane; scalebar: 2 μm

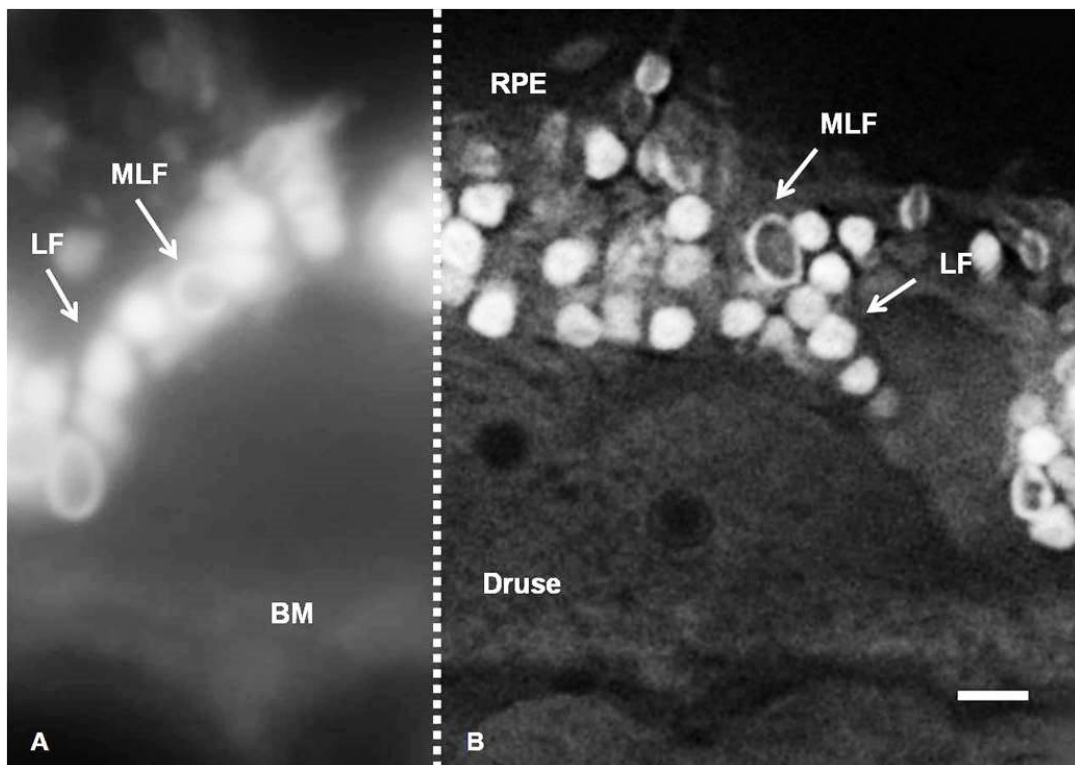


Figure 3.9: **A**: The sum of the recorded images with SIM using different phases is similar to a widefield fluorescence image acquired with a standard epifluorescence microscope **B**: High resolution image acquired with SIM and after reconstruction of the same druse (scale bar: $2\mu\text{m}$; BM: Bruch's membrane).

3.5 Simulation of Artifacts

SIM and SMLM simulations have been published individually,^{29,57} but a direct comparison between SIM, SMLM, and widefield microscopy is lacking. Simulations shown in figure 4.9 were performed using Matlab 2009a (The MathWorks Inc., Natick, MA, USA). Four sinusoidal patterns with different offsets respective to each other were generated. Afterwards images were overlaid in order to generate a double sinusoidal structure. Image size was 1,000 x 1,000 pixels with a pixel-size of 10 nm. The simulation for the SMLM image was performed by assuming $\sim 20,000$ single molecule events randomly distributed within the structure. Single molecule positions were jittered by the corresponding randomly generated localization error (mean = 10 nm, standard deviation = ± 10). The background was simulated by using $\sim 10,000$ random single molecule events per 1,000 x 1,000 pixels, with identical parameters for all simulated SMLM images. For simulating a sparse target distribution of a SMLM image $\sim 3,000$ single molecule events were generated. In order to generate a wide-field image, simulated single molecule events were blurred assuming a PSF of 200 nm. The SIM image was generated accordingly, assuming a PSF of 100 nm. As usually more fluorophores contribute to a SIM and widefield-image compared to a SMLM image, five times more fluorophores were assumed for simulation. Gaussian based visualization was performed by blurring single molecule positions with the localization error (pixel-size: 10 nm). Visualization based on a triangulation algorithm was performed by inversely translating next neighbor distances into intensity (jittering: 100, pixel-size: 10 nm). In order to smooth edges, single molecule positions were randomly jittered as described in detail in Baddeley *et al.*⁶⁴

The simulations shown in figure 4.10 were performed by Assoc. Prof. Dr. David Baddeley (Yale University, New Haven) using PYME. The pixelsize for SIM was 70 nm, the pixelsize for SMLM images was 5 nm. Visualization was performed using a triangulation algorithm. The simulations for single molecule events also consider multiple events within one frame in near vicinity in the case of very high labeling densities.

4.1 Analysis of Autofluorescent Particles within Drusen using SIM

A total of 441 drusen in eight histological sections (one central section per donor) was identified using epifluorescence microscopy. Hard and soft drusen were on average equally distributed among the eight sections (tab. 4.1). Autofluorescent (AF) material was identified within 17.9 % of all drusen ($n = 79$) when examined using epifluorescence microscopy (not shown in table), compared to 22.9 % ($n = 101$) when using SIM.

Approximately half of the AF-material containing drusen were dome-shaped with well-defined borders (54.46 %, 'hard' type of druse, tab. 4.1, fig. 4.1), as distinguished from drusen, which had poorly defined borders with endings often merging with adjacent basal linear deposits (45.54 %, 'soft' type of druse, tab. 4.1, fig. 4.2).¹⁸ The mean basal diameter of hard drusen was smaller compared to soft drusen ($29.4 \pm 26.25 \mu\text{m}$ vs. $43.12 \pm 26.25 \mu\text{m}$ respectively). Moreover, the majority of soft drusen was smaller than $63 \mu\text{m}$. According to the Wisconsin grating system drusen smaller than this size are generally assigned to the hard type.¹¹⁹ However, this result is in concordance with the histological classification of drusen by Rudolf *et al.*, who showed that drusen size and shape are not necessarily related.¹⁸ In total 90.1 % of all drusen containing AF-material were smaller than $63 \mu\text{m}$ ($35.65 \mu\text{m} \pm 23.89 \mu\text{m}$; tab. 4.2).

AF-intensity measurements allowed the signal ratio of the AF-material found in drusen to be compared with the signals of LF-granules deposited in RPE cells overlaying the druse (example shown in fig. 4.3). Here, the intensity profiles for each wavelength showed marked similarities regarding shape and maximum intensity (fig. 4.3) when comparing

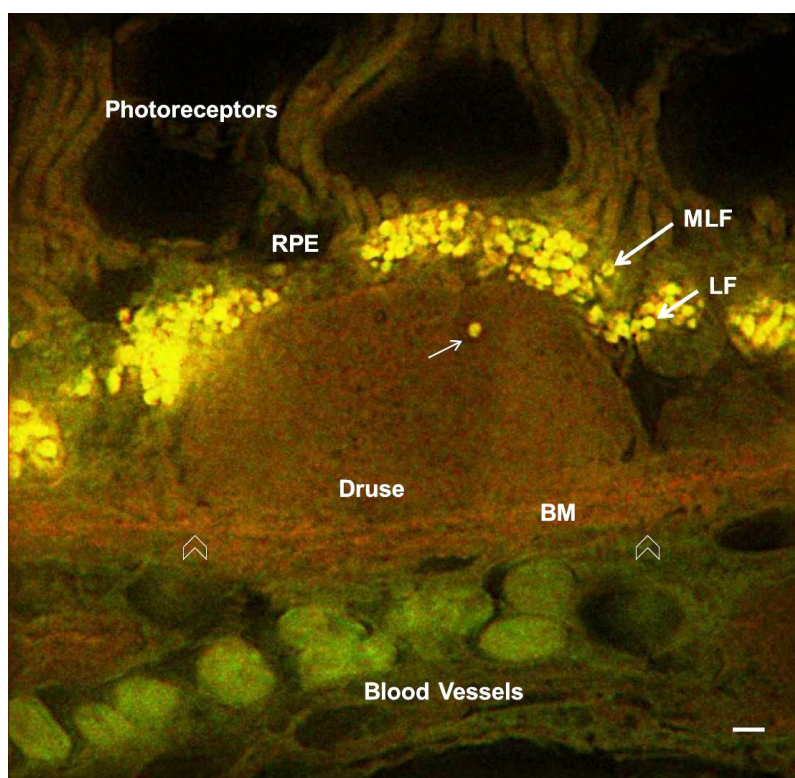


Figure 4.1: *Typical autofluorescent particle found within a hard druse smaller than $63\ \mu\text{m}$ (size of druse: $31.08\ \mu\text{m}$ (arrowheads); LF: lipofuscin; MLF: melanolipofuscin; RPE: retinal pigment epithelium; BM: Bruch's membrane; scalebar: $2\ \mu\text{m}$; red channel: $488\ \text{nm}$ excitation; green channel: $568\ \text{nm}$ excitation). From Rossberger et al.²*

a RPE-LF granulum with an AF particle embedded in the druse. AF intensity of the RPE-LF granule was higher at $488\ \text{nm}$ (max. intensity: $213\ \text{a.u.}$) than at $568\ \text{nm}$ (max. intensity: $45\ \text{a.u.}$). The ratio of the maximum intensity at $568\ \text{nm}$ excitation compared to $488\ \text{nm}$ excitation was 0.21 . A similar intensity profile and ratio was observed for the AF particle embedded in the druse (max. intensity at $488\ \text{nm}$: $203\ \text{a.u.}$; at $568\ \text{nm}$: $42\ \text{a.u.}$; intensity ratio $568/488 = 0.21$). These similarities have been observed for other AF-particles within drusen as well.

A total of 190 AF-particles were found in 101 drusen (tab. 4.3a). Single drusen contained on average one AF-particle. However, few drusen contained more than one AF-particles (maximum: 14 AF-particles within a single druse). Some particles appeared like LF-granules in RPE cells. Others were smaller than RPE-LF granules and a few lacked the characteristic round shape, though the intensity ratio given by the two excitation wavelengths was similar to LF-granules of the RPE (fig. 4.4). AF-particles within drusen had a median size of $705 \pm 298\ \text{nm}$, where 57 (30%) AF-particles were smaller than $500\ \text{nm}$ (tab. 4.3a). Most (85.94%) AF-particles were located in the lower two-thirds of the drusen, between Bruch's membrane (BM) and RPE. The distance between a AF-particle and BM was on average $6.3 \pm 7.1\ \mu\text{m}$, which is 54% of the average drusen height ($11.7\ \mu\text{m} \pm 6.9\ \mu\text{m}$). An overview is given in table 4.3b.

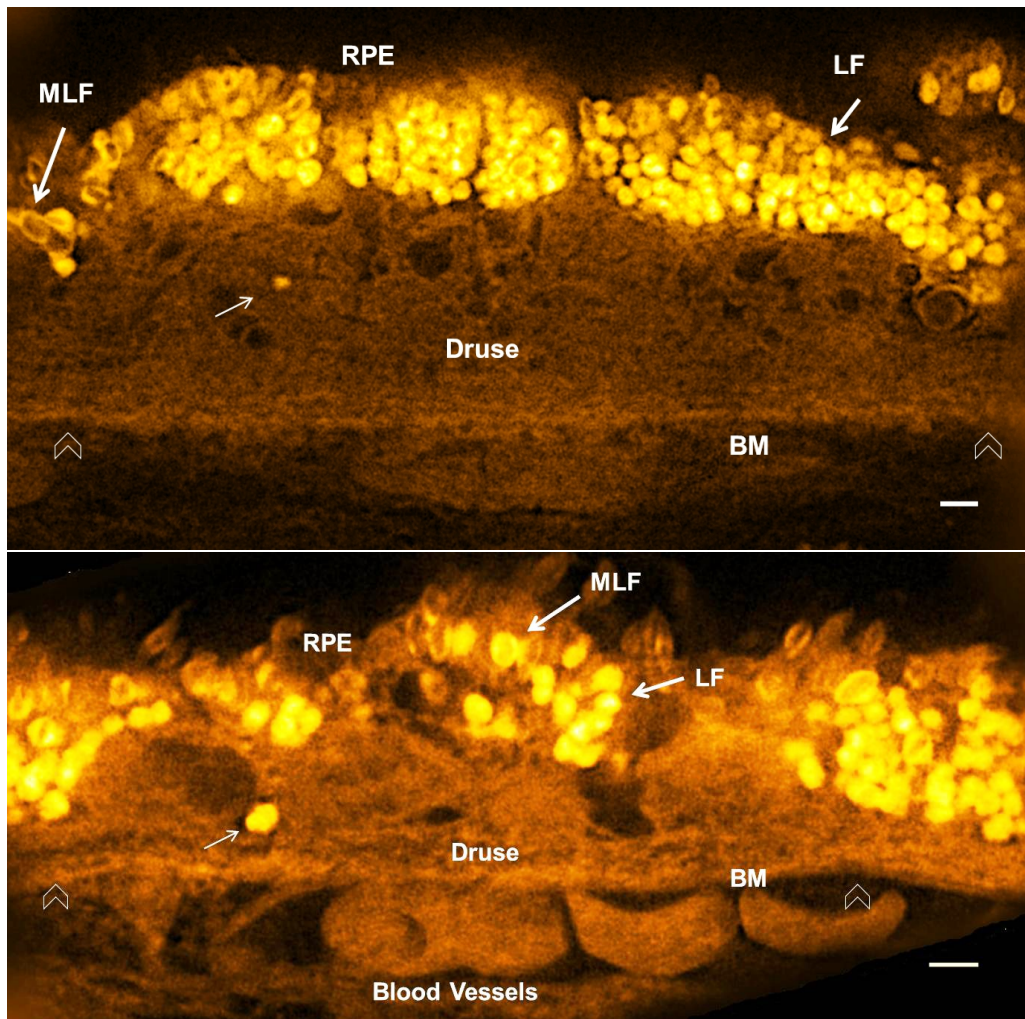


Figure 4.2: Typical autofluorescent (AF) particles found within soft drusen smaller than $63\ \mu\text{m}$. **Top:** Size of druse: $47.35\ \text{nm}$ (arrowheads). From Rossberger et al.². **Bottom:** Size of druse: $22.27\ \mu\text{m}$ (arrowheads). LF: lipofuscin; MLF: melanolipofuscin; RPE: retinal pigment epithelium; BM: Bruch's membrane; scalebar: $2\ \mu\text{m}$

To calculate the volume-fraction of drusen that is occupied by AF-particles, the AF-particle was assumed to be spherical. Figure 4.6 shows the relationship between drusen and AF-particle volumes. Visual inspection and low r^2 values with either a linear or exponential fit revealed no correlation between drusen and AF-particle size.

Sample	Epifluorescence Microscope			Structured Illumination Microscopy		
	# Drusen	# Soft Drusen	# Hard Drusen	# Drusen with Particles	# Soft Drusen with Particles	# Hard Drusen with Particles
80y, f	92	42	50	23	12	11
95y, m	55	22	33	15	6	9
78y, m	29	7	22	2	1	1
57y, m	37	16	21	7	2	5
79y, m	65	57	8	10	5	5
63y, m	10	1	9	6	1	5
73y, m	71	59	12	12	7	5
84y, f	82	27	55	26	12	14
Total	441	231	210	101	46	55
%	100	52.38	47.62	22.90	45.54	54.46

Table 4.1: Characteristics of drusen of eight central histological sections using epifluorescence microscopy and structured illumination microscopy (m: male, f: female). From Rossberger et al.²

Sample	Hard Drusen			Soft Drusen		
	< 63 μm	63 μm - 125 μm	> 125 μm	< 63 μm	63 μm - 125 μm	> 125 μm
80y, f	11	0	0	11	1	0
95y, m	0	0	0	4	2	0
78y, m	1	0	0	1	0	0
57y, m	4	1	0	2	0	0
79y, m	5	0	0	3	1	1
63y, m	5	0	0	1	0	0
73y, m	3	2	0	7	0	0
84y, f	14	0	0	10	2	0
Total	52	3	0	39	6	1
%	51.49	2.97	0.00	38.61	5.94	0.99

Table 4.2: Drusen imaged with SIM and found to contain fluorescent particles were distinguished into hard and soft type.¹⁸ Additionally, a size classification was conducted according to the Wisconsin grading system.¹¹⁹ From Rossberger et al.²

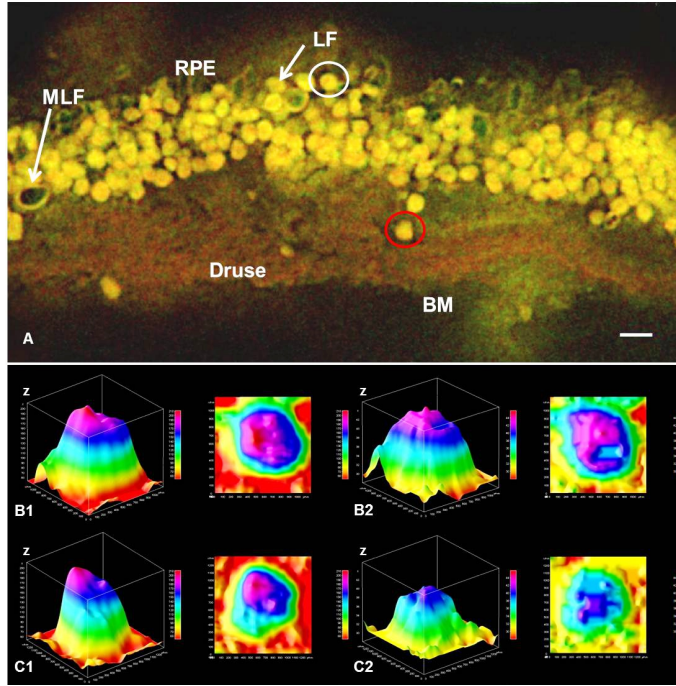


Figure 4.3: Auto-fluorescence (AF) profiles of a particle within a druse and RPE-LF. The comparison of profiles shows marked similarities in terms of fluorescence properties and shape. **A:** Typical AF-particles found within a soft druse (size of druse: $48.18 \mu\text{m}$; scalebar: $2 \mu\text{m}$; red channel: 488 nm excitation; green channel: 568 nm excitation; LF: lipofuscin; MLF: melanolipofuscin; RPE: retinal pigment epithelium; BM: Bruch's membrane). **B:** Intensity profile of a LF granule within a RPE cell overlaying the druse (white circle; z : intensity [a.u.]; B1: 488 nm excitation, max.: 200 a.u. ; B2: 568 nm excitation, max.: 42 a.u.). **C:** Intensity profile of an AF particle within a druse (red circle; z : intensity [a.u.]; C1: 488 nm excitation, max.: 200 a.u. ; C2: 568 nm excitation, max.: 42 a.u.). From Rossberger et al.²

Sample	# Autofluorescent Particles	ϕ Size Particles [μm]	# Particles $< 0.5 \mu\text{m}$
80y, f	29	0.56	12
95y, m	29	0.95	2
78y, m	2	0.70	0
57y, m	15	0.95	1
79y, m	28	0.50	17
63y, m	6	0.52	3
73y, m	41	0.69	10
84y, f	40	0.72	12
Total	190	0.7	57
%	100	---	30

(a) Fluorescent particles embedded in drusen: Size and number of particles smaller than 500 nm are shown. From Rossberger et al.²

Median Sizes	[μm]
Size Particles	0.705 ± 0.022
Distance to BM	6.29 ± 0.52
Distance to Basis	35.65 ± 2.38
Hard Drusen Basis	29.40 ± 2.68
Soft Drusen Basis	43.12 ± 3.87
Drusen Heights	11.68 ± 0.67

(b) Drusen study: Median values.

Table 4.3: Evaluation of autofluorescent particles found within drusen.

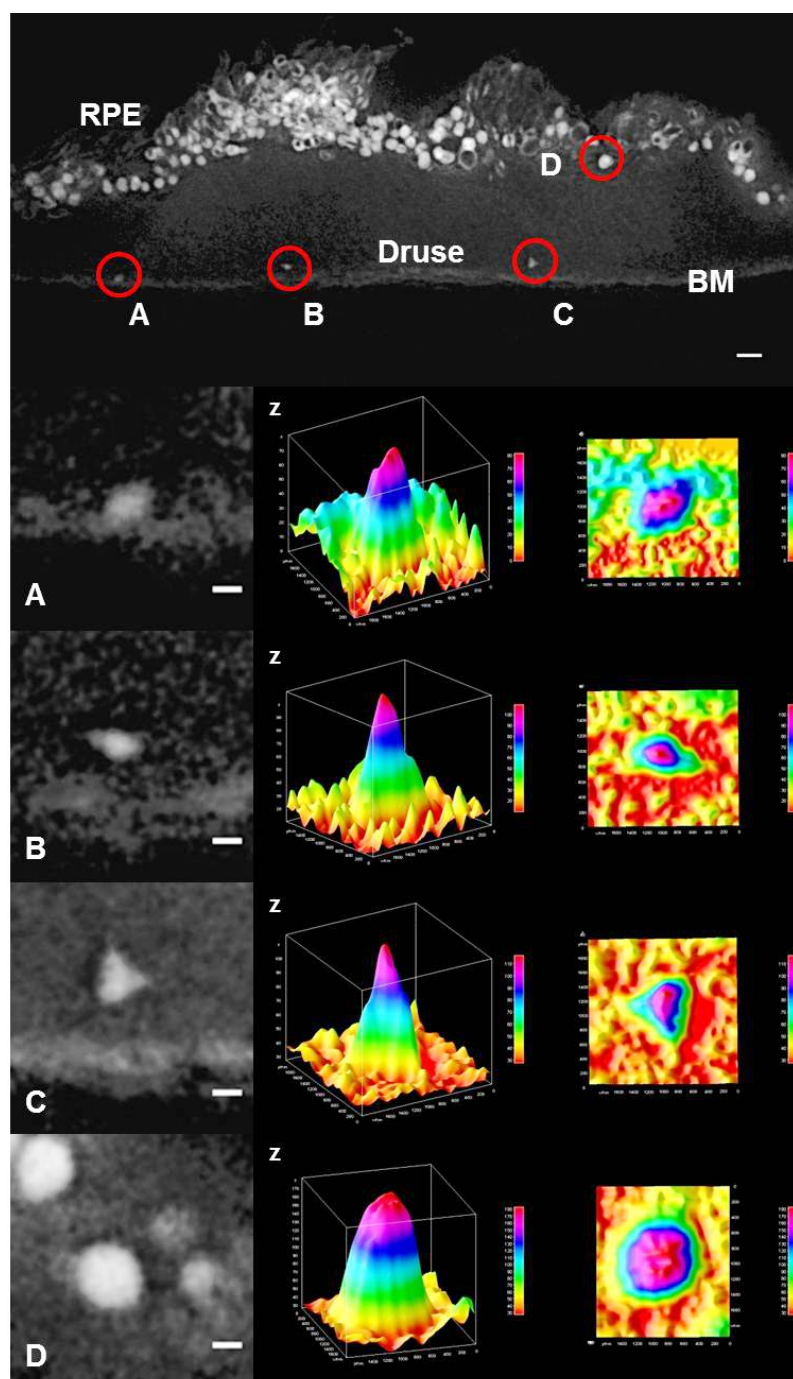


Figure 4.4: *Autofluorescence (AF) profiles of particles smaller than 500 nm within a druse (A, B, C; z: intensity [a.u.]). The small particles show similar fluorescence properties as RPE-LF granules (D; z: intensity [a.u.]) though size (left row) and shape lack the typical round-shaped appearance (right row). As particles are smaller, maximum intensities emitted (max.: ~ 100 a.u.) were generally lower compared to RPE-LF (max.: 180 a.u.) presumably due to less LF accumulation (size of druse: $66.88\ \mu\text{m}$; scalebar: $2\ \mu\text{m}$; magnification: $300\ \text{nm}$; excitation: $488\ \text{nm}$; RPE: retinal pigment epithelium; BM: Bruch's membrane). From Rossberger et al.²*

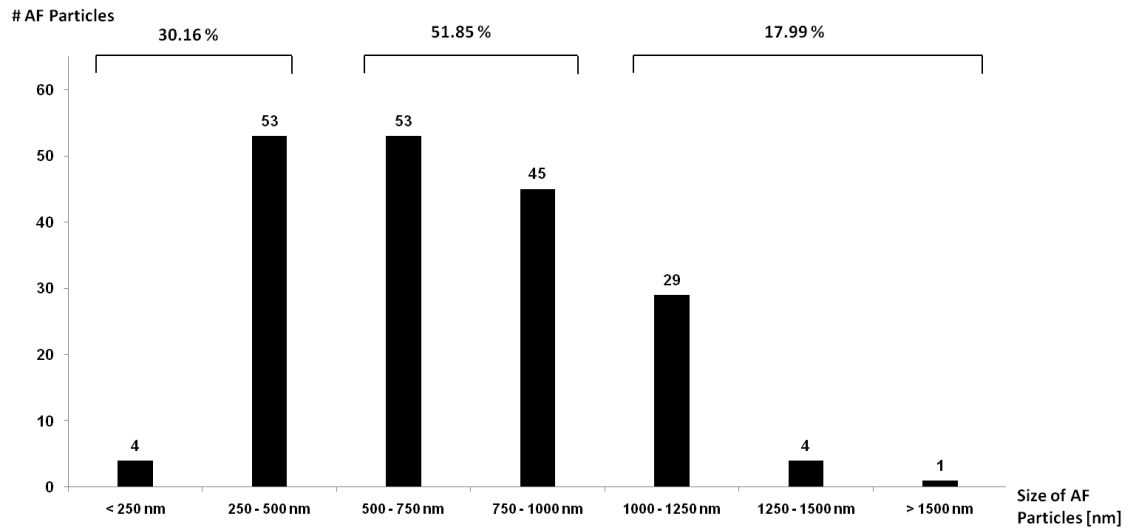


Figure 4.5: Size distribution of autofluorescent particles within drusen: 30.16 % of all particles were smaller than 500 nm. From Rossberger et al.²

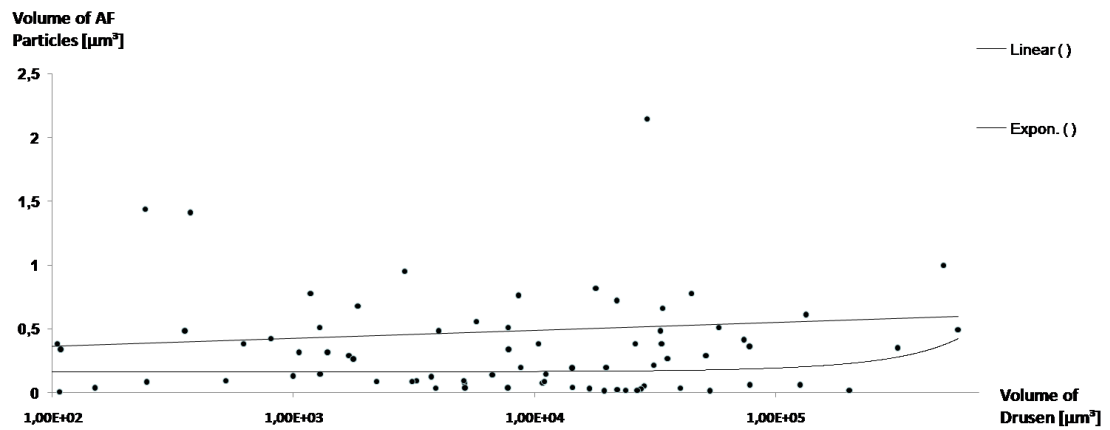


Figure 4.6: Volume of AF-particles plotted against the volume of the corresponding druse. A linear and exponential trend line was applied. From Rossberger et al.²

AF ring-like structures within drusen

Apart from AF-particles, other autofluorescent structures were also observed within drusen. In several drusen, a total of 37 ring-like structures of varying size and shape were recorded. Only a few AF ring-structures are round-shaped with a strong AF ring-like border. In most cases, a 'cigar-shaped' structure that contained a non-fluorescent core was observed (fig. 4.7, red arrow). On average, ring-like AF-structures were larger than AF-particles, with a median length of 1240 ± 80 nm along the long axis. A maximum of three ring-like structures are observed within one druse. Most ring-like AF-structures were located in the lower two-thirds of the druse (97.3 %).

In figure 4.7 a comparison of fluorescent spectra between a typical LF- (fig. 4.7-B2) and MLF-granule (fig. 4.7-C2) within the RPE (indicated by white arrows, fig. 4.7) and the 'cigar'-shaped structure (fig. 4.7-D2) is shown. Line-plots (fig. 4.7: B1-D1) are depicted for each particle using a 488 nm excitation line (distance vs. gray-value). The LF-granule shows a homogeneously distributed fluorophore distribution across its diameter (fig. 4.7-B), whereas the MLF-granule consists of a fluorescent ring with a core of significantly lower AF-signal (fig. 4.7-C) as already demonstrated.⁸⁸ This 'volcanic'-shaped spectrum can also be observed for the 'cigar'-shaped structure (fig. 4.7-D). However, the fluorescent signal typically varies quite strongly across the AF-ring. Therefore, a ratio calculation is not significant. In some structures the AF-ring is even unclosed as shown in figure 4.8 (A: blue and red arrows). Spectra for 488 nm (fig. 4.8-B1) and 568 nm (fig. 4.8-B2) are plotted exemplarily for one unclosed AF-structure (fig. 4.8-A: blue arrow). Maximum intensity values yielded 210 a.u. for 488 nm excitation and 180 a.u. for 568 nm excitation. A ratio calculation was not conducted due to previously explained reasons. In few cases AF-ring-like structures are even found beyond BM (green arrow). Only in one very small druse (early drusen) an AF-structure shaped similar to MLF was found, appearing as an AF ring with a significant lower AF-signal within the core (not shown).

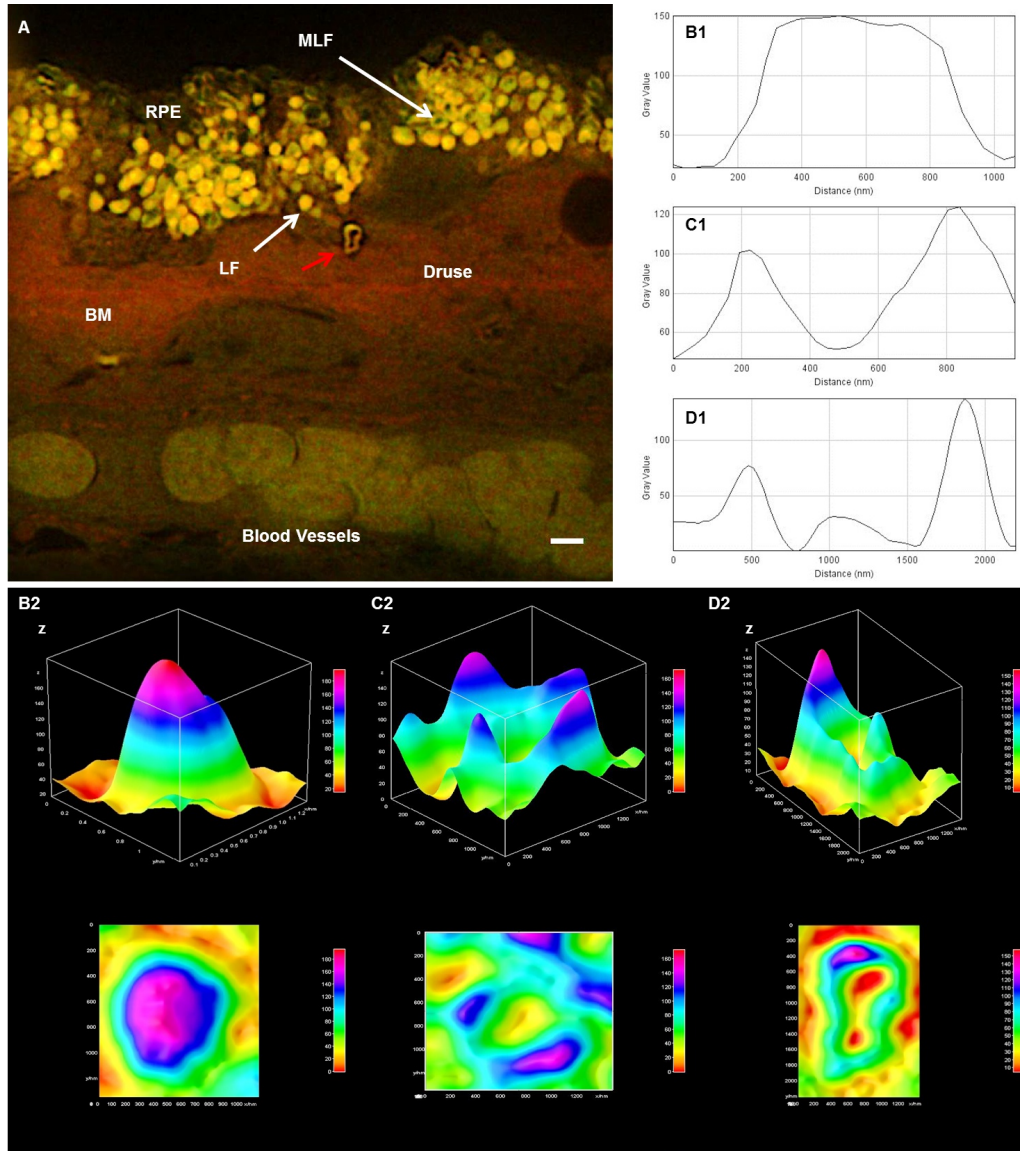


Figure 4.7: **A**: An autofluorescence (AF) 'cigar'-shaped ring-structure (red arrow) within a druse or potentially just released into a druse (scalebar: $2\ \mu\text{m}$; red channel: $488\ \text{nm}$ excitation; green channel: $568\ \text{nm}$ excitation; LF: lipofuscin; MLF: melanolipofuscin; RPE: retinal pigment epithelium; BM: Bruch's membrane). **B2-D2**: AF-profiles of the 'cigar'-shaped structure (D2) within a druse in comparison with RPE-LF (B2) and -MLF (C2). The comparison of MLF-AF-profile and the AF-profile of the 'cigar'-shaped structure show marked similarities. A dark core is surrounded by a strong AF-ring, whereas the LF-AF does not show a dark core as expected (z : intensity [a.u.], $488\ \text{nm}$ excitation). **B1-D1**: The same observation is maintained from a line-plot across the granules/structure (x : distance [nm]; y : gray value; $488\ \text{nm}$ and $568\ \text{nm}$ excitation).

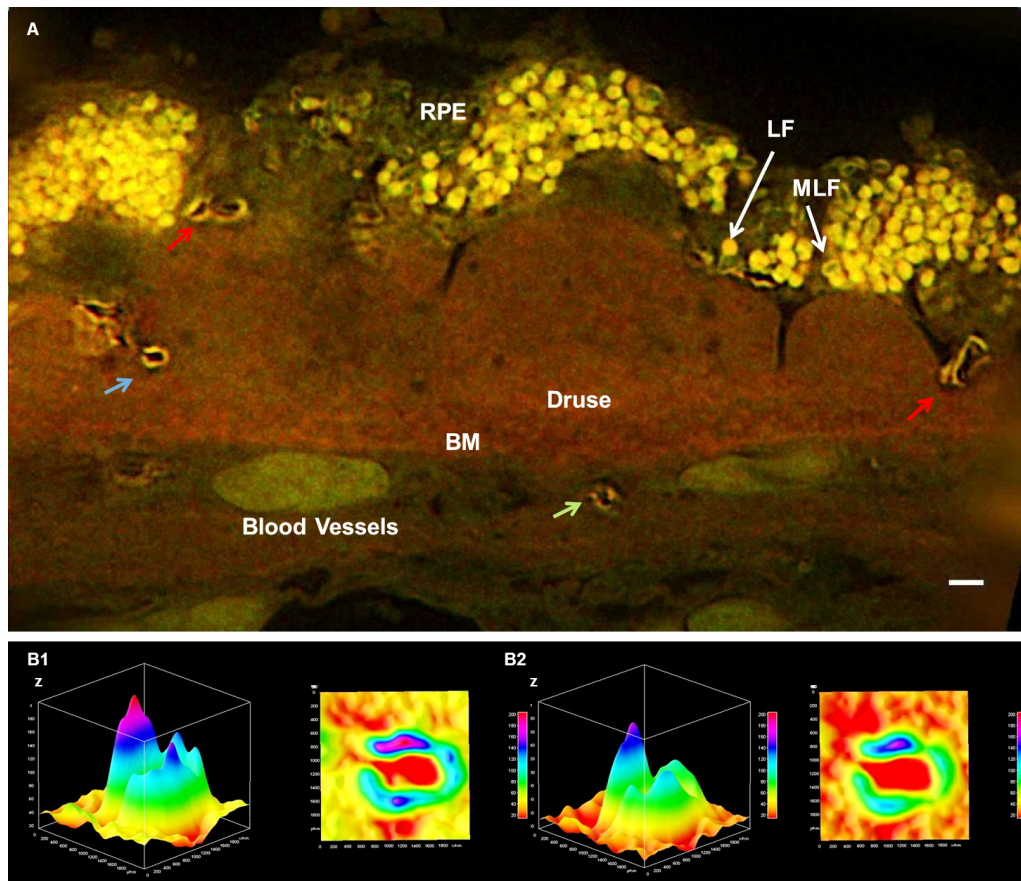


Figure 4.8: **A**: Different unclosed ring-like autofluorescent (AF) structures observed within drusen (scale-bar: $2\ \mu\text{m}$; red channel: $488\ \text{nm}$ excitation; green channel: $568\ \text{nm}$ excitation; LF: lipofuscin; MLF: melanolipofuscin; RPE: retinal pigment epithelium; BM: Bruch's membrane). **B1-B2**: AF-intensity spectra are exemplarily depicted for a ring-like AF-structure (blue arrow) at different excitation wavelengths (z : intensity [a.u.]; B1: $488\ \text{nm}$ excitation, max.: $210\ \text{a.u.}$; B2: $568\ \text{nm}$ excitation, max.: $180\ \text{a.u.}$). In few cases AF-ring-like structures are observed beyond BM (green arrow).

4.2 Resolution and Artifacts in SMLM & SIM Imaging

Figure 4.9 and 4.10 compare simulated conventional widefield, structured illumination (SIM) and single molecule localization microscopy (SMLM) images. For this purpose, SMLM and SIM have been applied to a simulated sinusoidal pattern (fig. 4.9-I). Figure 4.9-II shows the simulated widefield fluorescence image, as expected when using a conventional fluorescence microscope. At many positions, the structure is not resolved (white arrow). Figure 4.9-III displays the corresponding SIM image, where resolution was enhanced by a factor of two. The SIM image is not only able to resolve the two sinusoidal lines within the peaks of the generated structure but also within the area of high gradients, whereas the conventional widefield method (fig. 4.9-II) is not capable of this. The SMLM image is able to reveal this detail even better, due to the higher resolution provided (fig. 4.9-IV-VI). Applying a Gaussian algorithm for the localization of SMLM signals is the most common procedure in order to generate structural information (fig. 4.9-V). However, this visualization method usually results in a loss of resolution compared to the actual data, as positions are often blurred with the standard deviation of the corresponding localization accuracy. A triangulation algorithm⁶⁴ is usually superior to a Gaussian visualization in terms of conserving resolution provided by the raw data (fig. 4.9-VI). In this case, the two lines of the sinusoidal pattern are clearly resolved. A limitation arises when the triangulation algorithm is applied to a sparse target distribution (fig. 4.9 VII-IX), which does not produce sufficient structural information⁶⁴ (fig. 4.9-IX). In this case an overlay of the SMLM image with a widefield fluorescence image is desirable.

The conventional widefield fluorescence image is not able to resolve the inner structure of the simulated pattern (arrow in figure 4.9-II), and structural information can be hardly assigned to the single molecule events of the SMLM image. The highly resolved SIM image can be used in order to provide sufficient structural information. As a result, in most cases single molecule events can be located within the corresponding structure of the target and thus provide actual information about location and distribution, making it finally possible to gain nano-structural insights that have previously been inaccessible.

Figure 4.10 presents another simulated example. Simulation was conducted by Assoc. Prof. Dr. David Baddeley (Yale University, New Haven). In biology, two crossing lines might be represented e.g. by two actin fibers crossing each other. Simulations were performed in order to compare structures with varying fluorophore densities per recorded image frame (4.10-III-V). Widefield- (4.10-I) and SIM-image (4.10-II) of the same structure are illustrated as well. A continuous labeling density is assumed including a higher fluorophore density in the area of the overlap. The same structure is shown for a sparse labeling density (few fluorophores: 4.10-III), an average number of fluorophores detected

(4.10-IV) and for a very high labeling density (many detected fluorophores: 4.10-V). Comparing the magnification of the different labeling densities in the lower row (4.10: A-C) it is obvious that desired resolution depended strongly on labeling density. Visualization of low labeling densities (fig. 4.10-A) using a triangulation algorithm⁶⁴ does not resolve two separate structures in the vicinity of the two lines crossing. This situation can also occur due to high bleaching rates of the fluorophores ('bleaching artifacts'). In comparison the visualization of a normal fluorophore density (fig. 4.10-B), which assumes only one fluorophore per diffraction limited area, reveals two separate lines. However, gaps are present though the underlying structure appears continuous. These results are typical for real SMLM-data. Not all fluorophores are necessarily excited and detected. Orientation of the dipole momentum, the micro-environment or background issues heavily influence SMLM-detection.

Whether a fluorophore is excited is depended on the relative orientation of the dipole momentum of the single fluorophores and the propagation vector of the incident electromagnetic wave (photon).

A varying micro-environment within the sample can also negatively affect single molecule detection. Photo-switching of fluorophores is highly dependent on the micro-environment. Within the area of the missing signals, the micro-environment might potentially not have favored the blinking behavior of the single molecules and thus did not contribute to the image-acquisition, although labeling might have been present. A comparison with the SIM-image could reveal this information.

In addition, background issues may play a key-role in single molecule detection as out-of-focus single molecule events contribute to locally evaluated background levels ('shading'-artifacts). As a result, several single molecule events cannot be separated from the high background. Thus, locally reduced total numbers of detected signals are evaluated. Moreover, background levels do not tend to be homogeneous throughout the whole specimen. Usually inhomogeneities are present, resulting in a variable detection efficiency. Drifts occurring during the relatively long data acquisition may also distort single molecule positions. A highly-resolved SIM-image can help to identify drift-related displacements and would allow mathematical corrections of SMLM data.

Very high labeling densities also clearly produce prominent artifacts (fig. 4.10-C), while the structure is clearly resolved. Diffraction limited intensity distributions (PSFs) of single fluorophores in the near vicinity to each other overlap within the same recorded frame. The fitting procedure is not conducted separately but together for both single molecule signal. Hence a large standard deviation of the fitted Gaussian function is evaluated, signals are discarded from the total number of detected single molecule events during post-processing and visualization ('collision artifacts'). This procedure consequently could lead to gaps in

the target (fig. 4.10-C, white arrows), though the structure appears continuously labeled as revealed by the SIM-image (fig. 4.10-II). As a result, an information loss could potentially occur though the labeling efficiency was very good. Nevertheless, the opposite effect could occur as well when applying visualization algorithms on SMLM-data. In case of high event densities, visualization algorithms may tend to fill gaps between closely spaced structures although the SIM image would potentially reveal two separate structures. In both cases a comparison of both data sets could reveal the described artifacts and reduce a potential information loss. When evaluating whether labeling in specific areas is present or not it also needs to be considered that both methods provide different suppression capability for out of focus signals (z-sectioning). Continuously labeling appearing within a SIM image but not within a 2D-SMLM image could be due to the lower optical sectioning from other focal planes, where labeling was present. A 3D-SIM-recording could help to verify whether labeling is present within the focal plane or not. This case will be demonstrated in the next section.

Based on the discussed artifacts related to each imaging method, it is clearly desirable to compare SIM and SMLM of the same imaged region of interest in order to avoid misinterpretation of the recorded data.

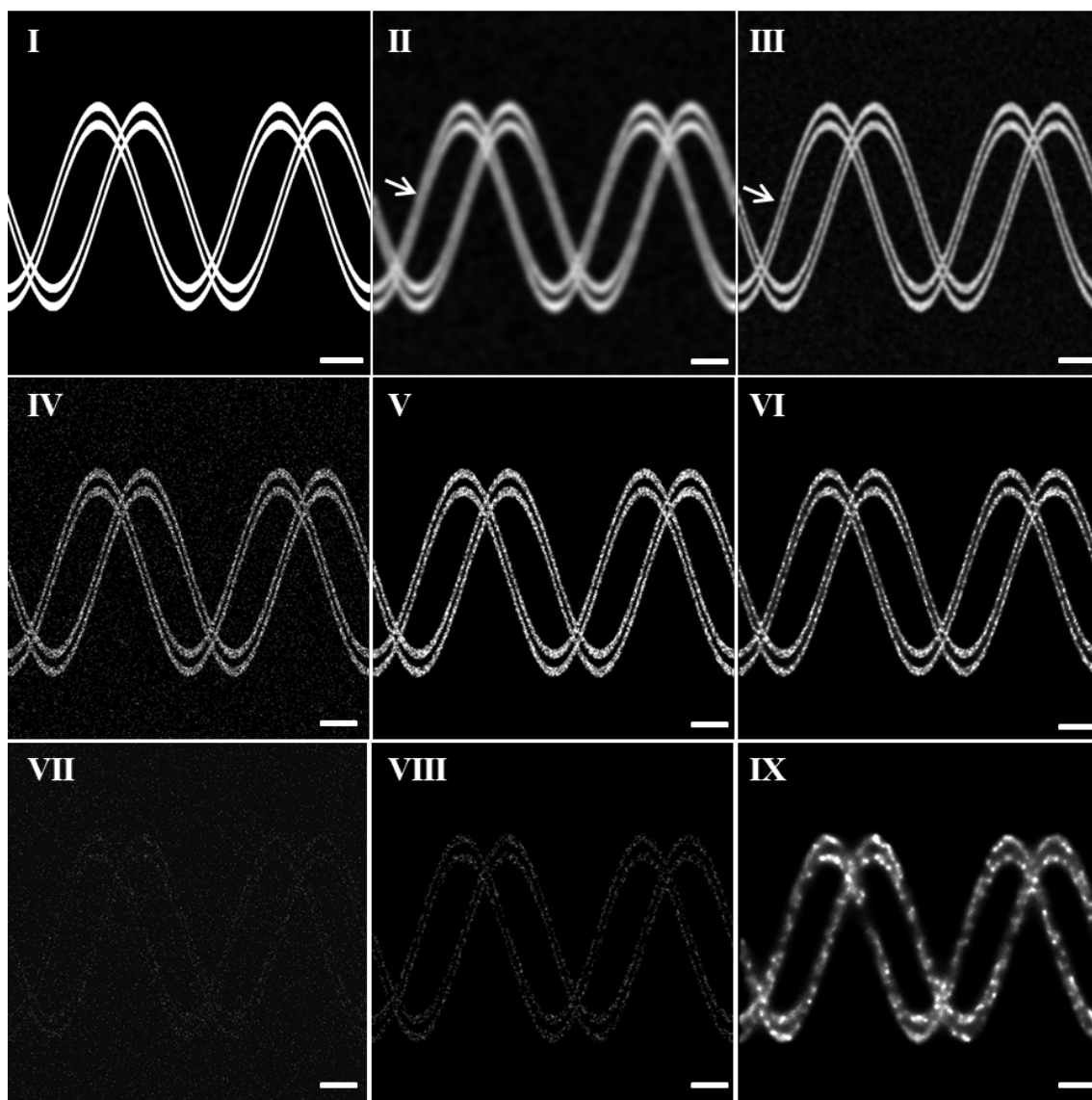


Figure 4.9: Comparison of conventional widefield fluorescence microscopy, SIM, SMLM and illustration of visualization methods for SMLM (simulation details: see section 3.5): **I**: Simulated structure within a target object. **II**: Simulated conventional widefield fluorescence image. **III**: Simulated SIM image. **IV**: Simulated single molecule localization data (SMLM, position data set). **V**: Visualization of the localization data in IV using a Gaussian based algorithm.⁶⁴ **VI**: Visualization of the localization data in IV using a triangulation algorithm.⁶⁴ **VII**: Simulated sparse target distribution of localization signals assuming the same structure within the target object. **VIII**: Visualization of the localization data in VII using the Gaussian algorithm. **IX**: Visualization of localization data in VII using the triangulation algorithm (scalebar: $2\mu\text{m}$). From Rossberger et al.¹

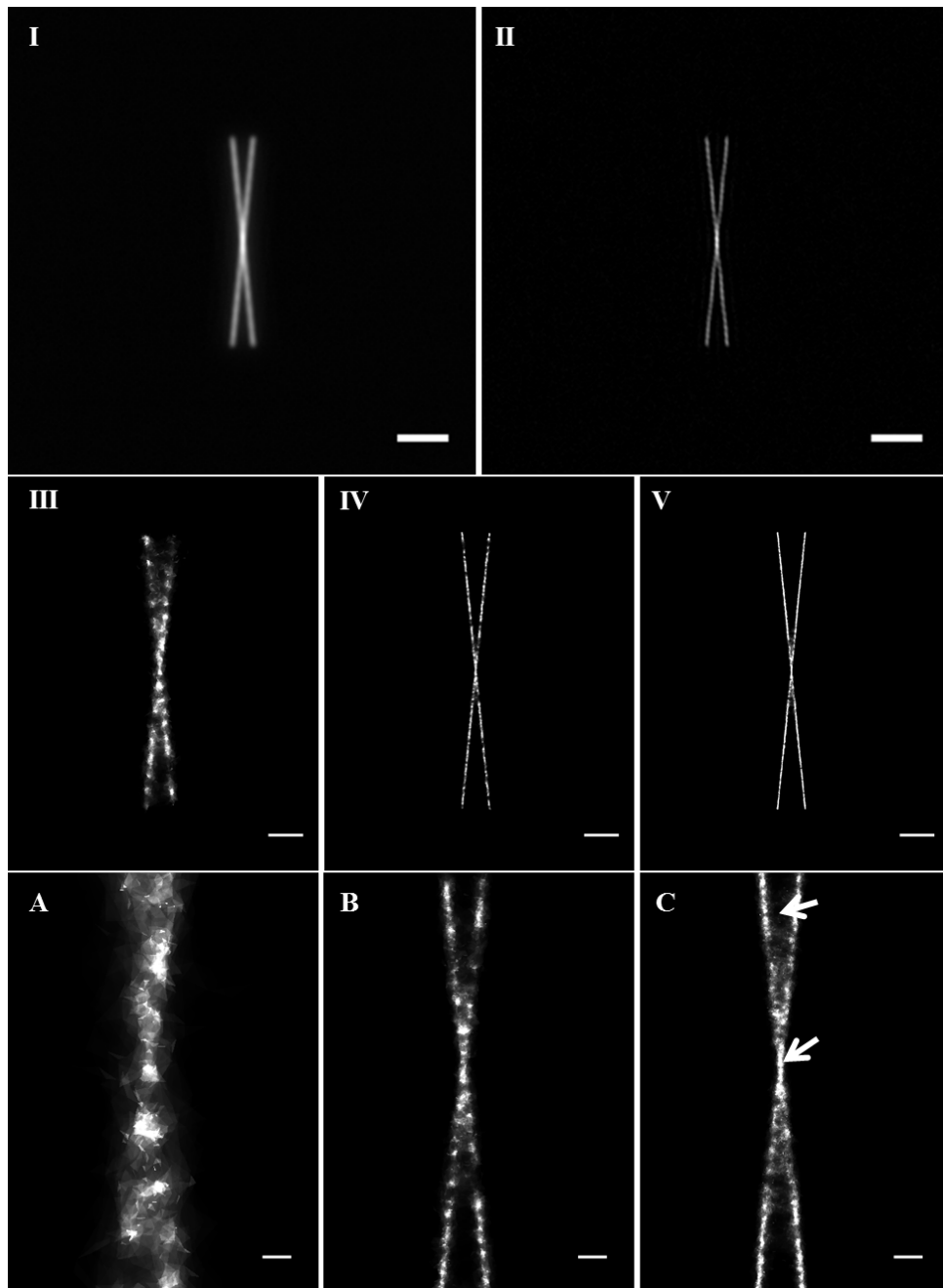


Figure 4.10: Simulation of different event densities for SMLM: **I**: Widefield image. **II**: SIM image. **III**: Highly bleached or sparsely labeled SMLM data (low event densities). **IV**: Medium densely distributed single molecule events visualized with a triangulation algorithm⁶⁴. **V**: Very densely distributed single molecule events. **A-C**: Corresponding magnifications of the crossing regions for the different event densities. **A**: Low event densities (**III**) are not able to resolve the crossing of the two lines properly. **B**: Medium densely packed (**IV**) single molecule events clearly reveal the crossing section. However, gaps within the lines occur although the structure is continuous. **C**: Multiple fluorophores (**V**) are localized within the same frame and within a diffraction limited area. As a result the localization algorithm discards events with insufficient optical isolation from the final image. The crossing is still clearly resolved though the visualization produces various artifacts in the signal density (white arrows). Simulations were performed by Assoc. Prof. Dr. David Baddeley (Yale University, New Haven). From Rossberger et al.¹

4.3 Co-localization Analyses with the 'Combo'-Setup

In order to demonstrate the function of the newly built 'Combo'-microscope, the axon initial segment (AIS) of retinal ganglion cells was imaged. As these cells are located in the outer layers of the retina an interference with AF signal arising from the RPE can be avoided for first demonstration purposes. Moreover, the AIS represents an essential strategic center of the visual signal transduction pathway. Pathological changes of the AIS inhibit signal transduction in the visual pathway and potentially result in loss of vision due to the fact that the AIS is the essential membrane domain generating action potentials in neurons.¹³⁵ As little is known about the structure and functionality of the AIS of retinal ganglion cells, it is of great interest to reveal structural information and composition on a high resolution level. Naturally, a 3D-visualization revealing spatial protein-substructure of the AIS would offer tremendous new insight.

Figure 4.11 shows a 2D-SIM and a 3D-SIM data set completed by a 2D-SMLM image, which were sequentially recorded with the 'Combo'-setup. The SMLM-data was visualized with a triangulation algorithm.⁶⁴ Immunofluorescence labeling of the AIS was achieved by a specific antibody against β -IV-spectrin, a major anchor protein of the AIS which connects the axon membrane scaffold ankyrin-G (ankG) with the inner actin cytoskeleton of the axon (see schematic in fig. 4.16). It therefore appears rather close to the surface of the AIS membrane. The AIS was labeled for β -IV-spectrin (Alexa 568), a protein spanning the cytoskeletal AIS network and is therefore located near to the membrane of the AIS. As it is known that spectrin is a membrane associated protein, this specimen may constitute a good test object to demonstrate the resolution obtainable with the various modes of the 'Combo'-setup constructed.

The resolution improvement gained by SIM and SMLM compared to conventional widefield fluorescence microscopy is demonstrated (fig. 4.11: A I-III). An overlay of the recorded SIM-image followed by a super-resolved single molecule data set is shown as well (fig. 4.11: A-IV). The 2D-SIM image suggests that the whole AIS is elongated within a certain focal area. However, when taking the 2D-SMLM data set into account, it is clear that SMLM provides a better z-sectioning compared to SIM (fig. 4.11: B III-V; white circles). Single molecule signals can be filtered according to total photon-numbers and the width of the fitted model function. Applying an appropriate threshold excludes single molecule signals from other focal areas. Therefore, the SMLM-image (fig. 4.11: A-III) does not depict the whole AIS, while the SIM-image does (fig. 4.11: A-II). This observation is confirmed when studying the 3D-SIM depiction of the same AIS (fig. 4.11: B VI-X). The AIS turns across its dimensions (fig. 4.11: B VI-X: white arrows), which is in concordance with the prior discussed SMLM-image. The 3D-depiction of a standard widefield fluorescence image of the same AIS is hardly able to resolve these details (fig. 4.11 C I-V).

Figure 4.12 shows a magnification of figure 4.11 depicting the resolution improvement gained by SIM (fig. 4.12: B) and SMLM (fig. 4.12: C) compared to conventional widefield fluorescence microscopy (fig. 4.12: A). While the widefield image (fig. 4.12: A) does not reveal any substructure of the AIS, the SIM image (fig. 4.12 B) indicates a substantial heterogeneity in the distribution of the β -IV-spectrin signals. On the single molecule level (fig. 4.12: C) this heterogeneity in the signal distribution becomes even more prominent. For quantitative analysis, intensity distributions for a selected cross section of the AIS were plotted (fig. 4.12: A-C). Whereas in the conventional widefield fluorescence image, the apparent width of the line plot was around 700 nm, the SIM and SMLM line plots indicated a considerably smaller width of the AIS (110 ± 10 nm for SMLM, 160 ± 20 nm for SIM; localization accuracy SMLM: $\delta x = 16.2$ nm). In contrast to the conventional widefield fluorescence image, the SIM line plot indicates a heterogeneity of the β -IV-spectrin signal distribution. This heterogeneity becomes much more prominent in the SMLM line plot: In this case, two clearly separated signal distributions across the AIS are observed, each of them with an apparent half-width below the conventional resolution limit. As the SMLM shows a cross section of the AIS, each line depicts β -IV-spectrin located near to the AIS membrane. Another important feature is the substantial gain in image contrast obtained by the suppression of background noise by the algorithms used.

The SMLM image (fig. 4.12: C-I and C-II) does not depict a homogeneous single molecule signal density across the whole AIS (white arrows), though the widefield as well as the SIM-image show a significant fluorescence signal for the whole AIS length. This observation can be explained with the z-extent of optical sections generated by the two methods. The 2-beam SIM reconstruction software provides an optical sectioning of 500-600 nm along the optical axis, whereas the SMLM algorithm is able to increase the optical sectioning to values smaller than 300 nm due to strict filtering of single molecule signals. Detected signals exceeding a certain width are eliminated from the positions taken into account for the visualization. Signals with a large FWHM are usually arising from out of focus objects. Consequently, within the SMLM image more parts of the AIS of the ganglion cell are out-of-focus than in the SIM mode, which is clearly illustrated in the 3D-visualization of the AIS in figure 4.11-B. Based on the 3D-SIM-depiction of the whole AIS, a varying micro-environment, 'collision'-artifacts or 'shading'-artifacts as a reason for missing single molecule signals (see section 4.2) within the indicated area (fig. 4.11: white arrows) can be excluded. Therefore, this example clearly demonstrates the advantage of combining a SMLM-data set with an 3D-SIM-image stack of the same region of interest.

A 2-color 3D-SIM and 2D-SMLM image data set recorded with the new 'Combo'-setup is illustrated in figures 4.13 and 4.14. For the first time, synpo (red, Alexa 647), an actin-binding protein associated with the cisternal organelle (CO), is visualized within the AIS

of retinal ganglion cells. So far, the existence of the CO in retinal ganglion cell AIS had not been shown. AIS were also labeled for ankG (green, Alexa 568). Widefield images acquired with transmitted light are illustrated for the two color channels including an overlay (fig. 4.13 A I-III). In order to demonstrate the resolution improvement gained with SIM- and SMLM-mode (fig. 4.13 SIM: C I-III and SMLM: D I-III), conventional fluorescence widefield images as the sum of three raw SIM-images with changing phase are depicted as well (fig. 4.13 B I-III). A co-localization of AIS and CO is clearly observable. However, the 3D-information is not apparent. A 'striped' pattern can be observed within the background of the 568 nm channel (fig. 4.13: C-II and III, white arrows). This pattern is not an artifact due to SIM-reconstruction, but depicting a fluorescent signal of a vertically arranged AIS bundle located in a lower focal layer. Due to a lower z-sectioning of SIM compared to SMLM, this pattern is nearly not observable within the SMLM visualization. Figure 4.14 and 4.15 show a 3D-SIM-stack of both color channels including a 2D-SMLM-image of each color and rotated in all spatial dimensions, which enables to extract 3D-information. For SIM-reconstruction, a pixel-sorting based deconvolution algorithm has been applied, which enhances z-sectioning and suppresses noise sources resulting in higher image quality.⁵⁶ However, an even superior depiction can be achieved applying 3D-SMLM on the specimen, which is planned for future experiments.

In some cases, the AIS appeared as if tilted helically around its longitudinal axis as shown in figure 4.16. β -IV-spectrin connects the inner axonal cytoskeleton with the ankG - ion channel complex in the membrane as illustrated in the schematic (from Rasband *et al.*²¹). The super-resolved SMLM-image, which is a cross section of the AIS, is able to resolve the actual distribution of β -IV-spectrin in its membrane-associated pattern with clear elongations pointing towards the inner actin cytoskeleton of the axon (fig. 4.16 magnification: white arrows).

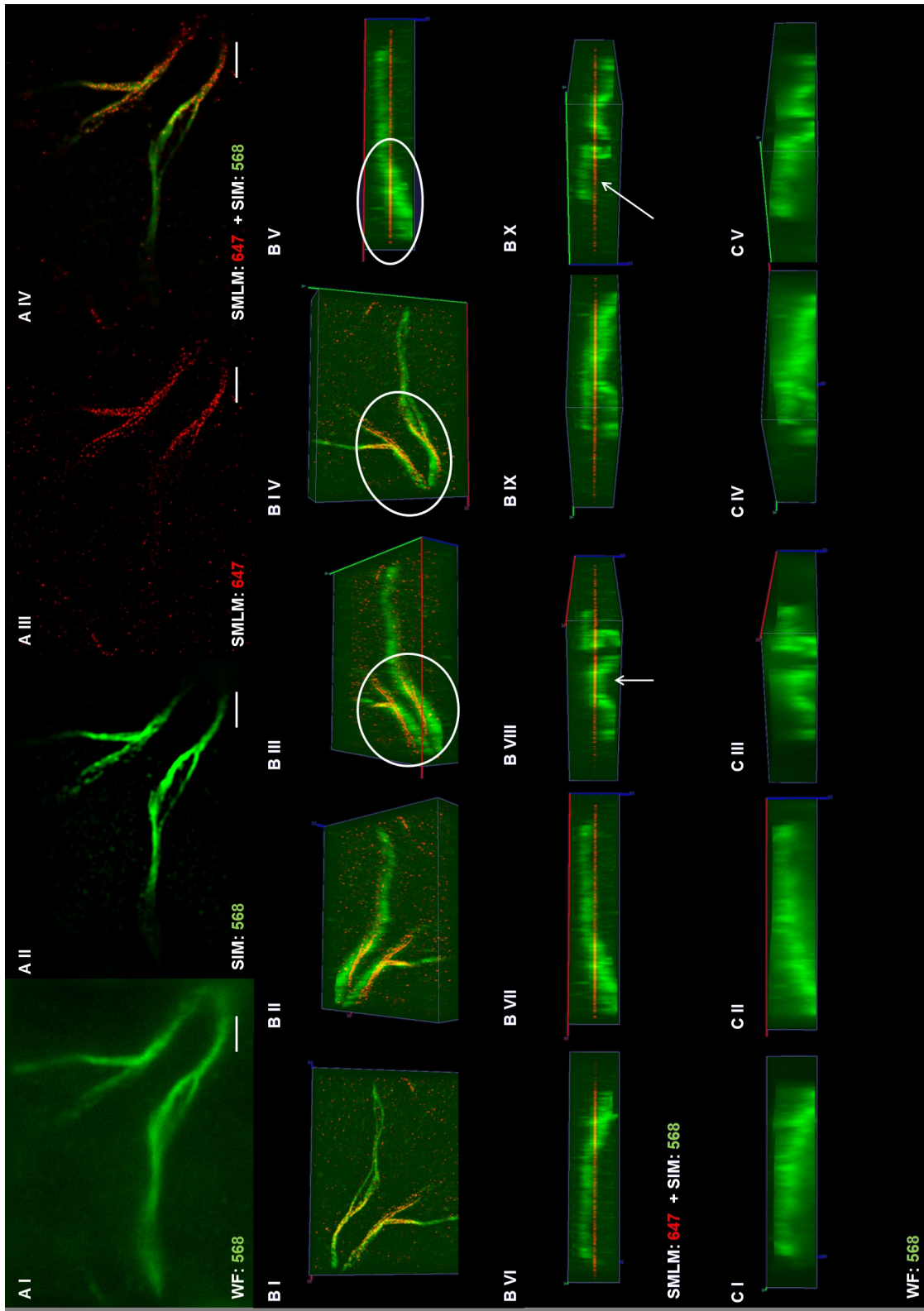


Figure 4.11: 'Proof of principle' of imaging with the 'Combo'-microscope: 3D-SIM (green) and SMLM (red) data set of the same axon initial segment labeled for β -IV-spectrin (Alexa 568) of a retinal ganglion cell. **A I**: Standard widefield fluorescence image. **A II**: Structured illumination microscopy (SIM) image. **A III**: Single molecule localization microscopy (SMLM) image (Visualization: Triangulation). **A IV**: Overlay SIM and SMLM image. **B I-V**: Rotated 3D-images of overlay SIM and SMLM: z-sectioning of SMLM is superior to SIM as only SMLM signals can be filtered more easily (white circles). SIM-images show the complete AIS, whereas the SMLM-image only depicts a certain focal area. **B IV-X**: Rotated (z) 3D-images of overlay SIM and SMLM data set: The AIS turns across its dimensions (white arrows). **C I-V**: Rotated (z) 3D-images of widefield-data set: Wriggling of the AIS can not be resolved (excitation: 568 nm; pixelsize: 32.25 nm; scalebar: 2 μ m).

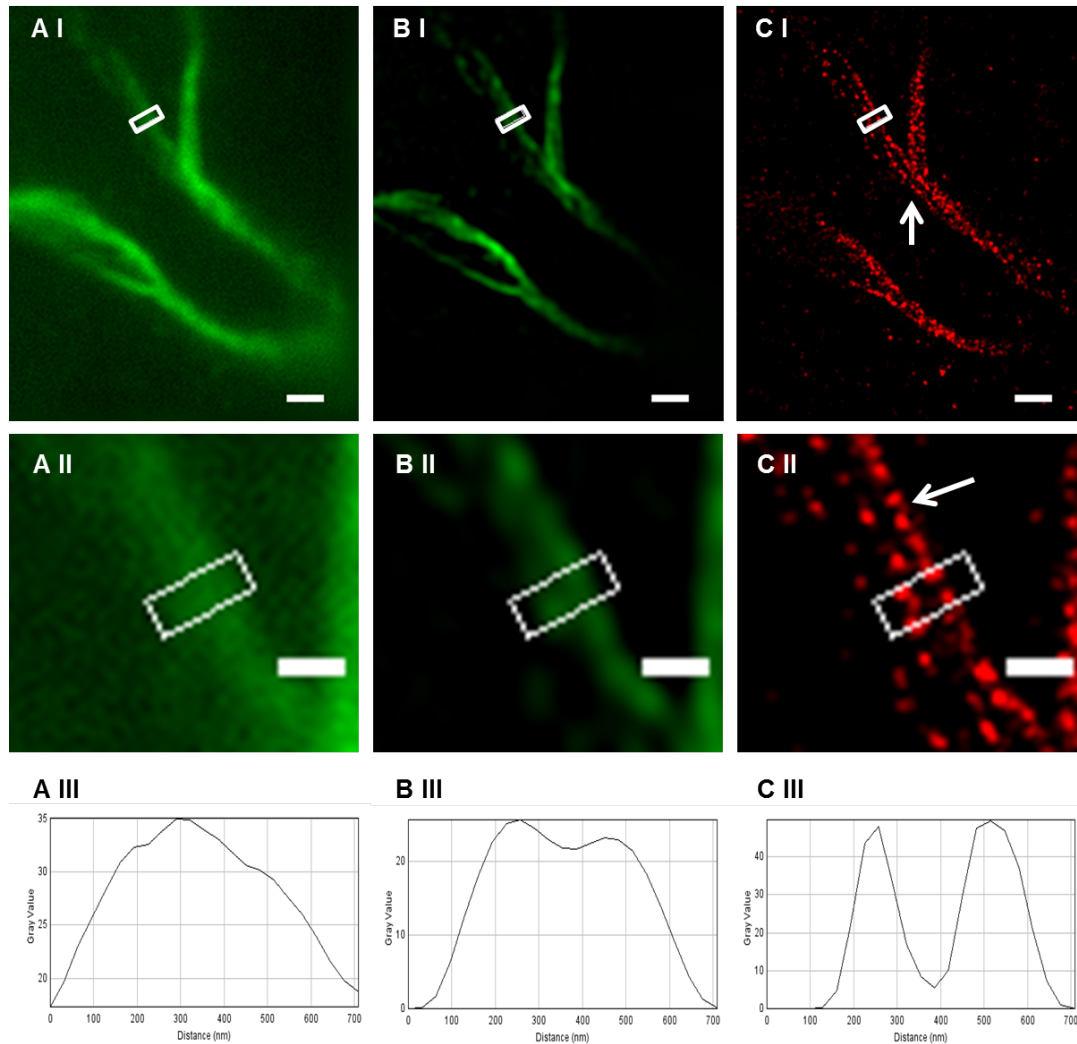


Figure 4.12: Resolution and information improvement gained with the 'Combo'-setup: 3D-SIM (green) and SMLM (red) data set of the same axon initial segment labeled for β -IV-spectrin (Alexa 568) of a retinal ganglion cell as in figure 4.11. The same region of interest was imaged using three different methods. **A-I**: Conventional widefield fluorescence image. **B-I**: Structured illumination microscopy (SIM) image. **C-I**: Single molecule localization microscopy (SMLM) image (Visualization: Triangulation). For illustration purposes, intensity profiles are plotted across the AIS of the ganglion cell (white frame). **A:II-C:II**: Magnified region of interest for all three acquisition modes. **A:III-C:III**: Intensity profiles across the AIS for the selected area and extracted for each acquisition mode (distance [nm] vs. intensity [a.u.]; excitation: 568 nm; pixelsize: 32.25 nm; scalebar: 1 μ m, scalebar magnification: 500 nm).

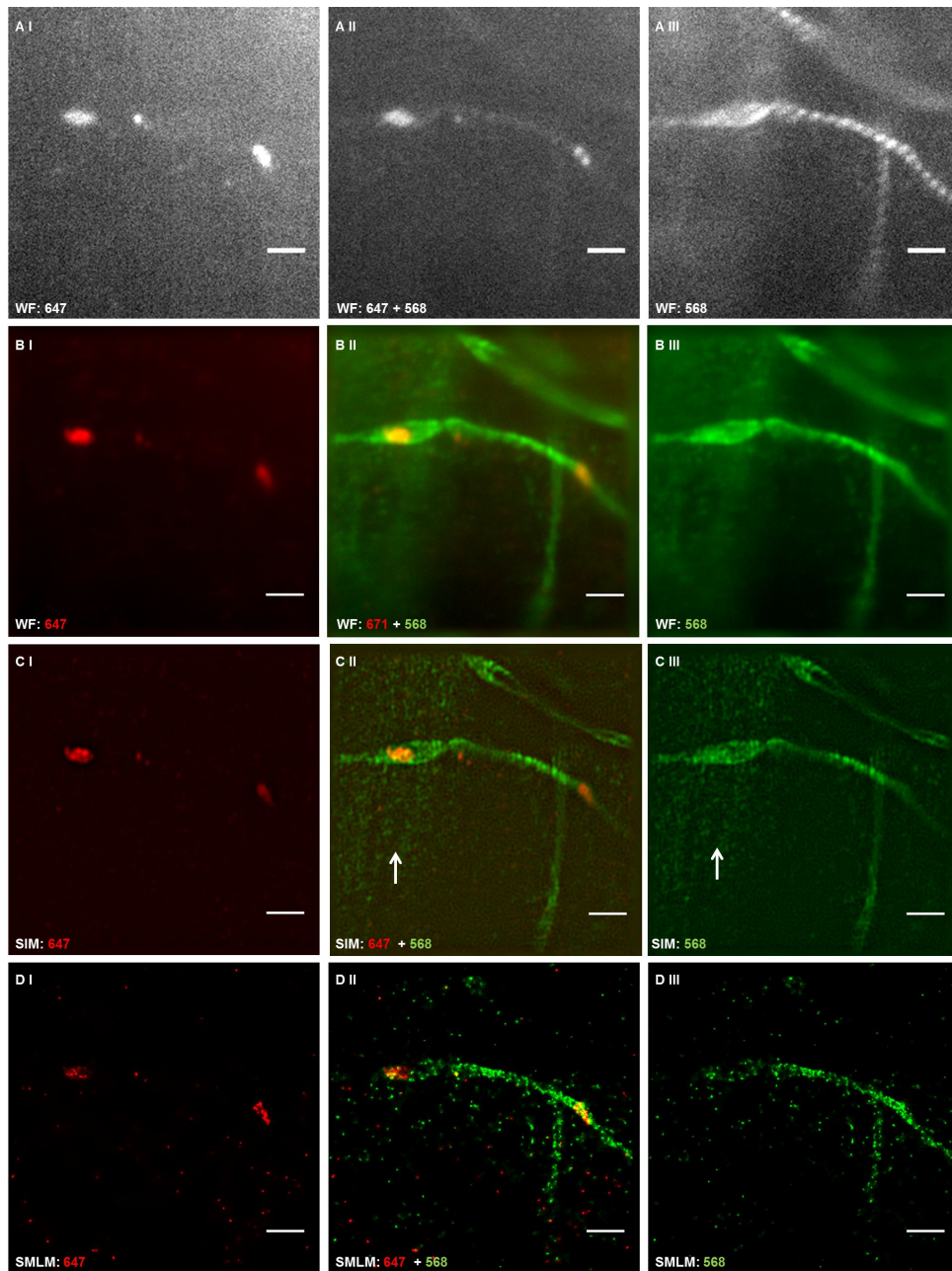


Figure 4.13: Illustration of 2-color-2D-'Combo'-microscope: Two color SIM and SMLM data set of the same axon initial segment (AIS) of a retinal ganglion cell. AIS was labeled for ankyrin-G (ankG, green, Alexa 568) and cisternal organelles (CO) associated with the AIS was labeled for synaptopodin (synpo, red, Alexa 647) **A I**: Widefield image synpo. **A II**: Widefield image AIS and synpo (dichromatic and blocking filter: 671). **A III**: Widefield image AIS (sinusoidal illumination visible). **B I-III**: Widefield images: Sum of three raw SIM-images with shifted phases. **C I**: SIM image synpo. **C II**: Overlay SIM images. **C III**: SIM image AIS. **D I**: SMLM image synpo. **D II**: Overlay SMLM images. **D III**: SIM image AIS (visualization SMLM: Triangulation; reconstruction SIM: conventional frequency space based reconstruction; excitation red channel: 671 nm; excitation green channel: 568 nm; pixelsize: 32.25 nm; scalebar: 2 μ m).

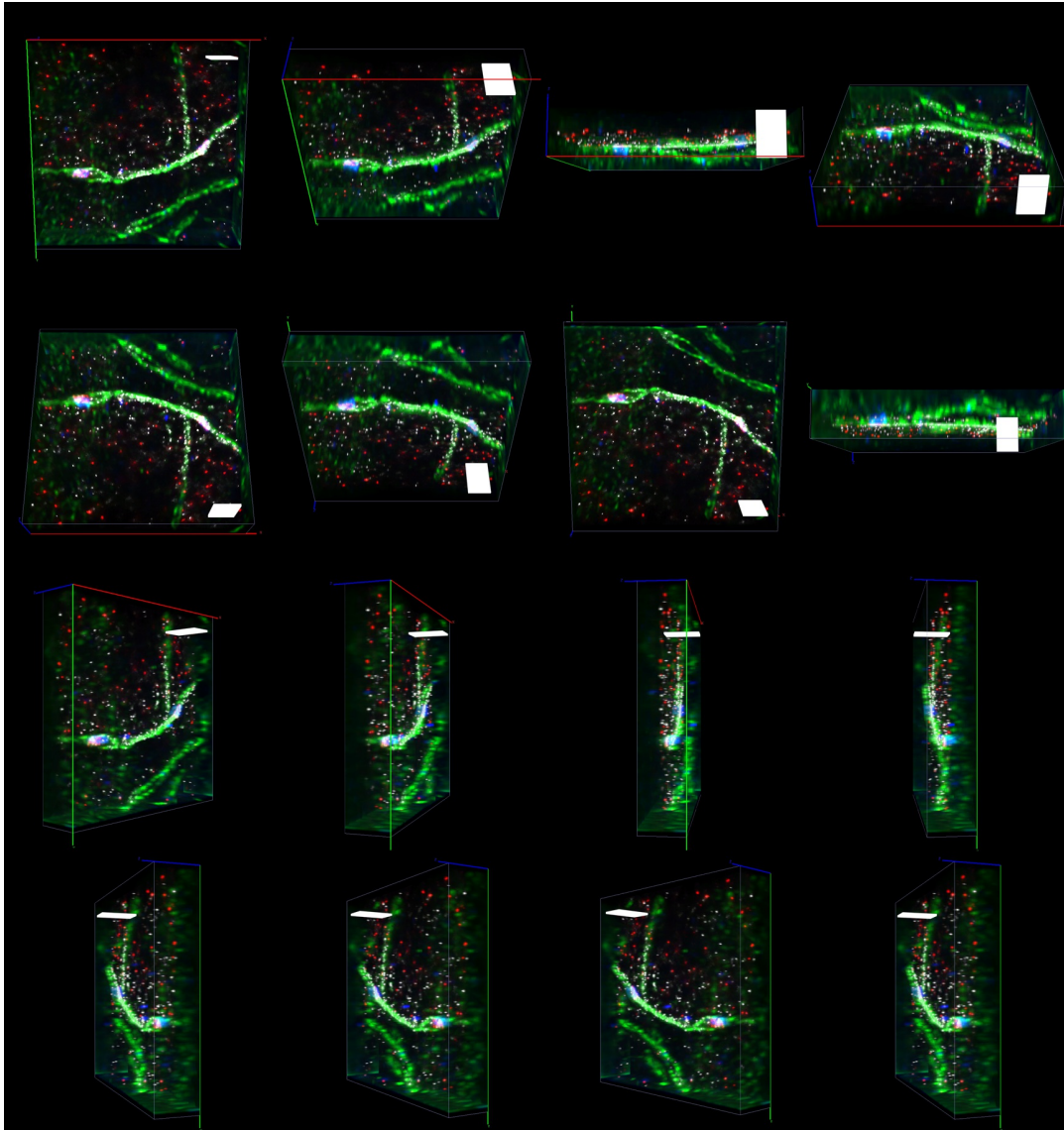


Figure 4.14: *3D-Visualization of 2-color-3D-SIM-2D-SMLM-imaging with the 'Combo'-microscope: 2-color-3D-SIM and 2D-SMLM data set of the same axon initial segment (AIS) and the AIS-associated cisternal organelles (CO) of a retinal ganglion cell as shown in figure 4.13. AIS was labeled for ankyrin-G (ankG, Alexa 568) and CO for synaptopodin (synpo, Alexa 647). SIM: green (ankG) and blue (synpo). SMLM: white (AnkG) and red (Synpo) (visualization SMLM: Triangulation; reconstruction SIM: pixel-sorting based deconvolution in position space; excitation blue/red color channel: 671 nm; excitation green/white color channel: 568 nm; pixelsize: 32.25 nm; scalebar: 2 μm (x/y) and 3.2 μm (z)).*

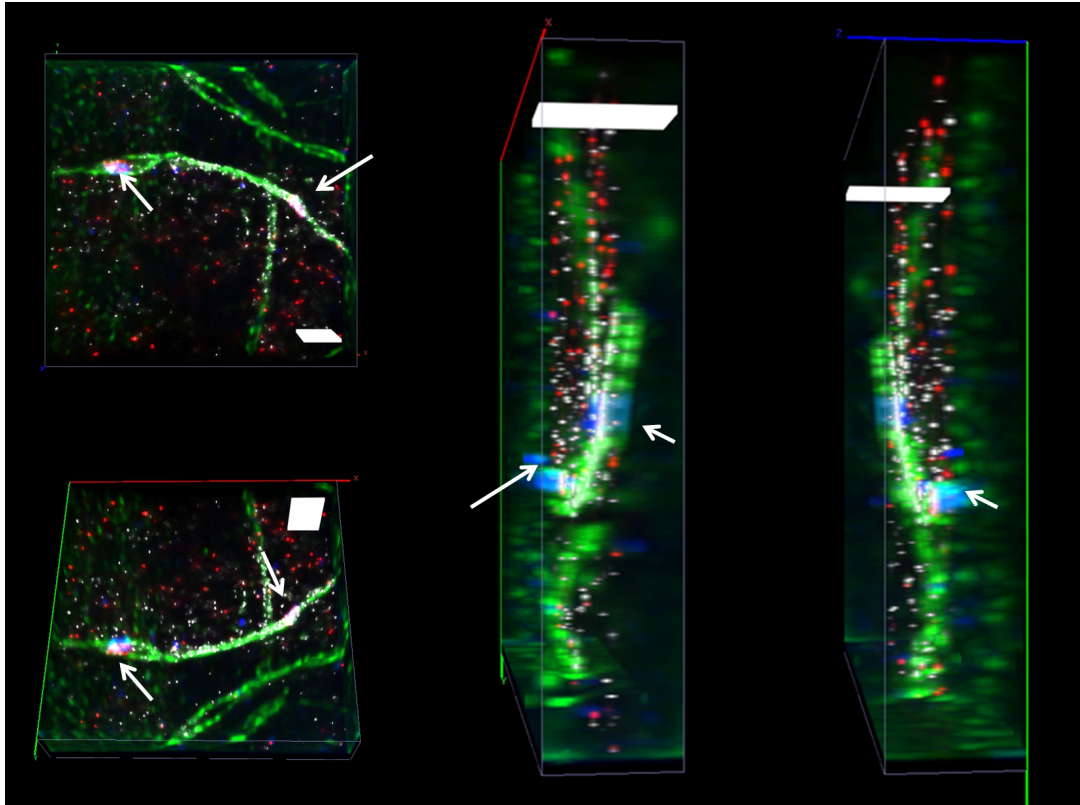


Figure 4.15: *3D-Visualization of 2-color-3D-SIM-2D-SMLM-imaging with the 'Combo'-microscope: 2-color-3D-SIM and 2D-SMLM data set of the same axon initial segment (AIS) and the AIS-associated cisternal organelles (CO) of a retinal ganglion cell as shown in figure 4.13. AIS was labeled for ankyrin-G (ankG, Alexa 568) and CO for synaptopodin (synpo, Alexa 647). SIM: green (ankG) and blue (synpo). SMLM: white (AnkG) and red (Synpo). Synpo labeling in both microscope modes can be identified within AIS (white arrows; visualization SMLM: Triangulation; reconstruction SIM: pixel-sorting based deconvolution in position space; excitation blue/red color channel: 671 nm; excitation green/white color channel: 568 nm; pixelsize: 32.25 nm; scalebar: 2 μm (x/y) and 3.2 μm (z)).*

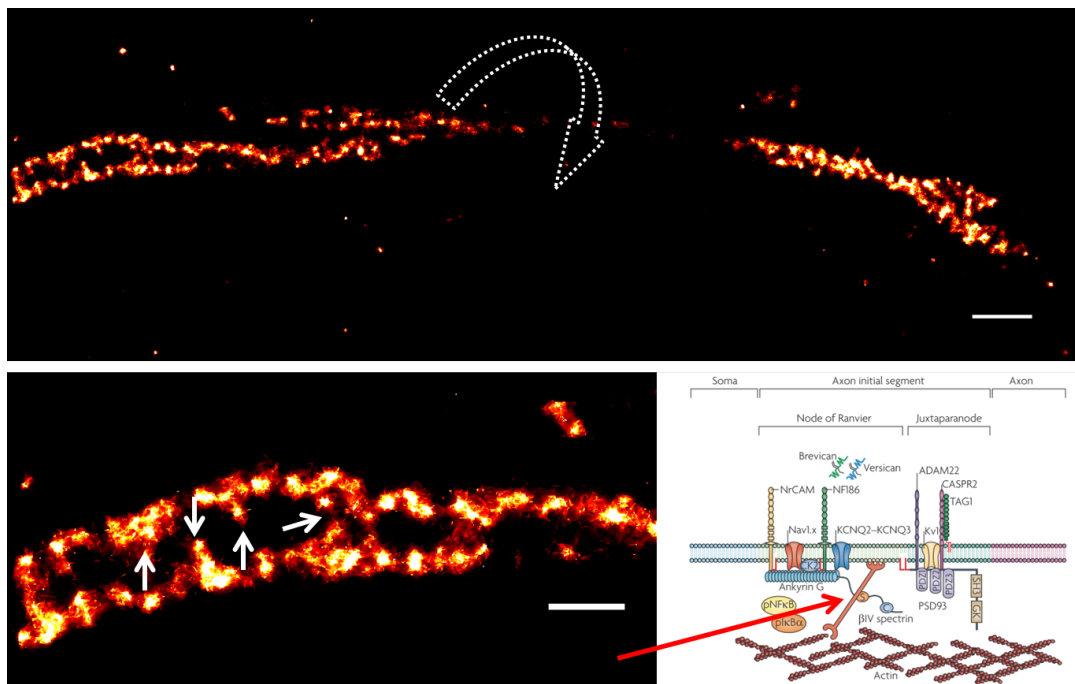


Figure 4.16: SMLM image of an axon initial segment (AIS) labeled for β -IV-spectrin (Alexa 568) of a retinal ganglion cell. The AIS appears helical or twisted around its own axis. Spectrin-similar invaginations into the inside of the AIS can be observed (magnification), which is in concordance to published data as illustrated within the schematic. Schematic modified from Rasband et al.²¹ (visualization SMLM: Triangulation; excitation: 568 nm; pixelsize: 5 nm; scalebar: 1 μ m; scalebar magnification: 500 nm).

4.4 Live-cell experiments with the 'Combo'-Setup

In literature, the RPE is described as a strong phagocytosing tissue.^{90,91} The phagocytosis of artificial sphericals (beads) by RPE-cells *in vitro* have been reported either imaged with electron microscopy¹³⁶ or by applying conventional fluorescence microscopy.¹³⁷ Before starting to test pharmaceutical uptake of RPE-cells, the possibility of applying SIM-imaging to RPE-cells was tested including a time-resolved study. Moreover, to demonstrate the possibility of a time-resolved visualization of phagocytotic activity using the 'Combo'-setup, cells *in vitro* were fed with artificial beads.

Phagocytosis of beads by donor RPE-cells

Repeatedly imaging of RPE-cells with SIM over hours or even few days using low laser intensities (Watt range) did not show any obvious harmful influences on the health of the living RPE-cells. A time-resolved study of living cells can be easily conducted by exploiting the SIM-mode as exemplarily shown in figure 4.17. The new position saving and relocation routine is demonstrated for repeated imaging of a prominent cell configuration (two cell nuclei). In order to ensure cells were relocated correctly an image in transmitted mode was conducted prior to each SIM-imaging process (fig. 4.17 A-I and B-I). The transmitted mode reveals more LF- and MLF-granules as this method does not provide any z-sectioning. SIM-imaging of the same cell was conducted by exploiting the AF-signal of the granules. Additional specific labellings were not used at that stage. One color channel can be quite sufficiently resolved though granules within RPE-cells tend to move during acquisition ('vibrations'). An overlay between the two color channels used for excitation (488 nm and 568 nm) already reveals granules movement as exemplarily demonstrated in figure 4.17 A-II (white arrow, magnification). In contrary, the same granule appears well overlaid in both color channels, when imaged after two hours (4.17 B-II, blue arrow, magnification). Thus, two excitation channels for a time-resolved study may already introduce artifacts due to moving of the specimen, which needs to be considered for following experiments. However, it is possible to image and track movement of same LF- and MLF-granules with time-resolved SIM-imaging (red and purple arrows).

In order to demonstrate the potential of imaging the phagocytotic activity of RPE-cells with the 'Combo'-setup, cells were exposed to fluorescent beads (200 nm) one day prior to imaging (fig. 4.18). Cells were imaged by exploiting again the AF-characteristics of LF- (purple arrow) and MLF-granules (blue arrow) with 2-color-3D-SIM. Cell borders were determined by a prior acquired image with transmitted light (not shown in figure). Beads are only excitable with the 488 nm laser line, whereas LF- and MLF-granules are excitable over a wide range in the visible spectrum as demonstrated in prior sections. Therefore,

a well defined separation of the bead signal from the granules signal can be conducted. For few granules a temporal shift between both sequentially recorded color channels was observable (red arrow). A 3D-visualization of the magnification clearly illustrates bead uptake into the cell, as beads are located within the same focal areas as LF- and MLF-granules (fig. 4.18 B I-V). Moreover, movement of single beads can be clearly tracked with the 3D-depiction. Elongated PSFs of beads in z-direction indicate no movement during SIM-acquisition, whereas a diagonal arranged resulting 3D-PSF clearly depicts movement of beads during image acquisition.

Phagocytosis of VEGF inhibitor by ARPE-19 cell line

The ARPE-19 cells are a standardize cell-line, which does not contain any LF- or MLF-granules and therefore no AF-signal. In order to prevent a spectral crosstalk between labeled pharmaceuticals this cell-line was chosen for the VEGF inhibitor experiments. However, dimensions of cells needed to be labeled in order to visualize a potential pharmaceutical uptake within the cell. Membrane and nucleus marker were chosen as described in section 3.3.3. Applying high laser-intensities (kWatt range) generally necessary for SMLM-imaging was only possible once. Several imaging cycles were not possible as high energies are absorbed by cells causing cell-death.

A publication describing 6S-IDCC and 6S-ICC (both Mivenion, see section 3.4.3) as a dye used for SMLM-imaging was not found. Both dyes exhibit good photo-switching behavior, when tested without being attached to any specific target protein within a specimen. Oxygen scavenging embedding media,⁴³ which additionally contained reducing agents⁵⁹ produced best results for 6S-IDCC in terms of photo-switching efficiency and stability. Photo-switching characteristics of 6S-IDCC were comparable to Cy5 or Alexa 647 dyes. Photo-switching characteristics of 6S-ICC were similar to Cy3 or Alexa 568 and remained satisfactory when imaged in water or PBS-based media, the latter of which may be favorable for live-cell experiments. Unfortunately, the 6S-ICC spectrally overlaps with the membrane and nucleus marker GFP and RFP. As no suitable far-red membrane or nucleus marker was found, the 6S-IDCC dye was selected for Bevacizumab labeling, which guaranteed satisfying spectral separation of the three channels. Hence, photo-switching of 6S-IDCC is enhanced by oxygen scavenger and reducing agents, switching buffer are added to the cell-culture. However, switching buffer remains toxic for cells. A 3D-SIM visualization of nucleus and membrane of the RPE-cells was successfully conducted (data not shown). The visualization of Bevacizumab molecules or clusters remained challenging. However, very first results of Bevacizumab (Avastin) uptake within standard ARPE-19 cells *in vitro* visualized in 3D-SIM images are discussed in section 6.

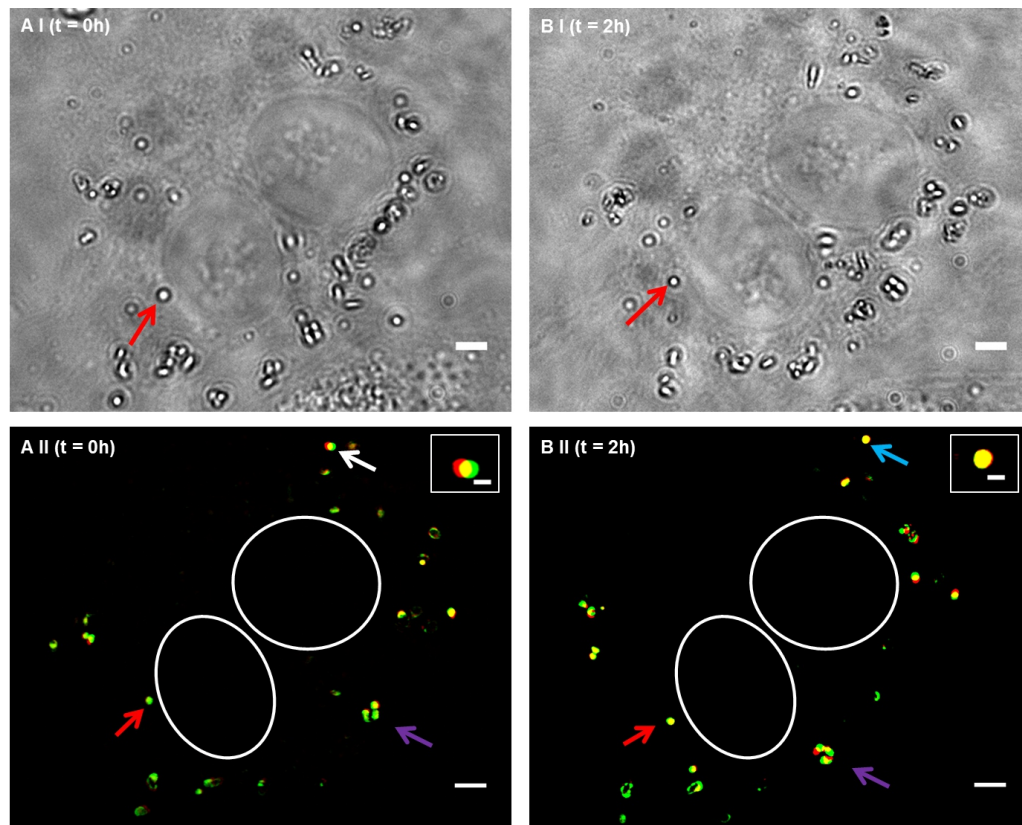


Figure 4.17: *Time-resolved study of retinal pigment epithelium (RPE) cells: RPE-cells were imaged and spatial positions saved applying a new developed routine including an automated relocation of cells. A-I: Two RPE-cells imaged with transmitted light at $t=0h$. A-II: 2-color-SIM-image of the same cells at $t=0h$. Cell nuclei positions are indicated by white circles derived from images A-I and B-I. Autofluorescent (AF) signals emitted by lipofuscin (LF) and melanolipofuscin (MLF) were exploited for imaging. The magnification indicates granules movement already at small time-scales as a shift is already visible between two sequentially recorded color-channels (white arrow). B-I: Same RPE-cells relocated and imaged with transmitted light at $t=2h$. B-II: Same RPE-cells relocated and imaged with 2-color-SIM-mode at $t=2h$. The magnification of the same LF-granule shows no granule movement (blue arrow). Same LF- and MLF-granules (red and purple arrows) can be detected with time-resolved SIM-imaging (excitation red channel: 488 nm; excitation green channel: 568 nm; pixelsize: 32.25 nm; scalebar: 2 μ m, scalebar magnification: 500 nm).*

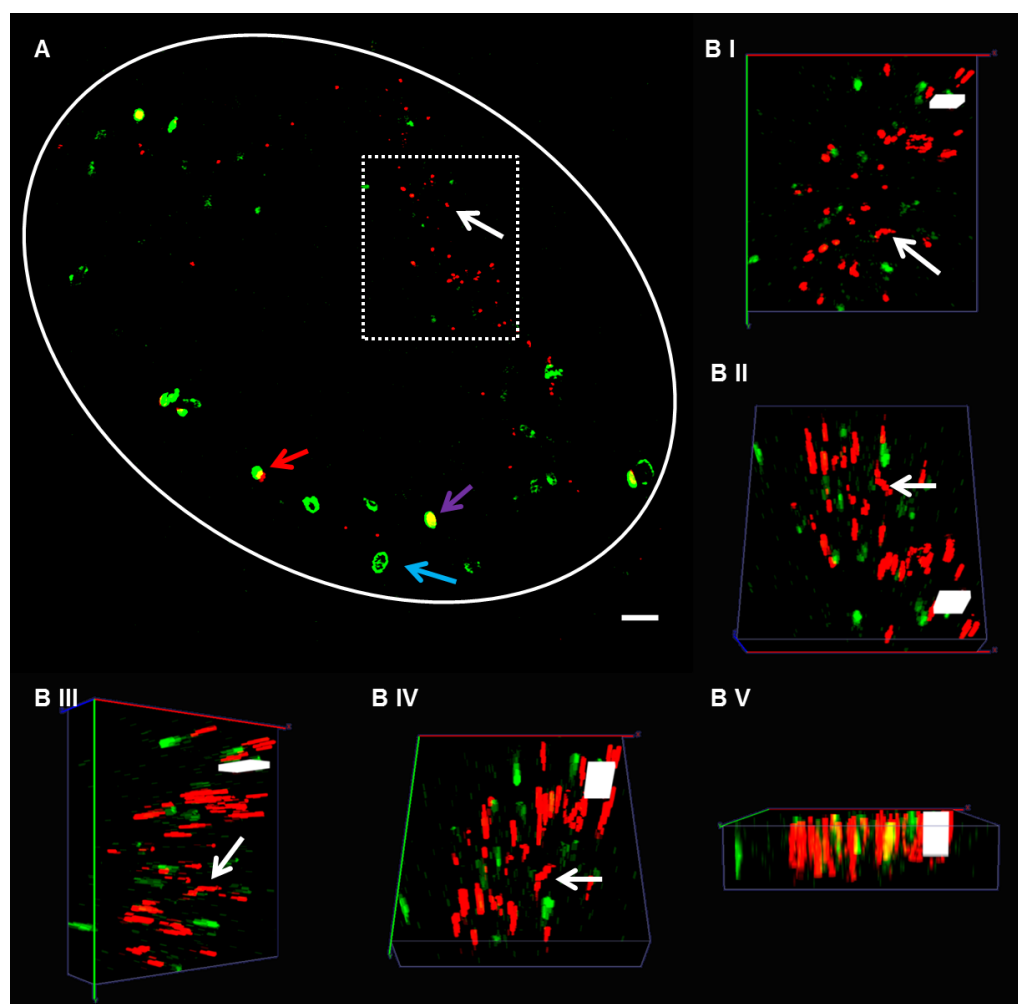


Figure 4.18: Phagocytosis of 200 nm beads by retinal pigment epithelium (RPE) cells. Cells were fed with beads one day prior to imaging. **A**: RPE-cell imaged with 2-color-3D-SIM. Autofluorescent (AF) signal emitted by lipofuscin (LF, purple arrow) and melanolipofuscin (MLF, blue arrow) were exploited for imaging. However, a temporal shift between the two sequentially recorded color channels is in some granules visible (red arrow). Cell borders were determined by a prior acquired image using transmitted light (not shown). Beads are only excitable with the 488 nm laser line and therefore appear only in the red color channel. The magnification is visualized in 3D-SIM in **B I-V**: The stack consists only of 6 focal layers for better visualization. Beads are clearly located with the cell as beads and LF- and MLF-granules occupy same focal layers. Elongated PSFs of beads in z-direction indicate no movement during SIM-acquisition. However, other beads have moved (white arrows) indicated by a diagonal arranged resulting 3D-PSF (excitation red channel: 488 nm; excitation green channel: 568 nm; pixelsize: 32.25 nm; scalebar: 2 μm , scalebar magnification: 1 μm (x/y) and 1.8 μm (z)).

5.1 Autofluorescence Study of Drusen using SIM

5.1.1 Autofluorescent Particles within Drusen

The pathogenesis of drusen, a major risk factor for AMD, is still not completely understood. Drusen have been classified as hard and soft drusen and consist of several components mainly identified by immunohistological studies.¹⁷ Observing soft drusen smaller than $63\ \mu\text{m}$ is not in agreement with the general assumption, however, the results presented here matches with the results presented by Rudolf *et al.*,¹⁸ who also reported similar median sizes for hard and soft drusen. Earlier, Hageman and Mullins had already suggested that a 'strict relationship between size and shape' does not exist.²⁶ However, the range covered by soft drusen is still much larger (maximum size found: 130 nm) as expected. It is possible that a single section from each donor (as used in this study) is not representative of all drusen in the whole eye, however, the section was chosen such that the averaged properties of the drusen measured should reflect the drusen population.

Intracellular material, such as organelles and fragments presumably originating from RPE cells has been described within drusen and basal laminar deposits.^{17,28,114,138} While some studies report such structures as coincidental findings,^{16,17,26} Rudolf *et al.*¹⁸ found pigment granules within drusen in at a significant frequency of 6.4% - 8.9%. However, little is known about frequency, shape and fluorescent properties of structures embedded in drusen.

The main advantage of the resolution improvement achieved with SIM emerges when analyzing the morphology of AF particles. Here, more detailed analyses are possible compared with standard widefield microscopy. Using standard widefield microscopy, 79 drusen that contained AF-material were detected (17.9% of all drusen), whereas 101 drusen with AF-

particles were found using SIM (22.7% of all drusen). AF-particles were present in near equal proportions in hard and soft drusen, supporting the idea that drusen shape is not important for the presence of AF-structures. In contrast, drusen size appeared to be important, where drusen with diameters smaller than 63 nm comprised 90% of all drusen that contained AF-particles. AF-intensity measurements and comparison of intensity ratios at different wavelengths suggested that AF-material in drusen resembles LF granules of the RPE. The similarity in intensity ratio between AF-particles and LF-granules suggest that they are composed of the same material though no whole emission spectrum was available. As intensity profiles of AF-particles were always compared with RPE-LF granules within cells overlaying the druse (on the same section), possible changes by the fixation process on the AF-characteristics will have affected same materials in the same manner. Thus, a misinterpretation of the spectral signals can be excluded as AF-particles were always compared with RPE-LF granules in the proximate vicinity.

AF-particle intensity profiles showed a stronger fluorescence for 488 nm compared with 568 nm excitation as expected for LF granules. Furthermore, the AF-particles in drusen generally appeared round-shaped as RPE-LF granules and were well circumscribed with no signs of dissociation.

A detailed analysis of particle sizes yielded a diameter of 702 ± 297 nm. This value is slightly smaller than the typical size of LF-granules within RPE cells, which have previously been evaluated by Boulton *et al.*¹³⁹, who demonstrated LF-granules were between 1 – 3 μ m in diameter when examined with electron transmission microscopy. However, a recent report by Biesemeier *et al.*¹⁴⁰ suggested that granules are 1.5 x 0.5 μ m, although they did not distinguish between LF, melanin and melanolipofuscin (MLF). We observed that almost one-third (30.2%) of AF-particles were even smaller than 500 nm. This 500 nm threshold is an arbitrarily selected value in this study and far below the previously reported granule sizes in literature. This emphasises the advantage of SIM. SIM is especially useful for the detection of such small particles and low autofluorescence signals. It has to be mentioned that some granules have been observed marginal to the section's thickness. A shortcoming of measuring structures on histological sections generally is that sections are only of a certain thickness, which may result in cropped structures at the edges.

It has been postulated that inflammatory, cell-mediated and immune processes might initiate drusen formation^{16,17}. Injuries of the RPE caused by various events (gene mutation, light damage, oxidative stress, LF accumulation)¹⁷ are assumed to result in a release and accumulation of cell debris between BM and RPE.¹⁴¹ Recently, Johnson *et al.*¹⁴² have shown that even cultured RPE cells secrete several membrane-bounded and non-membrane-bounded deposits which are also found in drusen. Besides this, material originating from the RPE, choroid and plasma proteins related to inflammatory processes have been reported within drusen,^{17,143} which supports the idea that drusen biosynthesis

is a response to local inflammatory events.¹⁴⁴ Moreover electron micrograph images of 'vacuoles' containing LF located within the RPE monolayer were interpreted by Anderson *et al.*¹⁶ as degenerated RPE cells and the first stage of forming a druse.

As drusen have been identified to contain lysosomal material, observing very small granules within drusen (< 500 nm) could display early stages of catabolic lysosomal processes of RPE cell material within drusen resulting in LF-like deposits.¹⁴⁵ Alternatively, lysosomal-LF granules secreted from RPE cells might undergo further catabolic degradation processes resulting in smaller LF particles than originally exocytosed.

We mainly detected these LF granules within small drusen (< 63 nm), which might indicate this aforementioned process of LF appearance only in early stages of drusen formation. In large drusen, LF granules are presumably completely catabolised. However, the AF-characteristic must get lost during the suggested catabolic processes, as no fragments in the near vicinity of a granule were observable. It has to be mentioned that though AF-particles were mainly detected within small drusen, no correlation between drusen volume and AF-particle volume was observed.

Furthermore, nearly all AF-LF granules (83.1 %) have been found in the outer two-third of the druse. This also might hint at secretion of AF-deposits in early stages of drusen formation. Or it indicates the time-consuming process of LF-like granules formulation within a druse while further excretion of RPE cell material is ongoing.

The data presented in this study is in concordance with the hypotheses of drusen originating partly from RPE cell material. SIM has proved to be a useful tool for analyzing AF-particles at a resolution level, which is much better than standard fluorescence microscopy and therefore provides better insights in drusen formation.

5.1.2 Autofluorescent 'ring-like' Structures within Drusen

A study reporting melanolipofuscin (MLF) granules within drusen could not be found in literature. The main characteristic of MLF is a dark (non-fluorescent) core surrounded by a strong AF-ring. Ring-like AF-structures also possessing a dark (non-fluorescent) core (most likely melanin) surrounded by a AF-ring with inhomogeneous intensity distribution were observed in several drusen during this study, though only in one case a structure similar to MLF is observed within a very small drusen. Typically ring-like AF-structures in this study were elongated along one axis ('cigar'-shaped) and often unclosed. Based on a comparison between AF-spectra of LF- and MLF-granules with the spectra of ring-like AF-structures, it is highly suggestive that the surrounding border consists of fluorescent dyes, which are similar to those located in LF- and MLF-granules. Moreover, no other AF-objects within have been reported within the macular yet. As demonstrated, in few cases these AF-structures are even observed beyond BM. Reports describing a similar

observation could not be found as well.

The same question about origin of ring-like AF-structures occur as well. Two possible scenarios can be thought of: Firstly ring-like structures were originally MLF granules. Sizes of the ring-like structures ($1240 \text{ nm} \pm 80 \text{ nm}$) and spectral characteristics are similar to the median size of MLF within RPE cells reported lately ($1097 \pm 110 \text{ nm}$)⁸⁸ taking the largest axis into account. However, due to the observation, that structures are often unclosed, objects are enlarged essentially. Similar to the considerations of the origin of AF-particles within drusen, ring-like AF-structures might have been MLF, which are catabolized during drusen-formation or are the result of secretion of RPE-material into the underlying druse. Details for this hypothesis can be found in the prior section (4.1).

5.2 The developed 'Combo' - Microscope

The developed 'Combo'-microscope setup combines the two high resolution methods SIM (Structured Illumination Microscopy) and SPDMPHymod (a method based on Single Molecule Localization Microscopy, SMLM) in one custom setup. The setup is also capable of PALM and STORM/dSTORM-imaging. Both imaging methods can be conducted with the same physical setup, which simplifies image acquisition significantly and is more over extremely time-saving. In contrast to presently available commercial microscope systems the setup is equipped with up to five different excitation channels for each microscope-mode and illumination pattern are generated with an adjustable interferometric unit.

5.2.1 Application and Benefits

In particular sparsely labeled structures will benefit from performing imaging with two high-resolution methods combined in one physical setup. As visualization algorithms used in SMLM-imaging require a reasonable density of spatial positions, the mathematical generation of structural information from a single molecule data set is still highly challenging or even impossible if the total number of events is too low. In this case, applied visualization algorithms are generally not able to reveal any structural and spatial information, which is a crucial requirement in life-science. A second label of correlated structures could help to resolve spatial information about the sparsely labeled target and thus provide an orientation within the specimen.⁶⁴ Nevertheless, single molecule event densities are not only dependent on the effective labeling density, but also on embedding-media, bleaching and blinking-efficiency, which can negatively influence SMLM-acquisition as prior discussed. Though the structure within the specimen is well labeled, the SMLM-data set might not be able to reveal the underlying structure. A high-resolved SIM-image recorded prior to the SMLM-imaging process of the same structure may close the information gap,

due to its different contrast mechanisms. To summarize, the 'Combo'-setup delivers a high-resolved image of the specimen acquired with SIM-mode providing necessary structural information for 3D-orientation. The structural information can be correlated with the sparse target distribution gained with SMLM-mode.

A second potential application, which will greatly benefit from the combination of sequential SIM- and SMLM-imaging will affect biological questions dealing with autofluorescent (AF) structures. As already demonstrated, SIM is a useful tool to study AF-structures generally found in the aging human eye.^{32,88} However, if additional fluorescence markers are used to mark specific structures, the influence of the AF-signal on the specific signal of the markers during the imaging process with SIM and SMLM needs to be studied. When utilizing SIM, the ratio of the AF-signal intensity versus the intensity emitted by additional fluorescent markers will be of main interest. SMLM will be more challenging as the AF-signal might outshine the single molecule signal, which is presumably much weaker. In future measurements, it needs to be tested whether it is possible to separate the single molecule signal from the AF-signal in order to reconstruct an image. As the AF is generally strongest in the shorter wavelength band (e.g. AF of lipofuscin in RPE-cells^{32,88} and AF-background due to fixation such as PFA¹⁴⁶), additional markers within the red or near-infrared range might be most promising in order to separate signals from each other.^{39,51}

Finally, the AF-signal given by the SIM image and its structural information can be merged with the SMLM-position data of specifically labeled target in one image. As a result, the relative spatial orientation to each other is revealed and can be assigned to separate compartments within the biological object. In other applications it might be impossible to distinguish between AF-signal and labeling. Here, SMLM would reveal the AF-signal as it is generally hardly 'blinking', when AF-fluorophores are packed in very high densities e.g. in lipofuscin or melanolipofuscin granules. Thus the AF-signal itself could be imaged with SIM and correlated with the SMLM data. However, there are reports referring to a blinking of densely 'packed' AF-structures, though details about the photo-switching capability are not described.³⁹ In other cases sufficient photo-switching of AF-structures was exploited for SMLM-imaging.¹⁴⁷ In this case the cross-talk of the emission spectrum of the AF-signal compared to the specific labeling are of interest. Well separated spectra would enable sequential SMLM-imaging. However, in practice AF-signals tend to cover a broad range of the visible spectrum making it difficult to separate single molecule signals. A prior acquired high-resolved SIM-image can help to solve this challenge as well.

Besides these application a combinations of 'switchable' and 'non-switchable' fluorophores will extend the total number of channels available for high resolution fluorescence imaging.

Moreover, the setup can easily be extended with multiple cameras in order to image different spectral emission signals simultaneously similar to the setup presented in Baddeley *et al.*³⁹ This setup splits the fluorescent signal of different populations onto two halves of one CCD-chip. Based on the ratio calculated from the two CCD-halves a spectrally distinction between different fluorophore population is possible. Utilizing two CCD-chips instead of one, each equipped with a separate emission filter-wheel, would easily allow exciting multiple fluorophore population simultaneously with multiple laser-lines. However, instead of long-pass dichromatic beamsplitters a multi-band pass is necessary, which results in a loss of fluorescent signal.

First proof-of-principle images recorded with 3D-SIM-2D-SMLM-mode for two color channels demonstrate that a combination of both methods in one setup allows biological questions to be addressed on a highly advanced resolution level (see discussion 5.3.1). Finally, as the 'Combo'-microscope presented here provides a unique, fast and fully automated imaging device, it is possible to conduct live-cell experiments as exemplarily demonstrated (see discussion 5.3.2).

5.2.2 Revealing Artifacts in SIM- and SMLM-Imaging

A big advantage of combining both methods is the identification of artifacts in SMLM and SIM-images. A standard light/fluorescence microscope delivers an image, which is only convolved with the PSF of the imaging system. However, SIM- and SMLM-images additionally rely on a mathematical reconstruction of the recorded data. Thus no 'real' but artificial images are generated often containing artifacts. As a result the interpretation of SMLM- as well as SIM images is not necessarily straight forward and should be conducted very carefully.

Artifacts due to visualization algorithms applied on SMLM-data have been described in detail in section 4.2. In case of very high labeling densities multiple fluorophores being in a bright state are no rareness especially when detected in early frames of the recording. The intensity distribution of these fluorophores are often located within a diffraction limited area and are therefore discarded ('collision artifacts'). The result is comparable to a sparsely labeled structure, though the underlying structure is well defined. As a result areas of high labeling intensity appear of less molecule density compared to 'collision free' areas and therefore can lead to a misinterpretation of the recorded data. Fluorophores staying in a fluorescent state for several frames are also excluded from the reconstruction and thus the total number of detected events is further reduced. As described applying visualization methods on low single molecule position densities can be highly challenging

or even impossible. It is also possible that algorithms fill gaps between close structures, though a connection is not real. Additionally, high background intensities due to unspecific labeling or AF due to fixation play a key-role resulting in a locally reduced total number of detected single molecule events ('shading artifacts') though the structure is labeled well.

A quite prominent problem is the interpretation of single molecule clusters detected with SMLM, which are difficult to interpret correctly.⁷ Each single molecule event within a cluster does not necessarily represent one labeled protein. More likely a protein is represented by a few events detected. The photochemical characteristics of fluorophores are still relatively insufficiently understood. It is known that fluorophores often undergo several switching cycles before they are photo-bleached, especially when the embedding medium contains oxygen-scavenger and reducing agents.^{43,59} Thus a cluster may represent only one labeled protein. Moreover, labeling is often conducted via antibodies (e.g. commercially available Alexa dyes), which generally have an varying number of fluorophores attached instead of only one. This also leads to multiple detection of the same target molecule and false clustering. Other drawbacks deal with the excitation of the fluorophore itself. Not all fluorophores are contributing to image formation as they are simply not excited due to disadvantageous orientation of their dipole momentum. Moreover, quenching effects and the limited quantum-efficiency of the CCD-chip can also negatively effect fluorescence detection. Misinterpretation of clustering may be avoided by applying appropriate thresholds onto the visualized SMLM-data. However, it remains often difficult to decide whether clustering is real or not. Typically, artifacts due to SMLM-visualization do not occur in a reconstructed SIM-image.

The opposite applies for SIM-images as well. SIM-data is also afflicted with artifacts, which do not occur within SMLM-images. A mathematical description of artifacts occurring during SIM-imaging is outlined and discussed in Schaefer *et al.*⁴⁸ or in the PhD-thesis of Dr. Kai Wicker.⁶ Artifacts due to different bleaching properties of various fluorophores or too high excitation intensities, which bleach the excitation pattern into the object, may result e.g. in a 'striped' image. Artifacts due to the post-processing of the SIM-data could include difficulties in depicting grating period and phase-shift. Additionally, wiener filtering is generally a parameter, which is not easy to handle during SIM-reconstruction. Low resolved noise can be mistaken for structures though they are only an artifact. These artifacts do not occur within the reconstruction of SMLM-data.

Based on the depicted artifacts potentially occurring during image reconstruction a direct comparison between generated images easily reveals artifacts and helps to simplify a correct interpretation of single molecule data. Clustering artifacts in SMLM-images can

be avoided consulting the high-resolved SIM-image and as a result an appropriate threshold for visualization and clustering algorithms can be chosen.¹⁴⁸ With the combination of both methods in one setup and by utilizing multi labeled targets a relatively easy and sufficient solution for this frequently encountered problem is now available. Nevertheless, taking all these mentioned considerations into account 'counting' molecules remains highly challenging though this is often desirable for various biological motivated questions.

5.3 Application of the 'Combo'-microscope

5.3.1 Dual-mode dual-color three-dimensional visualization of AIS in retinal ganglion cells

So far, synaptopodin (synpo) an actin-binding protein associated with the cisternal organelle (CO) of the axon initial segment (AIS), has only been visualized within cortical and hippocampal neurons. A study that describes synpo within the retina or addresses the localization in the AIS of retinal ganglion cells is lacking. Additionally, little is known about the morphology and function of the AIS itself. A super-resolved depiction of the morphology of the AIS is therefore of high interest. Super-resolved co-localization analysis of various proteins associated with the CO could help to understand potential functional and structural interaction between the CO and the AIS, specifically the AIS scaffolding protein ankyrin-G (ankG). The CO is known to be involved in calcium storage and release, and thus a potential interaction with the AIS would give insight into the molecular mechanisms of signal transduction in retinal ganglion cells. Furthermore, a comparison of relative single molecule densities e.g. between healthy and diseased retinal AIS and related proteins could be conducted.

Recently, virtual 'holes' within the AIS at the position of a CO were proposed by King *et al.* within the neocortex of rats by applying 2D-SIM-imaging.¹⁴⁹ Moreover, a correlation of synpo with Kv2.1- and RyR-channels, which are also located in proximity of the CO of neocortical neurons, is suggested. However, no 3D-information is provided in this publication, thus lacking crucial information about the exact CO position in neocortical AIS. It remains unknown whether the CO e.g. is membrane associated or located within the inner AIS. Therefore, this missing 3D-SIM data was obtained utilizing the 'Combo'-microscope. In a first set of experiments, the previously observed 'holes' by King *et al.*,¹⁴⁹ could not be confirmed. Even a super-resolved SMLM image could not confirm this observation. However, to eliminate a very small, yet noticeable crosstalk between the 568 nm and 671 nm color channels, either a dual-color labeling with two strictly separated fluorophores needs to be tested (e.g. Alexa 488 and 647) or a bandpass instead of a longpass filter needs to be used for emission. Moreover, sequential 3D-imaging in both microscope-modes could help

to resolve the morphology of the retinal AIS due to the improved z-sectioning of SMLM compared to SIM-imaging. For this purpose an astigmatism needs to be introduced into the detection-path as explained in previous sections.

Finally, as exemplarily shown in figure 4.16 the AIS of retinal ganglion cells seem to spiral around their longitudinal axis, an observation never made before due to limitation of conventional confocal microscopy.

5.3.2 *In vitro* Experiments: VEGF Inhibitors in AMD-Treatment

Live-cell experiments require a fast imaging process of low photo-toxicity, which is absolutely necessary for preserving cell-health. This requires imaging of the same region of interest over long periods of time as well as an automated relocation of a target, which is now possible with the developed 'Combo'-setup. As exemplarily demonstrated, first attempts showed promising results. For the first time 3D-SIM and time-resolved live-cell imaging of cultured RPE-cells was successfully performed over several hours, where the AF-signal of the LF- and MLF-granules within cells was exploited with no additional labeling necessary. Using low laser intensities, SIM already delivered a sufficient fluorescence signal, which maintained cell health and function and is therefore a much less invasive imaging tool compared to SMLM-methods based on ultraviolet and/or high illumination intensities. Due to the motility of living cells (even adherent cells), capturing at an instant of time is of utmost importance. If several channels are to be acquired, the movement of the cells introduces a shift between the sequentially acquired color channels.

The application of SMLM methods on living-cells has already been demonstrated, although no information about the influence on the cells was given.⁷⁷ Labeling methods e.g. via SNAP-tag fusion proteins are advantageous for live-cells experiments with combined SIM and SMLM imaging.⁷⁵ However, as SMLM in the SPDMPHymod mode presented here is highly invasive due to high laser intensities, the influence of these methods on living cells needs to be tested thoroughly. Moreover, SMLM-methods often require embedding media favoring the photo-switching ability of fluorophores of a specific labeling, which are generally incompatible for living specimens. Finding a reasonable compromise is highly challenging. While the 'Combo'-setup described could potentially be used in conjunction with low illumination intensity SMLM methods, such as PALM or FPALM, the problem of image construction in spite of extended molecule movements in the thousands of image frames remains. Moreover, PALM/FPALM is even more time-consuming due to on and off-switching of the excitation laser and requires fluorophores with special switching characteristics (e.g. pa-GFP). Biomedical processes taking place within the *msec* range or below can not be accessed by SMLM-methods, as the imaging process itself is ranged

in this time frame. Single molecule position information can be obtained from live-cells, though a time-resolved study, which relies on high excitation energies, will always be a limiting factor. Whether it is possible to repeatedly image living specimens with SMLM is highly dependent on the necessary intensity and embedding media, the absorption of light by the cell and the resistance of the cell to photo-toxic damage.

Based on the prior motivated background concerning AMD-treatment, a time-resolved study of pharmaceutical uptake by RPE-cells was endeavored. The long-term aim of this study is sought to be conducted using donor RPE-cells instead of the standardized ARPE-19-cell line. The behavior of the ARPE-19-cells is controversial in terms of similarities to donor RPE-cells and they do not contain AF-granules anymore. As prior described imaging of specific labeled pharmaceuticals in ARPE-19-cells without the influence of AF-signal already remains challenging. However, SMLM-imaging of the pharmaceuticals is absolute necessary in order to resolve spatial distribution and relative quantities of pharmaceutical molecules. First experiments have proven that the 'Combo'-microscope fulfills the necessary requirements for continuing this study. Nevertheless, to overcome the difficulties described, further improvements in terms of labeling-efficiency and density of living cells, photo-switching behavior of labeled pharmaceuticals including an appropriate embedding environment and the influence of AF-signals need to be conducted in order to perform a time-resolved super-resolution study of the pharmaceutical uptake.

CHAPTER 6

CONCLUSION AND OUTLOOK

Various different super-resolution fluorescence microscopy methods have become a powerful tool for tackling nano-scale problems in biomedical research. However, each imaging method is not universally applicable, addresses only very specific questions and has its limitations. In this work, a powerful and promising advanced fluorescence imaging method, which extends the range of high-resolution methods currently available, was established. The custom developed 'Combo'-super-resolution microscope combines the two high-resolution methods 'Structured Illumination (SIM)' and 'Single Molecule Localization Microscopy (SMLM)' in one robust physical setup. Moreover, the 'Combo'-microscope is equipped with a user-friendly GUI, which allows easier handling of the complex setup, and with fully automated and time-saving image acquisition algorithms. Additionally, the system is cost-efficient compared to commercially available systems.

A highly-resolved overview image provided by SIM is always desirable for SMLM-imaging as it reveals structural details, which are not obvious within a standard fluorescence image. In terms of sparse target distributions imaged with SMLM-methods a high-resolved overview image gives an orientation within the biological object, which is necessary in order to assign single molecule position information to structural information. Additionally, it has been outlined that the 'Combo'-microscope is able to deal with AF-structures as well as live-cell experiments simultaneously.

Nevertheless, it has to be noted, that both methods are mathematical reconstructions unlike instantly acquirable images in conventional fluorescence microscopy techniques. This leads to artifacts potentially introduced during the imaging and reconstruction process. Due to the complementary character of both methods, artifacts can be easily revealed as

they are generally only characteristic for one method. Therefore, a reduction in potential mis-interpretation of single molecule data can be achieved. A comparison of SIM-images with SMLM-data allows a more accurate interpretation in terms of clustering of proteins and/or fluorescent probes and whether detected signals are real or not, which is essential for linking biological functions to detected protein distributions.

In summary, both methods benefit from each other as each method compensates the weaknesses of the other. SMLM images deliver very high single molecule localization accuracies, but without further information about the structural context the highly resolved position information might even be useless. Assigning the SMLM position information to the structural information of a standard widefield fluorescence image would not necessarily increase information as in this case the widefield resolution may be too low to sufficiently reveal small structural details of the object. However, SIM images provide a sufficient resolution gain in order to visualize structures of biological objects much more detailed than conventional fluorescence microscopy. Thus position information can directly be assigned to improved structural features and increase the amount of information gained of the specimen.

Outlook

The developed 'Combo'-microscope will be a powerful tool in order to investigate various biomedical questions in life-science, which have been derived during this work. Nevertheless, a few developments in order to improve the 'Combo'-microscope still need to be conducted. It is sought to implement a few more controls into the microscope software including an absolute calibration of the microscope table and an automated saving routine for SIM-data directly to hard-disc instead of RAM. Furthermore, a script for an automated repeatedly imaging routine is sought. Moreover, it is planned to implement a user-friendly GUI for an automated SIM-reconstruction in Python, which is accessing the Matlab-reconstruction routine for SIM-images.

As outlined in previous sections, the work was motivated by a highly destructive disease affecting the central visual field of the aging eye - the age-related macular degeneration (AMD). Three main applications dealing with the impact on AMD-development and treatment will be further investigated by using the 'Combo'-microscope.

The first application will deal with the depiction of Autofluorescent (AF) particles combined with immuno-labeled structures within the retina. It has been demonstrated in this work, that SIM allows a much more detailed analysis of these AF-particles compared to

previously published reports, which were limited by the resolution of the chosen imaging method respectively. SIM was not only able to detect much more AF particles within drusen, but also to depict particles (1/3) much smaller compared to the common size of lipofuscin (LF) and melanolipofuscin (MLF) particles generally observable within retinal pigment epithelium (RPE) cells. However, particles possessed similar spectral signatures as LF and MLF. Results of a detailed analysis presented in this study support the theory that AF-particles were former LF and MLF granules generally found in RPE cells. Ring-like AF-structures also observed within drusen lead to further speculation of catabolic processes, which are connected to drusen formation.

Further studies of AF-particles within drusen combined with additional specific labeling of correlated target structures are now possible by applying the 'Combo'-microscope. Applying both methods could reveal new insights in drusen composition and formation as AF-granules or particles can be visualized at high resolution combined with super-resolved information about their direct vicinity. Nevertheless, AF structures are difficult to bleach and thus it will remain challenging to image immuno-labeled structures with SMLM in the near vicinity of the AF signal (e.g. lysosomes containing the AF-molecules such as LF or MLF). Theoretically this problem could be solved by calculating a differential stack in order to eliminate the AF-signal from the SMLM data set. This method would also allow to make single molecule signals visible, which are drowning in the AF-signal during SIM-acquisition. For this purpose the most promising would be a specific labeling with red/far-red dyes.^{39,51} As the AF-signal is strongest within the 488/568 channels less correlation would be expected for red dyes.

The second application focused on the investigation of the axon initial segment (AIS) of retinal ganglion cells, which has hardly been described in literature. Moreover, a study dealing with the cisternal organelle (CO) within the AIS is also lacking. To close this information gap a super-resolution study is of high interest in order to gain new insights in morphology and function of the AIS and the exact location of the CO. Additionally, AIS spiraling around their longitudinal axis have never been described and will be further investigated. Finally, 3D co-localization measurements of various CO-associated protein channels might help to reveal their impact on the signal transduction within the AIS.

The third application will be the study of molecule distribution of pharmaceuticals (Bevacizumab, Ranibizumab, Aflibercept) within RPE-cells *in vitro*, which are generally used for AMD treatment. Using SIM, a time-resolved study of pharmaceutical accumulation within cells will be possible due to minimal invasive laser intensities necessary for imaging. SMLM will deliver exact positions in order to be able to localize pharmaceutical molecules within specific cell compartments. Moreover, not only the visualization of labeled struc-

tures *in vitro* is possible, but also the possibility of imaging AF structures within cells. However, the method will be limited to biomedical processes taking place within a time range of seconds. Higher time-resolved imaging is not possible as even SIM-images will need a minimum of about one second for acquisition. As the pharmaceutical uptake is assumed to be a process over several hours as reported in literature and due to the very first results presented here, the 'Combo'-setup is a promising tool to reveal whether pharmaceutical accumulation within cells is taking place or not and most important in which cell-compartments the molecules can be localized. Based on this high resolution and time-resolved data it will be possible to gain new insights on the effectiveness of the different pharmaceutical for AMD treatment on the molecular level.

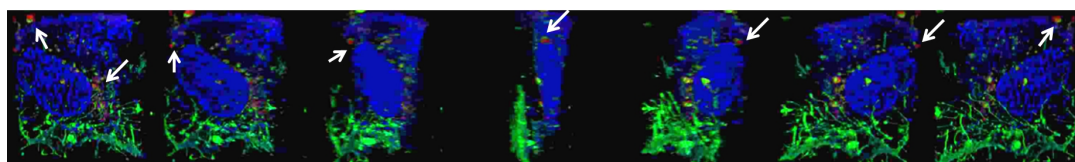


Figure 6.1: *Proof of principle: Very first results of Bevacizumab labeled with 6S-IDCC (671 nm excitation, red channel, white arrows) and detected within a ARPE-19 cell (white arrows). Nucleus and membrane were transiently transfected with GFP (488 nm excitation, blue channel) and RFP (568 nm excitation, green channel) respectively. Images were recorded in SIM-mode and show a 3D rotation by 180°. Imaging and reconstructed data shown in this figure were performed by Martin Hagmann (Kirchhoff Institute for Physics, University Heidelberg). Published on a poster-presentation during the 'Focus on Microcopy (FoM)' conference 2014 in Sydney: 'Tracking drug pathway in living-cells by super-resolution microscopy', M.Hagmann, N.Celik, S.Rossberger et al.*

Figure 6.1 shows very first results of Bevacizumab clusters, which were labeled with 6S-IDCC and detected within a standard RPE-19 cell (671 nm excitation, red channel). Cell-cultures and labeling were conducted by Nil Celik (Department of Ophthalmology, University Hospital Heidelberg). Imaging and reconstruction shown in this figure were performed by Martin Hagmann (Kirchhoff Institute for Physics, University Heidelberg), who will continue the outlined project in the course of his PhD-thesis. Nucleus and membrane were transiently transfected with GFP (488 nm excitation, blue channel) and RFP (568 nm excitation, green channel) respectively. Imaging was performed using the 3D-SIM-mode of the 'Combo'-setup. It is already at SIM-resolution possible to demonstrate Bevacizumab cluster uptake into the cell indicated by white arrows within figure 6.1.

However, single molecule distribution of Bevacizumab molecules can not be depicted using SIM due to its limited resolution. Thus imaging of pharmaceutical distribution with SMLM-mode is highly sought, but was hardly realized due to prior mentioned difficulties. Single molecule statistics will allow comparing relative densities of different VEGF-inhibitor pharmaceuticals uptake into cells. Furthermore, a localization determination within specific cell-compartments can be conducted. Imaging of 6S-IDCC labeled

Bevacizumab with SMLM-mode within living cells is currently being tested and showing promising first results. 6S-IDCC has already been proven to provide sufficient blinking statistics. However, best photo-switching is achieved using an oxygen scavenging systems, though this is highly toxic for cells. Therefore, a sufficient embedding medium still needs to be evaluated.

Nevertheless, these results are a first sufficient proof of principle for the outlined project dealing with the comparison of potential Bevacizumab, Ranibizumab and Aflibercept uptake in RPE-cells. Super-resolved distribution will reveal potential differences between pharmaceuticals in terms of quantitative uptake by RPE-cells. Moreover, a qualitative spatial localization determination of pharmaceuticals can be conducted when introducing astigmatism into the detection path. This can be realized either by a cylindrical lens or by a simple slide as recently demonstrated.³⁹ Further experiments will also include a time-resolved visualization of the pharmaceutical uptake using SIM-imaging. Co-localization experiments of pharmaceuticals with labeled VEGF, which allow to visualize the effective binding rate of the different drugs, will complete this study. Consequently, new insights into the biological mechanism will be gained with direct consequences for future AMD-treatment.

BIBLIOGRAPHY

- [1] Rossberger S, Best G, Baddeley D, Heintzmann R, Birk U, Dithmar S, et al. Combination of structured illumination and single molecule localization microscopy in one setup. *J Opt.* 2013;15:094003. VI, 1, 6, 33, 34, 35, 37, 48, 72, 73
- [2] Rossberger S, Ach T, Best G, Cremer C, Heintzmann R, Dithmar S. High-resolution imaging of autofluorescent particles within drusen using structured illumination microscopy. *Br J Ophthalmol.* 2013 Apr;97(4):518–523. Available from: <http://dx.doi.org/10.1136/bjophthalmol-2012-302350>. VI, 4, 12, 21, 28, 49, 52, 53, 60, 61, 62, 63, 64, 65
- [3] Abbe E. Beitrage zur Theorie des Mikroskops und der mikroskopischen Wahrnehmung. *Arch Mikrosk Anat.* 1873;9:413–420. 1, 7, 15
- [4] Rayleigh L. On the Theory of Optical Images with Special Reference to the Microscope. *Philos Mag.* 1896;42:167–195. 1, 7, 15
- [5] Cremer C, Masters BR. Resolution enhancement techniques in microscopy. *The European Physical Journal H.* 2013;38:281–344. 1, 5, 11, 19
- [6] Wicker K. Increasing resolution and light efficiency in fluorescence microscopy. King's College London, Randall Division of Cell and Molecular Biophysics; 2010. 1, 6, 93
- [7] Annibale P, Vanni S, Scarselli M, Rothlisberger U, Radenovic A. Identification of clustering artifacts in photoactivated localization microscopy. *Nat Methods.* 2011 Jul;8(7):527–528. Available from: <http://dx.doi.org/10.1038/nmeth.1627>. 93
- [8] Endesfelder U, Heilemann M. Art and artifacts in single-molecule localization mi-

- croscopy: beyond attractive images. *Nat Methods*. 2014 Feb;11(3):235–238. Available from: <http://dx.doi.org/10.1038/nmeth.2852>. 1, 6
- [9] Kolb H, Nelson R, Fernandez E, Jones B, editors. *The Organisation of the Retina and Visual System*. Webvision; 2011. 2, 25
- [10] Khan J, Marin-Castano ME, Kolar P, Talu SD, Golan S, Goldstein M, et al. Age-Related Macular Degeneration - Etiology, Diagnosis and Management - A Glance at the Future. Giudice GL, editor. ISBN 978-953-51-1113-9. InTech; 2013. 3, 27, 28, 30
- [11] Congdon N, O'Colmain B, Klaver CCW, Klein R, Munoz B, Friedman DS, et al. Causes and prevalence of visual impairment among adults in the United States. *Arch Ophthalmol*. 2004 Apr;122(4):477–485. 2, 27
- [12] Zarbin MA. Age-related macular degeneration: review of pathogenesis. *Eur J Ophthalmol*. 1998;8(4):199–206. 2, 3, 27
- [13] Zarbin MA. Current concepts in the pathogenesis of age-related macular degeneration. *Arch Ophthalmol*. 2004 Apr;122(4):598–614. Available from: <http://dx.doi.org/10.1001/archopht.122.4.598>. 2, 3, 27
- [14] Sarks JP, Sarks SH, Killingsworth MC. Evolution of soft drusen in age-related macular degeneration. *Eye (Lond)*. 1994;8 (Pt 3):269–283. Available from: <http://dx.doi.org/10.1038/eye.1994.57>. 3
- [15] Sarks SH, Arnold JJ, Killingsworth MC, Sarks JP. Early drusen formation in the normal and aging eye and their relation to age related maculopathy: a clinicopathological study. *Br J Ophthalmol*. 1999 Mar;83(3):358–368. 3
- [16] Anderson DH, Mullins RF, Hageman GS, Johnson LV. A role for local inflammation in the formation of drusen in the aging eye. *Am J Ophthalmol*. 2002 Sep;134(3):411–431. 3, 87, 88, 89
- [17] Hageman GS, Luthert PJ, Victor Chong NH, Johnson LV, Anderson DH, Mullins RF. An integrated hypothesis that considers drusen as biomarkers of immune-mediated processes at the RPE-Bruch's membrane interface in aging and age-related macular degeneration. *Prog Retin Eye Res*. 2001 Nov;20(6):705–732. 87, 88
- [18] Rudolf M, Clark ME, Chimento MF, Li CM, Medeiros NE, Curcio CA. Prevalence and morphology of druse types in the macula and periphery of eyes with age-related maculopathy. *Invest Ophthalmol Vis Sci*. 2008 Mar;49(3):1200–1209. Available from: <http://dx.doi.org/10.1167/iovs.07-1466>. 3, 28, 52, 59, 62, 87

- [19] Curcio CA, Medeiros NE, Millican CL. Photoreceptor loss in age-related macular degeneration. *Invest Ophthalmol Vis Sci.* 1996 Jun;37(7):1236–1249. 3, 23
- [20] Medeiros NE, Curcio CA. Preservation of ganglion cell layer neurons in age-related macular degeneration. *Invest Ophthalmol Vis Sci.* 2001 Mar;42(3):795–803. 3
- [21] Rasband MN. The axon initial segment and the maintenance of neuronal polarity. *Nat Rev Neurosci.* 2010 Aug;11(8):552–562. Available from: <http://dx.doi.org/10.1038/nrn2852>. 4, 23, 24, 76, 82
- [22] Klettner AK, Kruse ML, Meyer T, Wesch D, Kabelitz D, Roeder J. Different properties of VEGF-antagonists: Bevacizumab but not Ranibizumab accumulates in RPE cells. *Graefes Arch Clin Exp Ophthalmol.* 2009 Dec;247(12):1601–1608. Available from: <http://dx.doi.org/10.1007/s00417-009-1136-0>. 4, 31
- [23] Group CATT, Martin DF, Maguire MG, Ying Gs, Grunwald JE, Fine SL, et al. Ranibizumab and bevacizumab for neovascular age-related macular degeneration. *N Engl J Med.* 2011 May;364(20):1897–1908. Available from: <http://dx.doi.org/10.1056/NEJMoa1102673>. 4, 31
- [24] Rudolf M, Malek G, Messinger JD, Clark ME, Wang L, Curcio CA. Sub-retinal drusenoid deposits in human retina: Organization and Composition. *Exp Eye Res.* 2008;87(5):402–408. 4
- [25] Spaide RF, Curcio CA. Drusen characterization with multimodal imaging. *Retina.* 2010 Oct;30(9):1441–1454. Available from: <http://dx.doi.org/10.1097/IAE.0b013e3181ee5ce8>. 4, 28
- [26] Hageman GS, Mullins RF. Molecular composition of drusen as related to substructural phenotype. *Mol Vis.* 1999 Nov;5:28. 4, 28, 87
- [27] Gouras P, Ivert L, Mattison JA, Ingram DK, Neuringer M. Drusenoid maculopathy in rhesus monkeys: autofluorescence, lipofuscin and drusen pathogenesis. *Graefes Arch Clin Exp Ophthalmol.* 2008 Oct;246(10):1403–1411. Available from: <http://dx.doi.org/10.1007/s00417-008-0911-7>.
- [28] Wang L, Clark ME, Crossman DK, Kojima K, Messinger JD, Mobley JA, et al. Abundant lipid and protein components of drusen. *PLoS One.* 2010;5(4):e10329. Available from: <http://dx.doi.org/10.1371/journal.pone.0010329>. 4, 28, 87
- [29] Heintzmann R, Cremer C. Laterally Modulated Excitation Microscopy: Improvement of resolution by using a diffraction grating. *Proc SPIE.* 1999;3568:185–196. 5, 12, 13, 14, 19, 52, 53, 54, 58

- [30] Gustafsson MG. Surpassing the lateral resolution limit by a factor of two using structured illumination microscopy. *J Microsc.* 2000 May;198(Pt 2):82–87. 5, 12, 19
- [31] Ach T, Best G, Ruppenstein M, Amberger R, Cremer C, Dithmar S. High-resolution fluorescence microscopy of retinal pigment epithelium using structured illumination. *Ophthalmologe.* 2010 Nov;107(11):1037–1042. Available from: <http://dx.doi.org/10.1007/s00347-010-2183-y>. 5, 21
- [32] Best G, Amberger R, Baddeley D, Ach T, Dithmar S, Heintzmann R, et al. Structured illumination microscopy of autofluorescent aggregations in human tissue. *Micron.* 2011 Sep;42:330–335. Available from: <http://dx.doi.org/10.1016/j.micron.2010.06.016>. 5, 13, 14, 21, 34, 35, 52, 53, 54, 91
- [33] Schermelleh L, Carlton PM, Haase S, Shao L, Winoto L, Kner P, et al. Subdiffraction Multicolor Imaging of the Nuclear Periphery with 3D Structured Illumination Microscopy. *Science.* 2008;320:1332–1336. 5, 21
- [34] Kner P, Chhun BB, Griffis ER, Winoto L, Gustafsson MGL. Super-resolution video microscopy of live cells by structured illumination. *Nature Methods.* 2009;6:339–344. 5, 19
- [35] Betzig E, Patterson GH, Sougrat R, Lindwasser OW, Olenych S, Bonifacino JS, et al. Imaging Intracellular Fluorescent Proteins at Nanometer Resolution. *Science Express.* 2006 August;p. 1–5. 5, 15
- [36] Hess ST, Girirajan TPK, Mason MD. Ultra-High Resolution Imaging by Fluorescence Photoactivation Localization Microscopy (FPALM). *Biophysical Journal.* 2006 September;p. 1–24. 15
- [37] Juette MF, Gould TJ, Lessard MD, Mlodzianoski MJ, Nagpure BS, Bennett BT, et al. Three-dimensional sub-100 nm resolution fluorescence microscopy of thick samples. *Nature Methods.* 2008 June;5(6):527–529. 5, 15, 21
- [38] Baddeley D, Jayasinghe ID, Cremer C, Cannell MB, Soeller C. Light-Induced Dark States of Organic Fluochromes Enable 30nm Resolution Imaging in Standart Media. *Biophysical Journal: Biophysical Letters.* 2009;96:L22–L24. 5, 15, 16, 42
- [39] Baddeley D, Crossman D, Rossberger S, Cheyne JE, Montgomery JM, Jayasinghe ID, et al. 4D Super-Resolution Microscopy with Conventional Fluorophores and Single Wavelength Excitation in Optically Thick Cells and Tissues. *PLoS ONE.* 2011 May;6:e20645–e20645. 5, 15, 21, 41, 53, 91, 92, 99, 101

- [40] Lemmer P, Gunkel M, Baddeley D, Kaufmann R, Urich A, Weiland Y, et al. SPDM: light microscopy with single-molecule resolution at the nanoscale. *Applied Physics B: Laser and Optics*. 2008 June/September;93:1–12. 5, 15, 21, 42
- [41] Rust MJ, Bates M, Zhuang X. Sub-diffraction-limit imaging by stochastic optical reconstruction microscopy (STORM). *Nature Methods*. 2006 Oktober;3(10):793–795. 5, 15
- [42] Bates M, Huang B, Dempsey GT, Zhuang X. Multicolor Super-Resolution Imaging with Photo-Switchable Fluorescent Probes. *Science*. 2007;317:1749–1753. 15
- [43] Heilemann M, van de Linde S, Schuettelpelz M, Kasper R, Seefeldt B, Mukherjee A, et al. Subdiffraction-Resolution Fluorescence Imaging with Conventional Fluorescent Probes. *Angewandte Chemie*. 2008;47:6172–6176. 15, 21, 49, 84, 93
- [44] Huang B, Wang W, Bates M, Zhuang X. Three-Dimensional Super-Resolution Imaging by Stochastic Optical Reconstruction Microscopy. *Science*. 2008;319:810–813. 5, 15, 21
- [45] Heilemann M, Dedecker P, Hofkens J, Sauer M. Photoswitches: Key molecules for subdiffraction-resolution fluorescence imaging and molecular quantification. *Laser & Photon*. 2009;Rev. 3(1-2):180–202. 5
- [46] Gordon MP, Ha T, Selvin PR. Single-molecule high-resolution imaging with photo-bleaching. *Proc Natl Acad Sci U S A*. 2004 Apr;101(17):6462–6465. Available from: <http://dx.doi.org/10.1073/pnas.0401638101>. 5
- [47] Lidke K, Rieger B, Jovin T, Heintzmann R. Superresolution by localization of quantum dots using blinking statistics. *Opt Express*. 2005 Sep;13(18):7052–7062. 5
- [48] Schaefer LH, Schuster D, Schaffer J. Structured illumination microscopy: artefact analysis and reduction utilizing a parameter optimization approach. *J Microsc*. 2004 Nov;216(Pt 2):165–174. Available from: <http://dx.doi.org/10.1111/j.0022-2720.2004.01411.x>. 6, 93
- [49] Heintzmann R, Kubitscheck U, Dobrucki JW, Nienhaus GU, Nienhaus K, Naredi-Rainer N, et al. *Fluorescence Microscopy: From Principles to Biological Applications*. Kubitscheck U, editor. Wiley-Blackwell; 2013. 8, 9, 10, 11, 14
- [50] Allen JR, Ross ST, Davidson MW. Sample preparation for single molecule localization microscopy. *Phys Chem Chem Phys*. 2013 Nov;15(43):18771–18783. Available from: <http://dx.doi.org/10.1039/c3cp53719f>. 10

- [51] Rossberger S. Multi-color Localization Microscopy with a Single Excitation Laser Line using Far-Red Dyes. University of Heidelberg; 2010. 11, 15, 16, 18, 49, 91, 99
- [52] Heintzmann R, Ficz G. Breaking the resolution limit in light microscopy. *Brief Funct Genomic Proteomic*. 2006 Dec;5(4):289–301. Available from: <http://dx.doi.org/10.1093/bfgp/e11036>. 13, 19, 52, 53, 54
- [53] Heintzmann R, Benedetti PA. High-resolution Image Reconstruction in Fluorescence Microscopy with Patterned Excitation. *Applied Optics*. 2006;45:5037–5045. 13
- [54] Karadaglic D, Wilson T. Image formation in structured illumination wide-field fluorescence microscopy. *Micron*. 2008;39:808–818. 14
- [55] Wicker K, Mandula O, Best G, Fiolka R, Heintzmann R. Phase optimisation for structured illumination microscopy. *Opt Express*. 2013;21:2032–2049. 14, 21
- [56] Best G. Development of a Structured Illumination Ophthalmoscope for High Resolution Imaging of the Human Eyeground and Improvements to Structured Illumination Microscopy. University of Heidelberg; 2014. 14, 53, 76
- [57] Gunkel M, Erdel F, Rippe K, Lemmer P, Kaufmann K, Hoermann C, et al. Dual color localization microscopy of cellular nanostructures. *Biotechnology Journal*. 2009;4(6):927–938. 15, 19, 21, 42, 58
- [58] Cremer C, Kaufmann R, Gunkel M, Pres S, Weiland Y, Mueller P, et al. Superresolution imaging of biological nanostructures by spectral precision distance microscopy. *Biotechnol J*. 2011 Sep;6(9):1037–1051. Available from: <http://dx.doi.org/10.1002/biot.201100031>. 15, 42
- [59] Vogelsang J, Kasper R, Steinhauer C, Person B, Heilemann M, Sauer M, et al. A Reducing and Oxidizing System Minimizes Photobleaching and Blinking of Fluorescent Dyes. *Angewandte Chemie*. 2008;47:5465–5469. 15, 21, 84, 93
- [60] Levenberg K. A method for the solution of certain problems in least squares. *Quart Appl Math*. 1944;2:164–168. 16
- [61] Marquardt D. An Algorithm for Least-Squares Estimation of Nonlinear Parameters. *Journal of the Society for Industrial and Applied Mathematics*. 1963;11:431–441. 16
- [62] PythonSoftwareFoundation. Python Programming Language–Official Website. <http://www.python.org/>; 2009. Available from: <http://www.python.org/psf/>. 16

- [63] Thompson RE, Larson DR, Webb WW. Precise Nanometer Localization Analysis for Individual Fluorescent Probes. *Biophysical Journal*. 2002;82:2775–2783. 17
- [64] Baddeley D, Cannell MB, Soeller C. Visualization of localization microscopy data. *Microsc Microanal*. 2010 Feb;16(1):64–72. Available from: <http://dx.doi.org/10.1017/S143192760999122X>. 19, 53, 58, 69, 70, 72, 73, 74, 90
- [65] Schermelleh L, Heintzmann R, Leonhardt H. A guide to super-resolution fluorescence microscopy. *J Cell Biol*. 2010 Jul;190(2):165–175. Available from: <http://dx.doi.org/10.1083/jcb.201002018>. 19
- [66] Denk W, Strickler JH, Webb WW. Two-photon laser scanning fluorescence microscopy. *Science*. 1990 Apr;248(4951):73–76. 19
- [67] Heintzmann R, Jovin TM, Cremer C. Saturated patterned excitation microscopy—a concept for optical resolution improvement. *J Opt Soc Am A Opt Image Sci Vis*. 2002 Aug;19(8):1599–1609. 19, 21
- [68] Heintzmann R. Saturated patterned excitation microscopy with two-dimensional excitation patterns. *Micron*. 2003;34(6-7):283–291.
- [69] Gustafsson MGL. Nonlinear structured-illumination microscopy: Wide-field fluorescence imaging with theoretically unlimited resolution. *PNAS: Proceedings of the National Academy of Sciences*. 2005;102:13081–13086. 19, 21
- [70] Hirvonen LM, Wicker K, Mandula O, Heintzmann R. Structured illumination microscopy of a living cell. *Eur Biophys J*. 2009 Jul;38(6):807–812. Available from: <http://dx.doi.org/10.1007/s00249-009-0501-6>. 19
- [71] Gao L, Shao L, Higgins CD, Poulton JS, Peifer M, Davidson MW, et al. Non-invasive Imaging beyond the Diffraction Limit of 3D Dynamics in Thickly Fluorescent Specimens. *Cell*. 2012 Dec;151(6):1370–1385. Available from: <http://dx.doi.org/10.1016/j.cell.2012.10.008>. 19
- [72] Xie XS, Choi PJ, Li GW, Lee NK, Lia G. Single-molecule approach to molecular biology in living bacterial cells. *Annu Rev Biophys*. 2008;37:417–444. Available from: <http://dx.doi.org/10.1146/annurev.biophys.37.092607.174640>. 21
- [73] Shroff H, Galbraith CG, Galbraith JA, Betzig E. Live-cell photoactivated localization microscopy of nanoscale adhesion dynamics. *Nat Methods*. 2008 May;5(5):417–423. Available from: <http://dx.doi.org/10.1038/nmeth.1202>.

- [74] Testa I, Wurm CA, Medda R, Rothermel E, von Middendorf C, Foelling J, et al. Multicolor fluorescence nanoscopy in fixed and living cells by exciting conventional fluorophores with a single wavelength. *Biophys J*. 2010 Oct;99(8):2686–2694. Available from: <http://dx.doi.org/10.1016/j.bpj.2010.08.012>.
- [75] Klein T, Loeschberger A, Proppert S, Wolter S, van de Linde S, Sauer M. Live-cell dSTORM with SNAP-tag fusion proteins. *Nat Methods*. 2011 Jan;8(1):7–9. Available from: <http://dx.doi.org/10.1038/nmeth0111-7b>. 95
- [76] Ries J, Kaplan C, Platonova E, Eghlidi H, Ewers H. A simple, versatile method for GFP-based super-resolution microscopy via nanobodies. *Nat Methods*. 2012 Jun;9(6):582–584. Available from: <http://dx.doi.org/10.1038/nmeth.1991>.
- [77] Jones SA, Shim SH, He J, Zhuang X. Fast, three-dimensional super-resolution imaging of live cells. *Nat Methods*. 2011 Jun;8(6):499–508. Available from: <http://dx.doi.org/10.1038/nmeth.1605>. 95
- [78] Cella Zanacchi F, Lavagnino Z, Perrone Donnorso M, Del Bue A, Furia L, Faretta M, et al. Live-cell 3D super-resolution imaging in thick biological samples. *Nat Methods*. 2011 Dec;8(12):1047–1049. Available from: <http://dx.doi.org/10.1038/nmeth.1744>. 21
- [79] Finan K, Flottmann B, Heilemann M. Photoswitchable fluorophores for single-molecule localization microscopy. *Methods Mol Biol*. 2013;950:131–151. Available from: http://dx.doi.org/10.1007/978-1-62703-137-0_9. 21
- [80] Hell SW, Wichmann J. Breaking the Diffraction Resolution Limit by Stimulated-Emission-Depletion Fluorescence Microscopy. *Optics Letters*. 1994;19:780–782. 21, 36
- [81] Hell S, Stelzer EHK. Fundamental Improvement of Resolution with a 4Pi-Confocal Fluorescence Microscope using 2-Photon Excitation. *Optics Communications*. 1992;93:277–282. 21
- [82] Verveer PJ, Swoger J, Pampaloni F, Greger K, Marcello M, Stelzer EHK. High-resolution three-dimensional imaging of large specimens with light sheet-based microscopy. *Nat Methods*. 2007 Apr;4(4):311–313. Available from: <http://dx.doi.org/10.1038/nmeth1017>. 21
- [83] Ritter JG, Veith R, Veenendaal A, Siebrasse JP, Kubitscheck U. Light sheet microscopy for single molecule tracking in living tissue. *PLoS One*. 2010;5(7):e11639. Available from: <http://dx.doi.org/10.1371/journal.pone.0011639>. 21

- [84] Bock H, Geisler C, Wurm CA, von Middendorff C, Jakobs S, Schoenle A, et al. Two-color far-field fluorescence nanoscopy based on photoswitchable emitters. *Applied Physics*. 2007;B88:161–165. [21](#)
- [85] Shroff H, Galbraith CG, Galbraith JA, White H, Gillette J, Olenych S, et al. Dual color superresolution imaging of genetically expressed probes within individual adhesion complexes. *PNAS: Proceedings of the National Academy of Sciences*. 2007;104(51):20308–20313.
- [86] Donnert G, Keller J, Wurma CA, Rizzoli SO, Westphal V, Schoenle A, et al. Two-Color Far-Field Fluorescence Nanoscopy. *Biophysical Journal: Biophysical Letters*. 2007;p. L67–L69.
- [87] Bossi M, Foelling J, Belov VN, Boyarskiy VP, Medda R, Egner A, et al. Multicolor Far-Field Fluorescence Nanoscopy through Isolated Detection of Distinct Molecular Species. *Biophysical Journal: Biophysical Letters*. 2008;8 (8):2463–2468. [21](#)
- [88] Ach T, Best G, Rossberger S, Heintzmann R, Cremer C, Dithmar S. Autofluorescence imaging of human RPE cell granules using structured illumination microscopy. *Br J Ophthalmol*. 2012 Aug;96(8):1141–1144. Available from: <http://dx.doi.org/10.1136/bjophthalmol-2012-301547>. [21](#), [66](#), [90](#), [91](#)
- [89] Trepel M. *Neuroanatomy*. 4th ed. Urban & Fisher; 1999. [22](#)
- [90] Strauss O. The retinal pigment epithelium in visual function. *Physiol Rev*. 2005 Jul;85(3):845–881. Available from: <http://dx.doi.org/10.1152/physrev.00021.2004>. [23](#), [24](#), [26](#), [83](#)
- [91] Sparrow JR, Hicks D, Hamel CP. The retinal pigment epithelium in health and disease. *Curr Mol Med*. 2010 Dec;10(9):802–823. [23](#), [83](#)
- [92] Kevany BM, Palczewski K. Phagocytosis of retinal rod and cone photoreceptors. *Physiology (Bethesda)*. 2010 Feb;25(1):8–15. Available from: <http://dx.doi.org/10.1152/physiol.00038.2009>. [23](#)
- [93] Puthussery T, Venkataramani S, Gayet-Primo J, Smith RG, Taylor WR. NaV1.1 channels in axon initial segments of bipolar cells augment input to magnocellular visual pathways in the primate retina. *J Neurosci*. 2013 Oct;33(41):16045–16059. Available from: <http://dx.doi.org/10.1523/JNEUROSCI.1249-13.2013>. [23](#)
- [94] Wu C, Ivanova E, Cui J, Lu Q, Pan ZH. Action potential generation at an axon initial segment-like process in the axonless retinal AII amacrine cell. *J Neurosci*. 2011 Oct;31(41):14654–14659. Available from: <http://dx.doi.org/10.1523/JNEUROSCI.1861-11.2011>. [23](#)

- [95] Hedstrom KL, Ogawa Y, Rasband MN. AnkyrinG is required for maintenance of the axon initial segment and neuronal polarity. *J Cell Biol.* 2008 Nov;183(4):635–640. Available from: <http://dx.doi.org/10.1083/jcb.200806112>. 23
- [96] Sobotzik JM, Sie JM, Politi C, Del Turco D, Bennett V, Deller T, et al. AnkyrinG is required to maintain axo-dendritic polarity in vivo. *Proc Natl Acad Sci U S A.* 2009 Oct;106(41):17564–17569. Available from: <http://dx.doi.org/10.1073/pnas.0909267106>. 23
- [97] Calkins DJ. Age-related changes in the visual pathways: blame it on the axon. *Invest Ophthalmol Vis Sci.* 2013 Dec;54(14):ORSF37–ORSF41. Available from: <http://dx.doi.org/10.1167/iovs.13-12784>. 24
- [98] Ben-Shabat S, Parish CA, Hashimoto M, Liu J, Nakanishi K, Sparrow JR. Fluorescent pigments of the retinal pigment epithelium and age-related macular degeneration. *Bioorg Med Chem Lett.* 2001 Jun;11(12):1533–1540. 25, 27
- [99] Tang PH, Kono M, Koutalos Y, Ablonczy Z, Crouch RK. New insights into retinoid metabolism and cycling within the retina. *Prog Retin Eye Res.* 2013 Jan;32:48–63. Available from: <http://dx.doi.org/10.1016/j.preteyeres.2012.09.002>. 26, 27
- [100] Bui TV, Han Y, Radu RA, Travis GH, Mata NL. Characterization of native retinal fluorophores involved in biosynthesis of A2E and lipofuscin-associated retinopathies. *J Biol Chem.* 2006 Jun;281(26):18112–18119. Available from: <http://dx.doi.org/10.1074/jbc.M601380200>. 26
- [101] Lamb LE, Simon JD. A2E: a component of ocular lipofuscin. *Photochem Photobiol.* 2004 Feb;79(2):127–136. 26, 27
- [102] Sparrow JR, Gregory-Roberts E, Yamamoto K, Blonska A, Ghosh SK, Ueda K, et al. The bisretinoids of retinal pigment epithelium. *Prog Retin Eye Res.* 2012 Mar;31(2):121–135. Available from: <http://dx.doi.org/10.1016/j.preteyeres.2011.12.001>. 26
- [103] Parish CA, Hashimoto M, Nakanishi K, Dillon J, Sparrow J. Isolation and one-step preparation of A2E and iso-A2E, fluorophores from human retinal pigment epithelium. *Proc Natl Acad Sci U S A.* 1998 Dec;95(25):14609–14613. 26
- [104] Sparrow JR, Wu Y, Kim CY, Zhou J. Phospholipid meets all-trans-retinal: the making of RPE bisretinoids. *J Lipid Res.* 2010 Feb;51(2):247–261. Available from: <http://dx.doi.org/10.1194/jlr.R000687>. 27

- [105] Ablonczy Z, Gutierrez DB, Grey AC, Schey KL, Crouch RK. Molecule-specific imaging and quantitation of A2E in the RPE. *Adv Exp Med Biol.* 2012;723:75–81. Available from: http://dx.doi.org/10.1007/978-1-4614-0631-0_11. 27
- [106] Ablonczy Z, Higbee D, Anderson DM, Dahrouj M, Grey AC, Gutierrez D, et al. Lack of correlation between the spatial distribution of A2E and lipofuscin fluorescence in the human retinal pigment epithelium. *Invest Ophthalmol Vis Sci.* 2013 Aug;54(8):5535–5542. Available from: <http://dx.doi.org/10.1167/iovs.13-12250>. 27
- [107] Delori FC, Fleckner MR, Goger DG, Weiter JJ, Dorey CK. Autofluorescence distribution associated with drusen in age-related macular degeneration. *Invest Ophthalmol Vis Sci.* 2000 Feb;41(2):496–504. 27, 28
- [108] Sakai N, Decatur J, Nakanishi K ea. Ocular age pigment A2-E: an unprecedented pyridinium bis-retinoid. *J Am Chem Soc.* 1996;118:1559–1560. 27
- [109] Warburton S, Davis WE, Southwick K, Xin H, Woolley AT, Burton GF, et al. Proteomic and phototoxic characterization of melanolipofuscin: correlation to disease and model for its origin. *Mol Vis.* 2007;13:318–329. 27
- [110] Abdelsalam A, Del Priore L, Zarbin MA. Drusen in age-related macular degeneration: pathogenesis, natural course, and laser photocoagulation-induced regression. *Surv Ophthalmol.* 1999;44(1):1–29. 27
- [111] Pauleikhoff D, Barondes MJ, Minassian D, Chisholm IH, Bird AC. Drusen as risk factors in age-related macular disease. *Am J Ophthalmol.* 1990 Jan;109(1):38–43.
- [112] Curcio CA, Millican CL. Basal linear deposit and large drusen are specific for early age-related maculopathy. *Arch Ophthalmol.* 1999 Mar;117(3):329–339. 28
- [113] Bird AC, Bressler NM, Bressler SB, Chisholm IH, Coscas G, Davis MD, et al. An international classification and grading system for age-related maculopathy and age-related macular degeneration. The International ARM Epidemiological Study Group. *Surv Ophthalmol.* 1995;39(5):367–374. 27
- [114] Curcio CA, Medeiros NE, Millican CL. The Alabama Age-Related Macular Degeneration Grading System for donor eyes. *Invest Ophthalmol Vis Sci.* 1998 Jun;39(7):1085–1096. 28, 87
- [115] Newsome DA, Hewitt AT, Huh W, Robey PG, Hassell JR. Detection of specific extracellular matrix molecules in drusen, Bruch's membrane, and ciliary body. *Am J Ophthalmol.* 1987 Oct;104(4):373–381. 28

- [116] Marmorstein AD, Marmorstein LY, Sakaguchi H, Hollyfield JG. Spectral profiling of autofluorescence associated with lipofuscin, Bruch's Membrane, and sub-RPE deposits in normal and AMD eyes. *Invest Ophthalmol Vis Sci*. 2002 Jul;43(7):2435–2441. 28
- [117] Bressler NM, Silva JC, Bressler SB, Fine SL, Green WR. Clinicopathologic correlation of drusen and retinal pigment epithelial abnormalities in age-related macular degeneration. *Retina*. 1994;14(2):130–142. 28
- [118] Spraul CW, Lang GE, Grossniklaus HE, Lang GK. Characteristics of drusen and changes in Bruch's membrane in eyes with age-related macular degeneration. *Histological study*. *Ophthalmologie*. 1998 Feb;95(2):73–79. 28
- [119] Klein R, Davis MD, Magli YL, Segal P, Klein BE, Hubbard L. The Wisconsin age-related maculopathy grading system. *Ophthalmology*. 1991 Jul;98(7):1128–1134. 28, 59, 62
- [120] Jousseaume AM, Kirchhof B, Gottstein C. Molecular mechanisms of vasculogenesis and angiogenesis. What regulates vascular growth? *Ophthalmologie*. 2003 Apr;100(4):284–291. Available from: <http://dx.doi.org/10.1007/s00347-003-0799-x>. 28
- [121] Meyer CH, Holz FG. Preclinical aspects of anti-VEGF agents for the treatment of wet AMD: ranibizumab and bevacizumab. *Eye (Lond)*. 2011 Jun;25(6):661–672. Available from: <http://dx.doi.org/10.1038/eye.2011.66>. 29
- [122] Ferrara N, Damico L, Shams N, Lowman H, Kim R. Development of ranibizumab, an anti-vascular endothelial growth factor antigen binding fragment, as therapy for neovascular age-related macular degeneration. *Retina*. 2006 Oct;26(8):859–870. Available from: <http://dx.doi.org/10.1097/01.iae.0000242842.14624.e7>. 30
- [123] CCCOU Comparison of Age-related Macular Degeneration Treatments Trials (CATT) Research Group Cole Eye Institute, Martin DF, Maguire MG, Fine SL, Ying Gs, Jaffe GJ, et al. Ranibizumab and bevacizumab for treatment of neovascular age-related macular degeneration: two-year results. *Ophthalmology*. 2012 Jul;119(7):1388–1398. Available from: <http://dx.doi.org/10.1016/j.ophtha.2012.03.053>. 31
- [124] Mordenti J, Cuthbertson RA, Ferrara N, Thomsen K, Berleau L, Licko V, et al. Comparisons of the intraocular tissue distribution, pharmacokinetics, and safety of 125I-labeled full-length and Fab antibodies in rhesus monkeys following intravitreal administration. *Toxicol Pathol*. 1999;27(5):536–544. 31

- [125] Heiduschka P, Fietz H, Hofmeister S, Schultheiss S, Mack AF, Peters S, et al. Penetration of bevacizumab through the retina after intravitreal injection in the monkey. *Invest Ophthalmol Vis Sci*. 2007 Jun;48(6):2814–2823. 31
- [126] Heiduschka P, Julien S, Hofmeister S, Bartz-Schmidt KU, Schraermeyer U. Bevacizumab (avastin) does not harm retinal function after intravitreal injection as shown by electroretinography in adult mice. *Retina*. 2008 Jan;28(1):46–55. Available from: <http://dx.doi.org/10.1097/IAE.0b013e31815e9368>. 31
- [127] Shahar J, Avery RL, Heilweil G, Barak A, Zemel E, Lewis GP, et al. Electrophysiologic and retinal penetration studies following intravitreal injection of bevacizumab (Avastin). *Retina*. 2006 Mar;26(3):262–269. 31
- [128] Klettner A, Roeder J. Comparison of bevacizumab, ranibizumab, and pegaptanib in vitro: efficiency and possible additional pathways. *Invest Ophthalmol Vis Sci*. 2008 Oct;49(10):4523–4527. Available from: <http://dx.doi.org/10.1167/iovs.08-2055>. 31
- [129] Miura Y, Klettner A, Roeder J. VEGF antagonists decrease barrier function of retinal pigment epithelium in vitro: possible participation of intracellular glutathione. *Invest Ophthalmol Vis Sci*. 2010 Sep;51(9):4848–4855. Available from: <http://dx.doi.org/10.1167/iovs.09-4699>. 31
- [130] Bakri SJ, Snyder MR, Reid JM, Pulido JS, Ezzat MK, Singh RJ. Pharmacokinetics of intravitreal ranibizumab (Lucentis). *Ophthalmology*. 2007 Dec;114(12):2179–2182. Available from: <http://dx.doi.org/10.1016/j.ophtha.2007.09.012>. 31
- [131] Klettner A, Moehle F, Roeder J. Intracellular bevacizumab reduces phagocytotic uptake in RPE cells. *Graefes Arch Clin Exp Ophthalmol*. 2010 Jun;248(6):819–824. Available from: <http://dx.doi.org/10.1007/s00417-010-1317-x>. 32
- [132] Best G. Weiterentwicklung eines Aufbaus zur multispektralen hochauflösenden Fluoreszenzmikroskopie mit strukturierter Beleuchtung. University of Heidelberg; 2009. 33
- [133] Baddeley D. Precision measurements with SMI and 4Pi Microscopy. University of Heidelberg; 2007. 35
- [134] Baddeley D, Cannell MB, Soeller C. Three-Dimensional Sub-100 nm Super-Resolution Imaging of Biological Samples Using a Phase Ramp in the Objective Pupil. *Nano Res*. 2011;4(6):589 – 598. 53

- [135] Rasband MN. Composition, assembly, and maintenance of excitable membrane domains in myelinated axons. *Semin Cell Dev Biol.* 2011 Apr;22(2):178–184. Available from: <http://dx.doi.org/10.1016/j.semcdb.2010.09.010>. 74
- [136] Philp NJ, Bernstein MH. Phagocytosis by retinal pigment epithelium explants in culture. *Exp Eye Res.* 1981 Jul;33(1):47–53. 83
- [137] Klettner A, Moehle F, Lucius R, Roeder J. Quantifying FITC-labeled latex beads opsonized with photoreceptor outer segment fragments: an easy and inexpensive method of investigating phagocytosis in retinal pigment epithelium cells. *Ophthalmic Res.* 2011;46(2):88–91. Available from: <http://dx.doi.org/10.1159/000323271>. 83
- [138] Vogt SD, Curcio CA, Wang L, Li CM, McGwin G Jr, Medeiros NE, et al. Retinal pigment epithelial expression of complement regulator CD46 is altered early in the course of geographic atrophy. *Exp Eye Res.* 2011 Oct;93(4):413–423. Available from: <http://dx.doi.org/10.1016/j.exer.2011.06.002>. 87
- [139] Boulton M, McKechnie NM, Breda J, Bayly M, Marshall J. The formation of autofluorescent granules in cultured human RPE. *Invest Ophthalmol Vis Sci.* 1989 Jan;30(1):82–89. 88
- [140] Biesemeier A, Schraermeyer U, Eibl O. Chemical composition of melanosomes, lipofuscin and melanolipofuscin granules of human RPE tissues. *Exp Eye Res.* 2011 Jul;93(1):29–39. Available from: <http://dx.doi.org/10.1016/j.exer.2011.04.004>. 88
- [141] Burns RP, Feeney-Burns L. Clinico-morphologic correlations of drusen of Bruch's membrane. *Trans Am Ophthalmol Soc.* 1980;78:206–225. 88
- [142] Johnson LV, Forest DL, Banna CD, Radeke CM, Maloney MA, Hu J, et al. Cell culture model that mimics drusen formation and triggers complement activation associated with age-related macular degeneration. *Proc Natl Acad Sci U S A.* 2011 Nov;108(45):18277–18282. Available from: <http://dx.doi.org/10.1073/pnas.1109703108>. 88
- [143] Johnson PT, Lewis GP, Talaga KC, Brown MN, Kappel PJ, Fisher SK, et al. Drusen-associated degeneration in the retina. *Invest Ophthalmol Vis Sci.* 2003 Oct;44(10):4481–4488. 88
- [144] Johnson LV, Leitner WP, Staples MK, Anderson DH. Complement activation and inflammatory processes in Drusen formation and age related macular degeneration.

- Exp Eye Res. 2001 Dec;73(6):887–896. Available from: <http://dx.doi.org/10.1006/exer.2001.1094>. 89
- [145] Chen PM, Gombart ZJ, Chen JW. Chloroquine treatment of ARPE-19 cells leads to lysosome dilation and intracellular lipid accumulation: possible implications of lysosomal dysfunction in macular degeneration. *Cell Biosci.* 2011;1(1):10. Available from: <http://dx.doi.org/10.1186/2045-3701-1-10>. 89
- [146] Melan MA. 8. In: *Methods in Molecular Biology: Immunocytochemical Methods and Protocols Overview of Cell Fixation and Permeabilization*. Lorette C. Javois; 1995. . 91
- [147] Kaufmann R, Mueller P, Hausmann M, Cremer C. Imaging label-free intracellular structures by localisation microscopy. *Micron.* 2010 May; Available from: <http://dx.doi.org/10.1016/j.micron.2010.03.006>. 91
- [148] Kaufmann R. *Entwicklung quantitativer Analysemethoden in der Lokalisationsmikroskopie*. University of Heidelberg; 2011. 94
- [149] King AN, Manning CF, Trimmer JS. A unique ion channel clustering domain on the axon initial segment of mammalian neurons. *J Comp Neurol.* 2014 Jan; Available from: <http://dx.doi.org/10.1002/cne.23551>. 94

ACKNOWLEDGEMENTS

I thank everyone, who has supported or contributed to the success of this work!

Nothing is impossible! (All Blacks)

ERKLÄRUNG

Ich versichere, dass ich diese Arbeit selbstständig verfasst und keine anderen als die angegebenen Quellen und Hilfsmittel benutzt habe.

Heidelberg, den

.....
(Sabrina Roßberger)